ABSTRACT

Title of Dissertation:	UNDERSTANDING AND CONTROLLING NANOSCALE CHIRALITY: MATERIALS SYNTHESIS, CHARACTERIZATIONS, MODELING AND APPLICATIONS
	Hanyu Liu, Doctor of Philosophy, 2024
Dissertation directed by:	Professor, Min Ouyang, and Department of physics

Chirality, the property of objects possessing non-superimposable mirror images, initially identified and explored in organic and biological molecules, has gained growing interests in the realm of inorganic nanomaterials due to its foreseeable applications in the fields such as Enantiochemistry, Nanophotonics, Spintronics.

In the first segment of this dissertation, we demonstrate a bottom-up synthetic strategy to induce chirality in plasmonic nanoparticles and hybrid plasmonic-semiconductor nanostructures. Subsequently, we detail a simplified analytical coupled-oscillators model to facilitate the understanding of plasmonic-chiral coupling and predict various chiroptical responses based on different coupling strengths, validated through finite element method simulations. Furthermore, advancements in characterizing nanoscale chirality with high spatial resolution at the single nanoparticle level are explored using a novel polarization-dependent optical atomic force microscopy technique, overcoming resolution limits in far field measurements. Finally, we

demonstrate the employment of nanoscale chirality to induce spin polarization and enable unique nanoscale chiral Floquet engineering.

UNDERSTANDING AND CONTROLLING NANOSCALE CHIRALITY: MATERIALS SYNTHESIS, CHARACTERIZATIONS, MODELING AND APPLICATIONS

by

Hanyu Liu

Dissertation submitted to the Faculty of the Graduate School of the
University of Maryland, College Park, in partial fulfillment
of the requirements for the degree of
Doctor of Philosophy
2024

Advisory Committee:
Professor Min Ouyang, Chair
Professor Thomas Murphy
Professor Taylor Woehl
Professor Gregory Jenkins
Professor Lourdes Salamanca-Riba, Dean's Representative

Acknowledgements

My journey of graduate study at the University of Maryland are filled with support of many people. I would like to take this opportunity to express my heartful gratitude.

First of all, I would like to thank my advisor Prof. Min Ouyang. He has provided great support and guidance throughout my whole graduate study. He has not only been an excellent mentor in research problems but also inspired me to be a critical thinker and strive for excellence. It's his patience and dedication that made my journey a rewarding experience. I would like to also thank previous lab members in our research group: Dr. Geng Li, Dr. Shangjie Yu, Dr. Pengpeng Wang and Dr. Yanjie He. I gained firsthand experience by their side and built upon their pioneering work, which laid the foundation for my research. Furthermore, it's always pleasant to work along with my current labmates: Huayu Zhang, Xinying Ding, Yonatan Gazit, Aiden Riley, Michael Parker, Fahad Shaikh. We are from different culture and research backgrounds and come together as a great interdisciplinary team. I truly enjoyed the stimulating and insightful discussions we had.

I would like to thank Dr. Gregory Jenkins from the Laboratory for Physical Sciences for his input and helpful discussion in the project of polarization dependent optical AFM. I am thankful to Dr. Jiancun Rao and Dr. Sz-Chian Liou of the NanoCenter, for their assistance in TEM and SEM characterization.

Finally, I would like to extend my sincere gratitude to my parents. They have been supportive and considerate throughout my research journey away from home for the

past years. It’s their constant care and encouragement that made me believe I can overcome any challenges.

Table of Contents

List of Figures

List of Abbreviations

3D	Three Dimensional
CD	Circular Dichroism
ORD	Optical Rotatory Dispersion
LCP	Left-handed Circularly Polarized Light
RCP	Right-handed Circularly Polarized Light
LSPR	Localized Surface Plasmon Resonance
AFM	Atomic Force Microscopy
SNOM	Scanning Near Field Optical Microscopy
PiFM	Photo-induced Force Microscopy
TEM	Transmission Electron Microscopy
SEM	Scanning Electron Microscopy
FEM	Finite Element Method
CISS	Chirality-Induced Spin Selectivity
TRFR	Time Resolved Faraday Rotation

Chapter 1: Introduction

1.1 Background

Chirality describes a general property of objects that possess non-superimposable mirror images, for example, human hands. Generally, a chiral object and its mirror images are referred to as 'left-handed' and 'right-handed' respectively. (Figure 1.1). Chirality was initially extensively studied in life science.[1] It's found that most biological molecules and tissues are chiral and enantioselective reactions have been found significant in investigation for the exploration of life origin as well as application for pharmaceuticals.[2] For example, most DNA molecules have a right-handed double helix structure, and all 21 essential amino acids only exist in L-enantiomers in life.

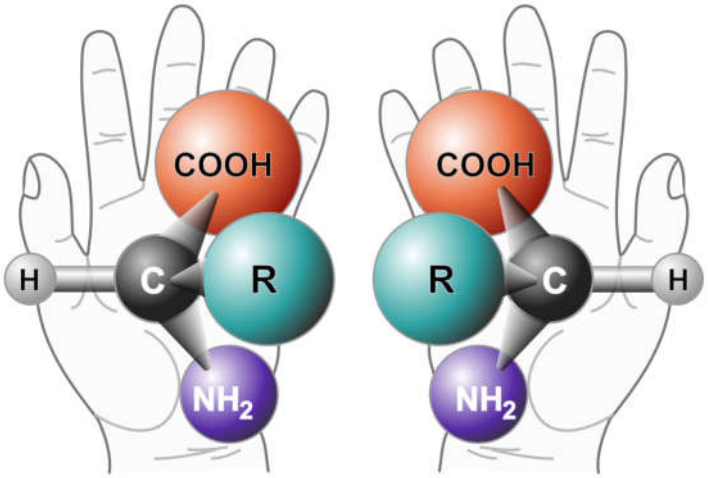

Figure 1.1. Two enantiomers of a generic chiral amino acid. Image from Wikipedia page of 'Chirality'.

The interesting physical and chemical properties manifested by chiral objects originate from the broken symmetry of their structures.[3] The broken symmetry affects the light-matter interaction of chiral objects leading to so-called optical activities. Circular dichroism (CD) and optical rotatory dispersion (ORD) are the two most common optical activities, where CD describes the difference in absorption of left and right circularly polarized light and ORD describes the difference in the propagation velocity of polarized light. Objects of opposite chirality present CD and ORD of opposite signs and same amplitude. Distinguishing biomolecules of different handedness has been vital in many cases. For example, in pharmaceutical industry, while the drug molecules of one chirality show beneficial medical effects, the drug molecules of the opposite chirality could be toxic[4]. Measurement of chiroptic response, especially CD, are thus developed as a great tool for handedness discrimination and characterization of chiral biomolecules.

Although the majority of research efforts on chirality have been focused on organic molecules due to historical reasons and availability, recent years has witnessed a rising interest in exploration of chirality in inorganic systems due to promising broad application and exotic physics. One example is introduction and control of chirality in plasmonic materials which is a natural platform of strong light-matter interaction thanks to localized surface plasmon resonance (LSPR). LSPR is a collective photon driven electronic oscillations in plasmonic metals which manifests a large optical response and strong confined electromagnetic fields and thus naturally leads to potential strong chiroptical response.[5-6] Meanwhile, semiconductor materials have been a hot research topic due to various physics and applications from exciton

dynamic to LED. Integrating chirality with semiconductor materials opens up a research field of potential applications in circularly polarized photoluminescence, chiral sensing and the optical manipulation of electron spins.[7-9] The research efforts of realization of chiral objects have been following two general directions: top-down and bottom-up methods. Top-down nanofabrication methods like direct laser writing[10] and lithography based technique[11-13] have fabricated plasmonic nanostructures with chiral morphology with various shapes. Meanwhile, bottom-up chemical methods are garnering significant interests due to their potential of scalability and efficiency and compatibilities of further fabrication of assembly and hybrid nanostructure.[7,8,14-23] Although most inorganic lattices are achiral, the chirality could be induced by breaking symmetry of lattice facets in bottom-up chemical synthesis. Recent discoveries have shown that the enantioselective adsorption of chiral molecules on surface chiral facets of an achiral lattice breaks the surface symmetry and potentially enable the enantioselective growth of nanoparticles.[14-16] Conversely, chirality could also be induced and controlled by introducing the coupling of achiral and chiral objects or chiral coupling of achiral objects in bottom-up methods. For instance, molecular self-assembly of achiral plasmonic nanoparticles has been shown to effectively create chiral plasmonic nanostructures with strong chiroptical response.[17-19] Additionally, the coupling of plasmons with chiral biomolecules or media has demonstrated enhancement and manipulation of the original chiroptical response and even lead to the emergence of novel chiral hybrid light-matter states.[20-23] Along with experimental efforts of introducing chirality in inorganic systems, there are both theoretical and numerical efforts of understanding the chirality mechanism. The

chiroptical response of chiral medium could be characterized by a second order term called non-locality tenser in its constitutive relations. Historically, dipole and oscillator models were demonstrated to be successful in modeling the physical origin of chiroptical properties of organic molecules and have been recently applied to inorganic chiral medium and their plasmon analog.[] The dipole and oscillator model provided a simple but effective tool for a theoretical understanding and also served as the guidance for design of chiral nanostructures. On the other hand, given a certain chiral nanostructure, it was demonstrated that numerical simulation (e.g. finite element method) could give a reasonably accurate prediction of its chiroptical response.

With the rapid advancement of inorganic chirality material systems, there is an growing need for characterization tools that enable microscopic observation of chiroptical response of individual nanoparticles and even allow for spatially dependent chiroptical feature analysis. For instance, a local chiroptical characterization would be necessary to understand the underlying mechanism of chiroptical properties of individual chiral inorganic nanoparticles as well as nanoscale coupling among the chiral and achiral objects. However, traditionally the chiroptical measurements have been limited to ensemble measurements[24-25] and the effort to improve spatial resolution of far field measurements is restricted by the diffraction limit.[18,26] Optical AFM techniques including AFM-IR and SNOM are experimental tools that integrates optical and AFM measurement. These newly developed techniques allow acquisition of near field optical signal simultaneously with morphological information and therefore build the connection of optical responses

and the local features. Introduction of polarization dependent measurement into the optical AFM measurement could provide the opportunity to characterize the nanoscale chiroptical features in the chiral nanostructures.

Apart from the chiroptical response, the symmetry breaking of chiral objects also breeds other fascinating physical phenomena, such as chiral phonon[27-30], chiral optical force[31-33] and spin control[35-42]. Chiral phonon describes mirror-asymmetric vibrational states which can be characterized by terahertz circular dichroism spectroscopy. The diagnostic ability of such chiral phonons is found to be important in pharmaceuticals and biomedical images. On the other hand, it's demonstrated that chiral plasmonic nanoparticles can be exerted a circular polarization-dependent gradient optical force by circularly polarized laser, which provides an optical approach for manipulating and separating chiral objects.[31] Moreover, there have been predictions and demonstrations of the potential applications of chiral objects in spintronics. For example, it's found that chiral molecules could exhibit chirality induced spin selectivity (CISS)[38-42], where the spin of the transmitted electrons is influenced by the handedness of chiral biomolecules. Previous research of chirality induced spin effect has been focused on biomolecules due to historical reasons and difficulties in synthesis of chiral inorganic nanostructure. The newly developed synthetic strategy for creating chiral inorganic structures provides an excellent testbed for investigation of chirality-spin interplays in inorganic systems.

1.2 Overall structures

The rest of the dissertation is organized as follows.

Chapter 2 demonstrates a bottom-up synthetic strategy to induce chirality in inorganic nanoparticles using chiral Au nanocube and chiral Au nanorod as an example.(published[16]) Surface geometric chirality is introduced by uneven distribution of chiral high Miller index facets facilitated by the enantioselective adsorption of chiral molecules. We further demonstrate the synthesis of chiral hybrid plasmonic-semiconductor nanoparticles based on the chiral plasmonic nanoparticles, which proves the robustness of the geometric chirality.

Chapter 3 details a simplified analytical coupled-oscillators model to facilitate the understanding of plasmonic-chiral coupling. We build the coupled-oscillator model by integrating plasmonic oscillator with Born-Kuhn model. Based on the oscillator model, we predict various chiroptical responses at different coupling strengths and discussed the underlying mechanism of CD. The predictions are further validated through finite element method (FEM) simulations.

Chapter 4 presents our advancements in characterizing nanoscale chirality with high spatial resolution at the single nanoparticle level. By using a novel polarization-dependent optical atomic force microscopy technique, we are able to overcome resolution limits in far field measurements and characterize a synthesized chiral plasmonic helicoid nanoparticle. The results are further analyzed based on the underlying physical mechanism and evaluated with simulated near field electric field distribution of the chiral helicoid.

Chapter 5 presents a low-temperature ultrafast optical measurement on the synthesized chiral hybrid Au-CdS core-shell nanoparticles following the synthetic

strategy presented in Chapter 2. We acquired the time-resolved Faraday rotation (TRFR) of the chiral Au-CdS core-shell nanoparticles and demonstrated the employment of structural chirality to induce spin polarization and spin manipulation.

Chapter 6 summarizes the dissertation and outlines some future research.

Chapter 2: Tuning Geometric Chirality in Metallic and Hybrid Nanostructures by Controlled Nanoscale Crystal Symmetry Breaking

2.1 Introduction

2.1.1 Background

Chirality (or handedness) represents a pervasive and fundamental geometric character of an object whose space group contains no improper symmetry operations. While organic chiral molecules containing cyclic or dihedral point groups and their induced chirality-dependent phenomena have been extensively studied[43], exploration of inorganic chiral objects has been limited until recently due to their structural complexity with involvement of many atoms as well as lack of understanding of underlying chiral mechanisms. Nevertheless, if chirality of inorganic objects can be induced or even controlled, it should open up many foreseeable opportunities for emerging exotic physics and applications. For example, merging chirality with metal nanostructures could potentially induce chiral plasmons with tunable and enhanced chirality and the emerging chiral vortical effects (e.g., negative refractive materials)[5,44-45]. A few mechanisms have been proposed to induce inorganic chirality. For example, there exists a small group of inorganic crystals such as quartz, mercury sulfide and tellurium that can possess a chiral atomic lattice along certain crystallographic axes, leading to intrinsic handedness[46,47]. Although intrinsic lattice handedness is absent in achiral in-organic metals and semiconductors, extrinsic handedness can be induced by either electromagnetic coupling or inter-particle

assembly via chiral templates[18,20,48,49]. Nevertheless, such extrinsic handedness is in general not robust and has limited applications. From the crystallographic viewpoint, the kinked site of step edges can act like a chiral center in an organic molecule to break mirror symmetry in an inorganic achiral lattice, rendering two high Miller index crystallographic planes enantiomorphous (see more details in Supporting Information). Figure 2.1 shows the unit sphere of a face centered cubic (fcc) lattice that can be divided to different regions designated by two distinct colors, representing two sets of left- and right- handed chiral planes, respectively. Although the racemic mixture of chiral high Miller index planes should not induce handedness in a bulk crystal, when they are exposed and controlled on the surface of a crystal the enantiomeric excess favoring chiral facets with definite handedness can be induced by chiral symmetry breaking, leading to the formation of chiral boundary morphology and thus extrinsic chirality of an achiral crystal. Importantly, a few theoretical studies have shown enantiospecific interactions between chiral molecular adsorbates and inorganic chiral facets, which has also been experimentally confirmed by scanning tunneling microscopy[50-53]. This can potentially offer a general and effective pathway to enable symmetry breaking of crystallographic chiral facets towards new chiral materials design and enantioselective control of inorganic chiral nanostructures.

2.1.2 Chiral high Miller index facets

The chiral boundary morphology in our current work originates from the broken symmetry of chiral high Miller index facets on the surface of an inorganic crystalline lattice. We use Au as an example to denote its associated handedness. The crystal

structure of Au is face-centered cubic (fcc) with no intrinsic lattice chirality. A high Miller index plane with index of (hkl), where h≠k≠l and hkl≠0, cannot be superimposed by its mirror image by any combination of rotations and translations. This crystalline plane is defined as a chiral plane, with one example of (321) plane shown in the Figure 2.1. In general, from the viewpoint of atomic structure, such high Miller index chiral plane can be signified by a micro unit cell (with in-plane translation) consisting of atomic kink site that acts as the interconnect of an ordered combination of symmetric Miller planes like (100), (110) and (111), mimicking a chiral center from an organic chiral molecule. To that, we follow Attard's notation to assign an R- or S- designation to a high Miller index chiral plane[54]: when viewing from above a chiral plane (Figure 2.1), if its interconnected symmetric low Miller index microfacets around the atomic kink site are oriented clockwise from the most densely packed microfacet to the least densely packed one, it is defined as R- chiral plane, and vice versa for the S- chiral plane. For example, the R-(321) plane in Figure 2.1 has a clockwise conformation of (111) → (100) → (110), while the S-(321) manifest a counter-clockwise conformation of (111) → (100) → (110). Because of the crystal symmetry as shown in Figure 2.1a, although there exist many high Miller index chiral planes in a bulk achiral crystal, their effects are cancelled out. Nevertheless, the symmetry between two chiral planes with opposite handedness can be broken on the surface.

It has been demonstrated both experimentally and theoretically that there exist enantioselective interactions between chiral organic molecules and inorganic chiral planes defined above[50,52,53]. In general, the L-cysteine molecules consistently show

enantioselective binding on high Miller index chiral R-facets, while D-cysteine molecules favor occupation onto the chiral S-facets. For example, the DFT calculations have shown that the adsorption energy of L-cysteine on R-(321) is higher than that on S-(321), leading to enantioselective binding of L-cysteine on R-(321).[50,52,53]

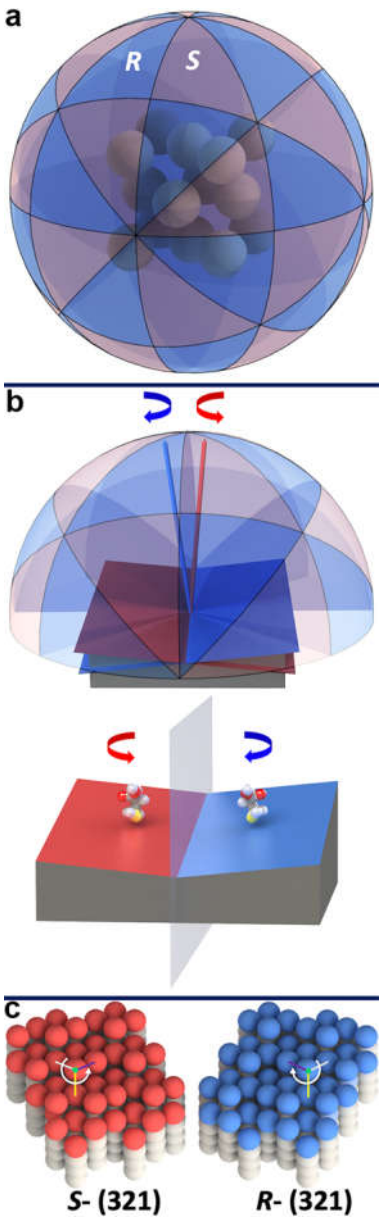

Figure 2.1. Designation of high Miller index chiral facets in a crystalline lattice. (a) Unit spherical representation of atomic *fcc* lattice (small spheres at the center). Any single point on the surface can define a zone axis of crystalline plane. Black curves highlight all the crystalline planes that possess at least one mirror symmetry. The regions lying off the mirror zones are designated by two different colors, light blue and light red, to represent sets of *R*- and *S*- chiral planes, respectively. (b) Construction of enantiomeric crystalline plane (top) by following notation in (A), with enantiospecific interaction with small chiral organic molecules (bottom). Red (*S*-) and blue (*R*-) represent chiral planes, having enantioselective binding with *D*- and *L*-chiral molecules, respectively. (c) Atomic models of exemplary chiral *R*-(321) and *S*-(321) facets showing that the kinked site (green filled circles) of step edges in a high Miller index plane behaves as a "chiral center", leading to the chirality.

2.2 Results and discussions

2.2.1 Synthetic strategy

Figure 2.2 shows schematics of how to employ small organic chiral molecules to preferentially occupy enantioselective chiral facets during the synthesis of achiral inorganic nanostructures. This enantioselective interaction leads to a biased kinetic growth rate favoring crystallographic overgrowth with opposite handedness, thus dictating the prevailing coverage of one handedness of chiral facets on the surface to induce robust chiral boundary morphology of an inorganic nanostructure. One significance of such chiral inorganic nanostructures is to serve as building blocks to allow creation of novel chiral hybrid nanostructures through interfacial epitaxial and non-epitaxial growth to form various chirality coupling at the nanoscale[55]. We choose Au nanostructures as an example to demonstrate the proposed strategy in Figure 2.2 based on a few considerations: First, the Au possesses an achiral fcc lattice and

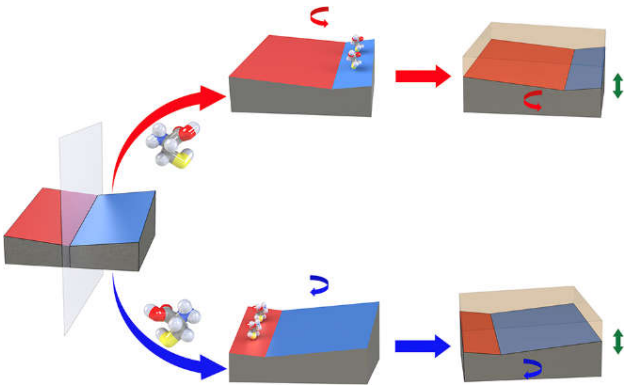

Figure 2.2**.** Schematic of controlled bottom-up growth of chiral inorganic materials and their enabled chiral hybrid nanostructures. Red and blue represent high Miller index chiral *S*- and *R*- crystallographic planes, respectively. Small chiral organic molecules are employed to break structural symmetry and to enable enantiomerically pure chiral boundary morphology to induce crystallographic handedness in inorganic materials. The robustness of chiral boundary morphology of inorganic materials can allow integration of multiple components (yellow block) by the formation of hybrid nanostructures, possessing interfacial chirality coupling (green arrows).

synthesis of achiral Au nanostructures with versa-tile controls have been achieved, which make Au an excellent testbed for understanding role of chiral morphology in an achiral crystal[56-58]. It is worth noting that a gigantic chiral Au structures with a size of a few hundred nanometers have been achieved recently[14,15,59], however small sized chiral Au nanocrystals with robust chirality that can be potentially utilized as chiral functional building blocks have been absent, which is the impetus of our current work; Second, Au nanostructures have been demonstrated to possess strong localized surface plasmon resonance (LSPR), which is uniquely determined by the size and morphology of nanostructures[60]. Therefore, chirality of crystalline boundary morphology should have a direct implication in the LSPR due to delocalization of plasmonic electrons, which plays an important role in the emerging field of chiral plasmonics and in understanding the interplay be-tween chirality and plasmonics; Last but not the least, it has been demonstrated that functional hybrid nanostructures consisting of metal and semiconductor subunits can be synthesized by non-epitaxial approach with enhanced and tunable light-matter coupling[55, 61, 62]. Consequently, if the standalone chiral Au nanostructures can be achieved with robust chirality, chirality of metal subunits might be imprinted to semiconductor subunits to create unique chiral hybrid nanostructures with exotic functionality and properties.

In following the proposed synthetic strategy outlined in Figure 2.2, we start with Au nanostructures with well-defined achiral morphology (e.g., nanocubes, NCs or nanorods, NRs) as seeds, followed by surface treatment with chiral molecules (e.g., L-/D- cysteine). After the removal of excessive chiral molecules from the surface

treatment, overgrowth of chiral Au nanostructures is initiated and kinetically controlled by a slow injection of an Au precursor with a mild reducing agent such as ascorbic acid.

2.2.2 Chiral Au nanocube (NCs)

The achiral Au seed NCs are synthesized by a revised seed-mediated method[63]. Typically, a 0.5 ml of Au seed NCs solution is added into 1.5 ml of 80 mM CTAC solution. A 10~25 μl of 70 μM L-cysteine (or D-) solution is added and the mixed solution is kept stirring for 30 mins to adsorb the cysteine molecules on the surface of Au NCs. The mixed solution is centrifugated by 13200 rpm for 10 mins and the supernatant is discarded to remove the extra cysteine molecules in solution. This centrifugation process is repeated twice, redispersing each time in DI water. The precipitate is then re-dispersed into 0.5 ml of DI water, followed by addition of 1.5 ml of 80 mM CTAC solution and 100 μl of 0.1M ascorbic acid under stirring. A 500 μl of 1 mM $HAuCl_4$ solution is slowly injected into the mixture solution by syringe pump for 30 minutes. The products (i.e., chiral Au NCs) are washed out by centrifugation and redispersed into the DI water.

Figure 2.3a shows a typical transmission electron microscopy (TEM) image of chiral S-Au NCs with average size of 50 nm by using L-cysteine molecules, which were grown from achiral seed NCs shown in Figure 2.4. Different from achiral Au NCs possessing uniform morphology with flat surface, high-resolution TEM image of a single chiral NC as presented in Figure 2.3b show inhomogeneous identities on the surface with a few highlighted by red arrows. Importantly, the circular dichroism

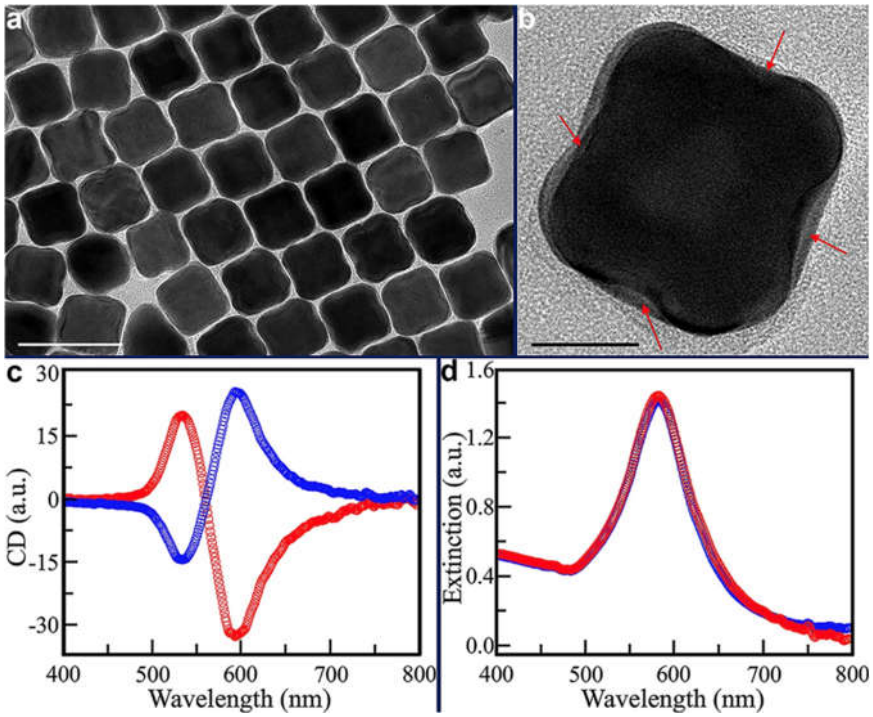

Figure 2.3. Synthesis and characterizations of chiral Au NCs. (a) Typical large-scale TEM image of chiral *S*-Au NCs. Scale bar, 100 nm. (b) Typical TEM image of individual *S*-Au NC. A few inhomogeneous features on the surface are highlighted by red arrow. Scale bar, 20 nm. (c) Experimental CD spectra of *S*- (red) and *R*- (blue) Au NCs. (d) Experimental extinction spectra of *S*- (red) and *R*- (blue) Au NCs.

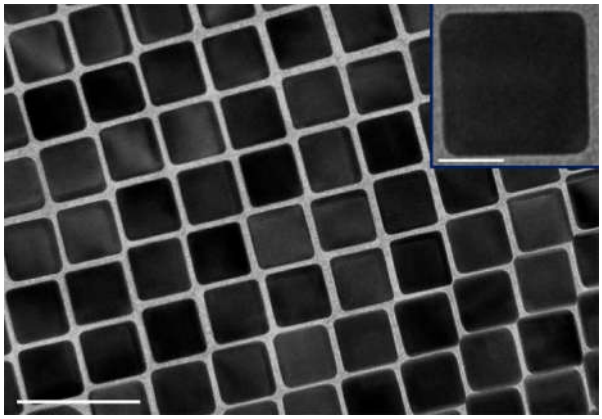

Figure 2.4. Achiral Au NCs as seeds for growing chiral Au NCs. Typical TEM image. Scale bar, 100 nm. Inset shows a single achiral NC with scale bar of 20 nm. Straight edges and flat surface of achiral Au seed NCs can be clearly revealed.

(CD) measurement of as-synthesized S-Au chiral NCs in Figure 2.3a shows the presence of a clear bisignate spectra feature (red data points in Figure 2.3c), i.e., a positive peak at 532 nm and a negative peak at 592 nm. For the chiral R-Au NCs that are synthesized by using D-cysteine molecules while other synthetic conditions remain the same, their corresponding CD spectrum is also presented in Figure 2.3c (blue data points) for comparison, in which the CD peaks occur at the same wavelengths but with opposite sign. For both R- and S- chiral Au NCs, their optical extinction spectra are almost identical (Figure 2.3d), similar to the case of molecular enantiomers.

A few mechanisms have been proposed to account for chiral plasmonic nanoparticles, including electromagnetic interaction between chiral molecules and plasmonic resonance on the surface and formation of chiral oligomers[17,18,48]. We have performed one control experiment by passivating the surface of achiral Au NCs with chiral molecules but without overgrowth, however no detectable CD is found from such samples. This is also consistent with theoretical study that for the high symmetric plasmonic nanostructure like nanosphere or NCs, the chirality induced by electromagnetic coupling between embedded/coated chiral molecules and nanostructures could be cancelled out, and the effect of chiral molecules in this scenario is negligible[20]. Furthermore, although chiral-template- mediated inter-particle interactions in a plasmonic oligomer has been observed in literatures[64], such chiral oligomers have been absent in our current study based on TEM and SEM characterizations, and the concentration of chiral molecules utilized in our chiral synthesis is much smaller than those required for the formation of chiral oligomers.

In order to understand the inhomogeneous morphological features as highlighted in Figure 2.3a and 2.3b and to elucidate the origin of their optical characteristics shown in Figure 2.3c and 2.3d, we have performed a thorough angle-dependent high-resolution SEM characterization of single S-Au NC with three examples presented in Figure 2.5a. A few structural features can be immediately identified: First, although the overall shape of chiral Au NC remains cubic, its surface becomes concave after the overgrowth, which is consistent with TEM observation in Figure 2.3b and can be attributed to the edge- and corner- favored growth under the kinetically controlled

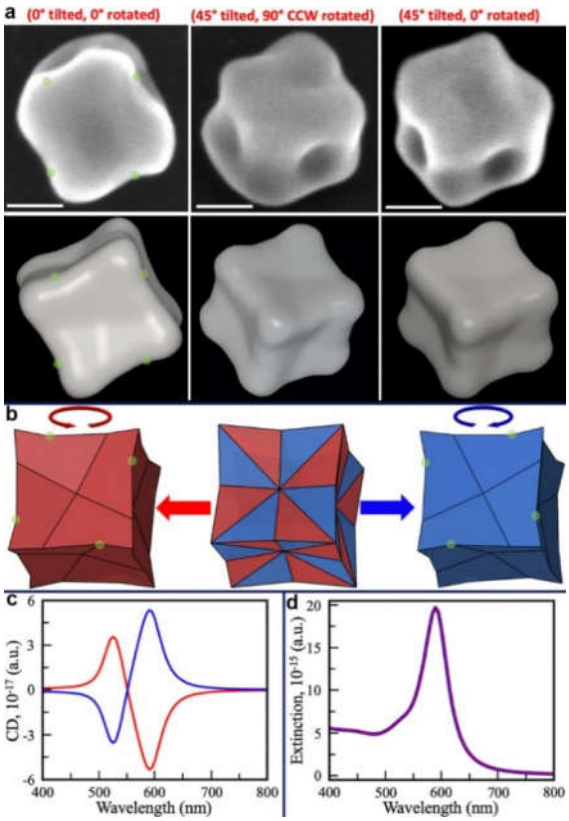

Figure 2.5. Angle-dependent high-resolution SEM characterizations and modeling of chiral Au NCs. (a) (Top) SEM images of single *S*-Au NC under three different viewing angles. Scale bar, 20 nm. (Bottom) Corresponding structural model. (b) Schematic showing the formation of *S*- (left) and *R*- (right) chiral NCs facilitated by the prevailing chiral high Miller index facets on the surface due to chiral symmetry breaking from an achiral NC (middle). Small green filled circles as guide to the eye highlight the twisted edges on the boundary. (c) & (d) Computed CD and extinction spectra of *S*- (red) and *R*- (blue) chiral Au NCs by using the structural model presented in (A), respectively.

condition[65]. The fact of formation of concave surface further suggests the exposure of high Miller index facets during the growth[58,67]. Second, the boundary edges of chiral Au NC are twisted as is evident from the twisting sites highlighted by the four small green circles in Figure 2.5a. From the crystallographic viewpoint (Figure 2.1and Figure 2.2), the surface of a regular achiral concave Au NC can be modeled as a racemate of chiral high Miller index facets, which is schematically shown in the

middle of Figure 2.5b. In the presence of chiral molecules like L-cysteine, the preferential occupancy of chiral molecules onto specific chiral facets (e.g., R-facets for L-cysteine) inhibits their successive outward growth and thus leads to preferential kinetic growth of chiral facets with opposite handedness. As a result, the predominant coverage of chiral facets with exclusive handedness is achieved on the surface of a chiral NC, resulting in chiral morphology with feature of twisting boundary edges, as schematically shown in Figure 2.5b. The small green filled circles on both the right and left NCs in Figure 2.5b highlight the twisting sites on the edge, which are formed by simply considering the prevailing overgrowth of one type of chiral facets from a concave surface. Based on the proposed mechanism illustrated in Figure 2.5b, we have constructed a structural model and compared it with SEM images acquired at the different tilting and rotating angles (Figure 2.5a), which shows excellent agreement with experimental results and can elucidate chiral characteristics of morphology as manifested in the SEM characterization. More importantly, we have utilized the constructed models presented in Figure 2.5a to compute optical properties of chiral Au NCs by using finite element method (FEM) simulation[67], and presented both theoretical CD and extinction spectra in Figure 2.5d, which also shows excellent agreement with experimental data in Figure 2.4c and 2.4d. This offers a sanity check of our model and supports the proposed CD mechanism of as-synthesized chiral Au NCs.

2.2.3 Chiral Au nanorods (NRs)

We would like to emphasize that our model and understanding of the CD origin in a chiral Au NCs, which is based on the symmetry breaking of chiral high Miller index facets on the surface, is general and can be immediately applied to other nanostructures to induce and control similar extrinsic handedness. Figure 2.6 presents another example of chiral Au NRs by following a similar mechanism and growth process. As compared with Au NCs, Au NRs are more complicated from the structural viewpoint, but possess more tunability to engineer their properties and functionalities. For example, a few structural parameters including the aspect ratio (AR) and the surface facets on both sides and ends of a NR often play a crucial role in determining various physical and chemical properties and functionalities.

We chose achiral Au NRs that are synthesized by using the well-known seed-mediated growth method as the starting structures[68]. The growth of chiral Au NRs starts with preparation of seed solution, in which a 5 ml of 0.2 M CTAB solution is mixed with 5 ml of 0.5 mM $HAuCl_4$, followed by addition of 0.6 ml of ice-cold 0.010 M $NaBH_4$ under vigorous stirring for 2 mins and then aged for 30 mins before further usage. A 5 ml of 0.2 M CTAB is mixed with 0.1 ml of 4 mM $AgNO_3$ solution and 5 ml of 1 mM $HAuCl_4$ solution, and after gentle mixing by hand shaking of the solution, 70 µl of 0.1M ascorbic acid is added. This step is followed by addition of 12 µl of the above seed solution. After aging for 12 hrs, the solution is centrifuged at 13200 rpm for 10 mins, and the precipitate (i.e., achiral Au NRs) is re-dispersed in 2 ml of DI water as seed NRs for the subsequent overgrowth of chiral Au NRs. For the

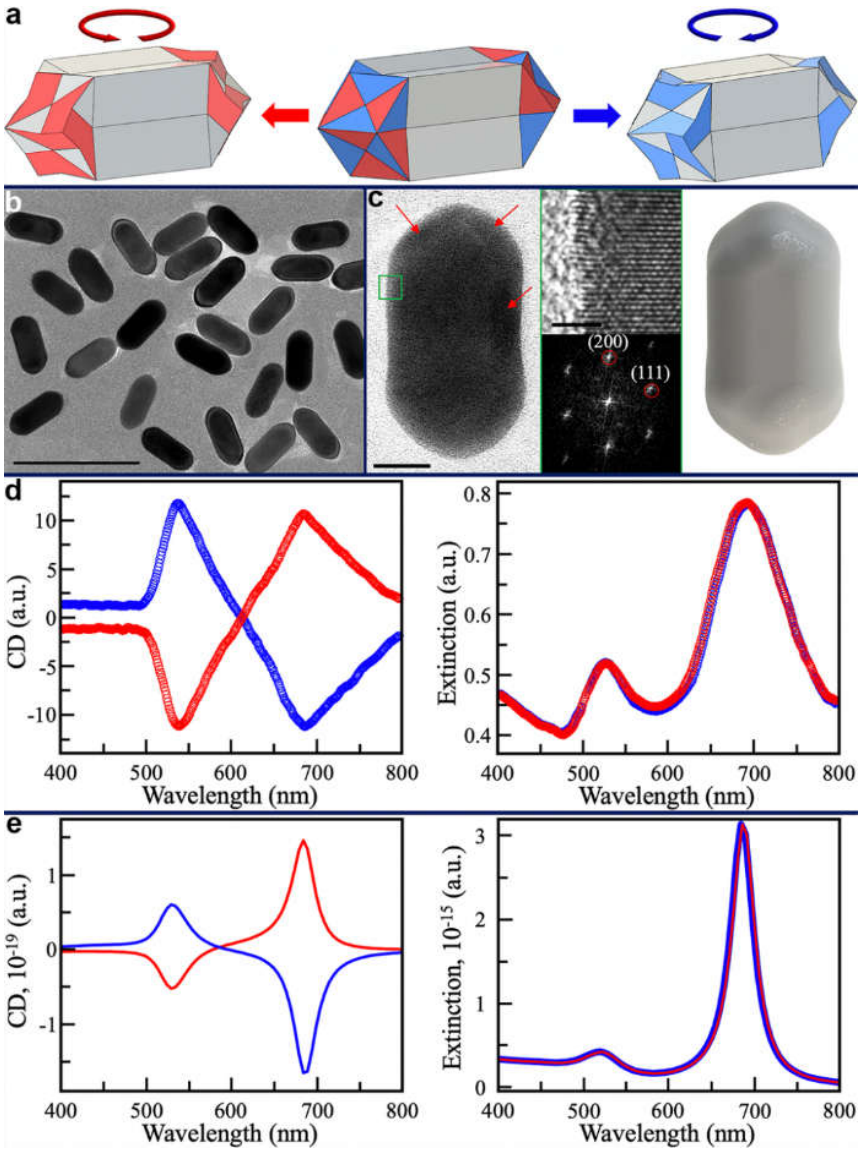

Figure 2.6. Synthesis, characterizations and modeling of chiral Au NRs. (a) Schematic showing that by breaking the symmetry of enantiomeric high Miller index facets (red and blue colors represent chiral crystallographic S- and R- facets, respectively) at the ends of achiral NR (middle), chiral S- (left) and R- (right) NRs can be formed by the prevailing chiral facets at the ends, while its elongated side consists of symmetric low Miller index facets (gray color) as those of achiral NR. (b) Typical large-scale TEM image of chiral S-Au NRs. Scale bar, 100 nm. (c) (Left) High-resolution TEM image of single chiral S-Au NR. (Middle top) Atomic resolved TEM image of the green re-gion on the left image. Scale bar, 2 nm. (Middle bottom) the FFT pattern of the side of NRs. The side facets of the chiral NR are identified by both imaging and indexing the FFT pattern. (Right) Constructed structural model of chiral S-NR. (d) Experimental CD (left) and extinction (right) spectra of chiral S- (red) and R- (blue) Au NRs. (e) Computed CD (left) and extinction (right) spectra of chiral S- (red) and R- (blue) Au NRs by using the structural model in (C).

growth of chiral Au NRs, a 1 ml of above Au seed NRs solution is mixed with 1 ml of 80 mM CTAC and 10 µl of 0.3 mM L- (or D-) cysteine molecule. The mixture solution is aged for 1 h. After aging, a 10 µl of 5 mM $HAuCl_4$ and 0.2 ml of 0.1M ascorbic acid is added and aged for 1 h. Then the solution is centrifuged at 13200 rpm for 10 mins to get the Au NRs and repeated twice and dispersed in 2 ml of 80 mM CTAC. A 30 µl of 5 mM $HAuCl_4$ solution and 0.2 ml of 0.1 M ascorbic acid is added to the above solution, followed by aging for 1 h. After aging, the solution is centrifuged twice at 13200 rpm for 10 mins, and the chiral product is re-dispersed in 2 ml of 80 mM CTAC solution. Similar overgrowth condition is repeated to grow chiral Au NRs with different aspect ratio and protrusions and eventually the final product is collected by centrifugation and redispersion into DI water. Typically, a regular achiral NR can be modeled as a four-sided elongated rhombic dodecahedron (middle in Figure 2.6a)[69-72], whose side surfaces manifest achiral low index facets (110), while the high surface curvature at the apexes often makes chiral high Miller index facets (red and blue regions) more accessible at both ends. This can provide an invaluable opportunity to induce intriguing chirality of NRs by controlling the prevalence of chiral high Miller index facets at the end of NRs, as schematically shown in Figure 2.6a. Figure 2.6b shows one typical TEM image of overgrown chiral Au NRs assisted by the chiral L- cysteine molecules in the growth. Both high-resolution TEM (Figure 2.6c) and SEM characterizations (Figure 2.7) have confirmed that our as-synthesized chiral Au NR remains an overall four-sided elongated rhombic dodecahedron but with concave morphology in the boundary facets. The atomic image and its Fast Fourier Transform (FFT) pattern show the undistorted (110) facets on the sides, while

the concave morphology can be clearly observed at both ends of NRs, that is similar to the concave characteristics and chiral high Miller index facets of chiral NCs in Figure 2.3.

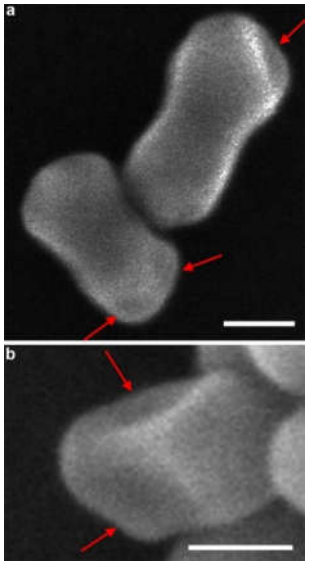

Figure 2.7. SEM images of chiral Au NRs. (a) Image showing concave facets at the ends of NRs (highlighted by red arrows). Scale bar, 20 nm. (b) Image showing straight and undistorted concave facets on the side (highlighted by red arrows). Scale bar, 20 nm.

We have found that the as-synthesized chiral Au NRs manifest CD features in the visible regime. In particular, Figure 2.6d (red data points) shows experimental CD (left) and extinction (right) spectra of the S-Au NRs from Figure 2.6b which is grown by using L-cysteine molecules. For comparison, the optical data acquired from the R-Au NRs that possess the same dimensions but were grown using D-cysteine instead are also presented (blue data points). Both R- and S- chiral Au NRs exhibit almost identical op-tical extinction features, and two absorption peaks at 525 nm and 660 nm can be attributed to the transverse and longitudinal LSPR modes of the Au NRs,

respectively[73]. Meanwhile, their CD spectra show the opposite signs with peaks at 530 nm and 660 nm.

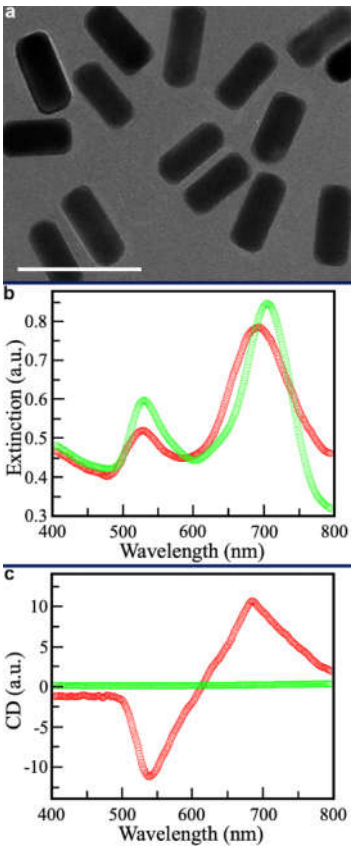

Figure 2.8. Overgrowth of chiral Au NRs by using binary surfactants mixture. (a) Typical TEM image showing that overall morphology of Au NRs become more even after the overgrowth. Scale bar, 20 nm. (b) Experimental extinction spectra before (red) and after (green) overgrowth. Small red shifts of both transverse and longitudinal peak wavelengths are observed after overgrowth due to the size increase. (c) Experimental CD spectra before (red) and after (green) overgrowth.

In order to elucidate the underlying mechanism of observed chirality in the Au NRs, we have performed two control experiments. First, we have re-moved surface ligand molecules after growth of chiral Au NRs by a ligand exchange process with achiral oleylamine molecules, and redispersed the chiral Au NRs in toluene, and we have observed that the CD features remain almost unchanged. This observation excludes

the role of possible residue chiral molecules on the surface[74,75]. Second, we have modified chiral overgrowth conditions and coated additional Au layers onto chiral Au NRs by using a binary surfactant mixture of cetyltrimethylammonium chloride and sodium oleate (Figure 2.8). This modified overgrowth condition led to an even morphology of NRs, and those inhomogeneous structural features that are originally observed from the chiral Au NRs disappear (Figure 2.6c and Figure 2.7). Correspondingly, the CD features measured after this second overgrowth almost completely disappear. This control experiment unambiguously suggests that our observed CD in Figure 2.6d originates from the boundary morphology itself, rather than other mechanisms. Similar to the CD mechanism observed in chiral Au NCs that is attributed to the existence of prevailing chiral high Miller index facets on the surface, we propose that the prevailing chiral high Miller index facets exist on both ends of the chiral Au NRs as schematically shown in Figure 2.6a. The exposure of chiral high Miller index facets at the ends of NRs originates from the kinetically controlled overgrowth reaction, and the adsorption of chiral molecules onto enantioselected chiral high Miller index facets breaks the symmetry and thus promotes the formation of each enantiomorph dependent upon the molecular chirality. Based on this proposed mechanism, a structural model of a chiral Au NR is constructed and presented in Figure 2.6c to compare with its corresponding TEM image, showing excellent agreement. More importantly, we have computed the CD and extinction spectra by using the structural model in Figure 2.6c, and presented the results in Figure 2.6e. The excellent agreement between our experimental (Figure

2.6d) and simulation (Figure 2.6e) results has validated our proposed CD mechanism as well as our structural model in Figure 2.6c.

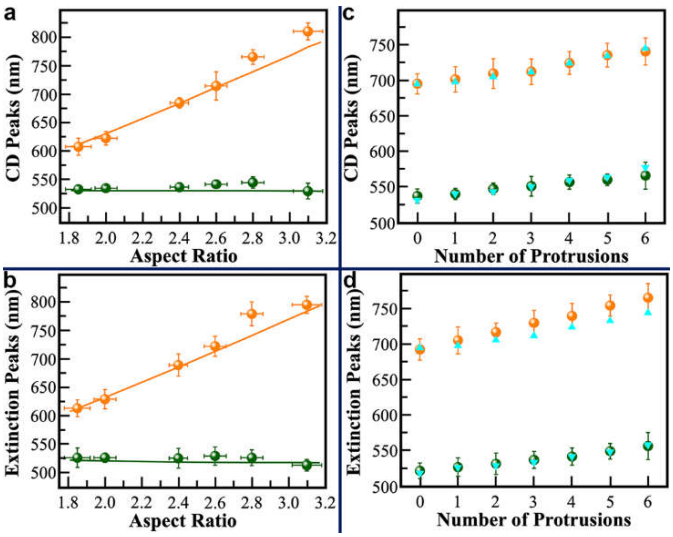

Figure 2.9. The dependence of handedness of chiral Au NRs on the AR and the apex protrusions. (a) & (b) Evolution of peak wavelengths in CD and extinction spectra with the AR, respectively. Both transverse (green spheres) and longitudinal peaks (orange spheres) are presented and compared. The green and orange lines are data from simulation for transverse and longitudinal peaks, respectively. (c) & (d) Evolution of peak wavelengths in CD and extinction spectra with the average number of protrusion features at the ends of chiral NRs, respectively. Both transverse (green spheres) and longitudinal peaks are presented and compared. The cyan upper and down triangles are simulation data for longitudinal and transverse peaks, respectively. The experimental uncertainty of the AR is determined by counting more than 500 nanostructures from TEM images of each sample. The experimental uncertainty of peak wavelength is estimated by the Gaussian peak fit error.

Our experimental observations and proposed mechanism of induced chirality in both Au NCs and NRs immediately suggest that such nanoscale chirality can be further engineered by designing and tailoring their dimensions and boundary morphology. Figure 2.9 highlights two examples of such chirality control. For regular achiral Au NRs, their optical properties have been demonstrated to be dependent on the AR[76].

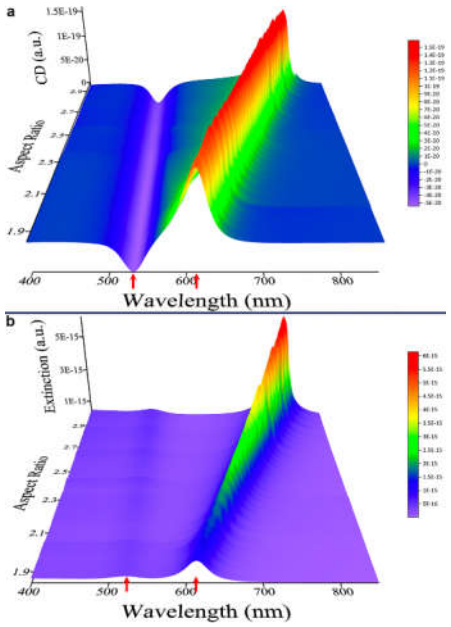

Figure 2.10. Evolution of optical properties of chiral Au NRs with the AR by FEM simulation. (a) & (b) Simulated CD and extinction spectra as a function of the AR of chiral Au NRs, respectively.

By using our proposed CD mechanism and model of chiral Au NRs in Figure 2.6, we have evaluated theoretically the evolution of both CD and extinction spectra with the AR of chiral Au NRs while keeping the other structural parameters the same, and we present the results in Figure 2.10. Experimentally we have achieved chiral Au NRs with different AR but similar width of 18.3 ± 0.5 nm (Figure 2.11), and we have measured their CD and extinction spectra with results presented in Figure 2.12. It can be seen that although all samples with different AR show similar characteristics in both CD and extinction spectra and both transverse and longitudinal LSPR modes are observed, the longitudinal mode in both CD and extinction spectra manifests strong dependence on the AR but the transverse mode does not. In order to compare experimental with computational results, we have extracted peak wavelengths of both trans-verse and longitudinal LSPR modes from the CD and extinction spectra, and

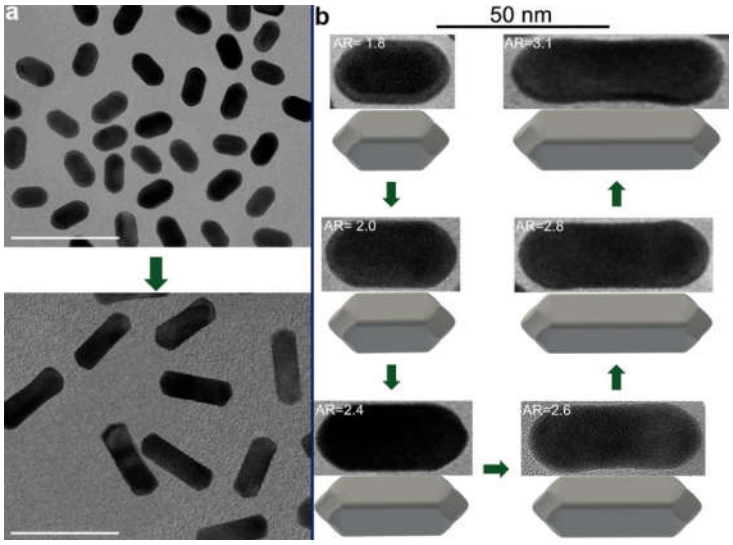

Figure 2.11. Tuning the AR of chiral Au NRs. (a) Typical large-scale TEM images of chiral Au NRs with two different averaged ARs of 1.8 (top) and 3.1 (bottom). Scale bar, 100 nm. (b) TEM image and model of individual chiral Au NRs showing structural evolution with the AR. Structural model for each AR is also used for FEM computation in Figure 2.10.

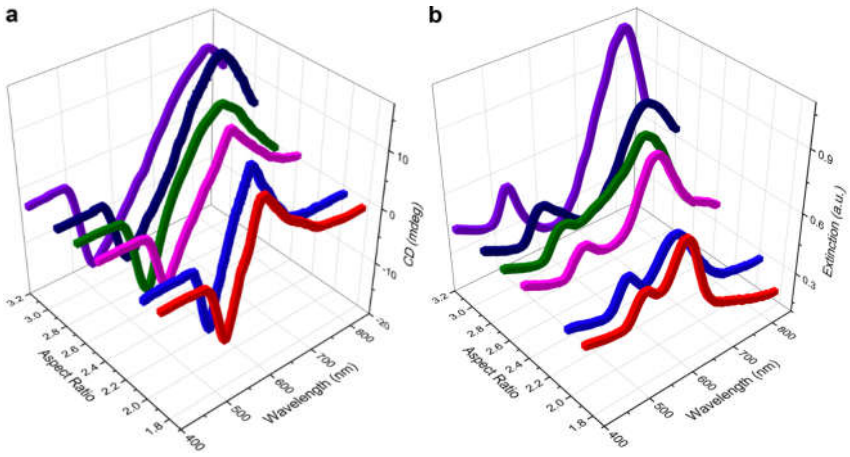

Figure 2.12. Experimental optical spectra of chiral Au NRs with different AR. (a) CD spectra. (b) Extinction spectra. Data were acquired from samples summarized in Figure 2.11.

summarized their results in Figure 2.9a and 2.9b, respectively. It can be clearly seen that the variation tendency seen in our experimental results agrees very well with the theoretical prediction, and both the CD and extinction wavelengths of the longitudinal mode show strong dependence on the AR, while the corresponding peak wavelength

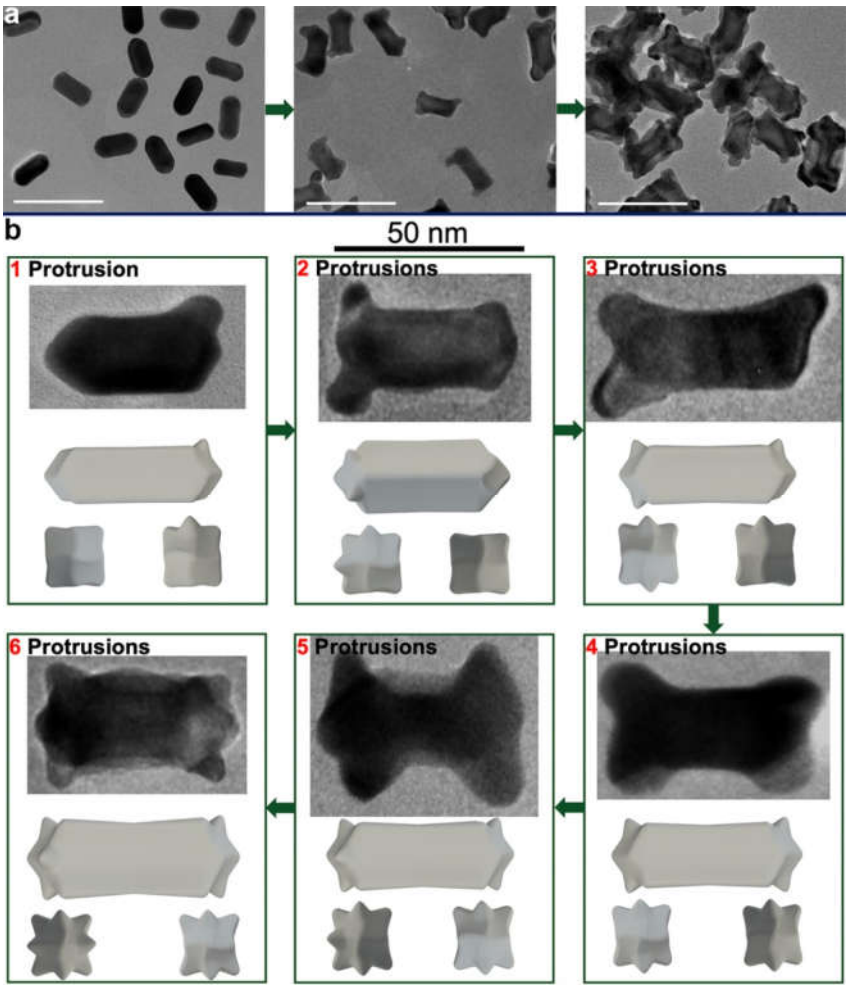

Figure 2.13. Control of structural protrusions at the apex of chiral Au NRs. (a) Typical large-scale TEM images of chiral Au NRs with different number of protrusions at the ends of Au NRs. Three examples, 0 protrusion, 2 protrusions and bone-shape are presented to show the overall quality of samples in this control experiment. Scale bar, 100 nm. (b) Representative TEM image and structural model of individual chiral Au NRs with evolution of different number of protrusions at the ends. For model, side view and two end views are provided for clarification purpose. These are also the models utilized for FEM computation presented in Figure 2.14.

of the transverse mode remains almost unchanged, as it is mainly determined by the width of chiral Au NRs.

Our observed CD of chiral Au NRs originates from the prevailing chiral facets exposed at the ends of chiral NRs, suggesting that if such chiral facets (and thus the

end morphology) can be tailored it should offer an important way to finely tune and enhance its induced handedness. Indeed, by employing a layer-by-layer overgrowth process onto the starting chiral Au NRs, we have found that the boundary morphology at both ends of NRs evolves from a simple chiral concave rhombic dodecahedron (Figure 2.6) to a more intricate shape with multiple protrusions at the end, and the average number of such structural protrusions can be controlled from single protrusion to a bone-shaped morphology with more than six protrusions (Figure 2.13). The appearance of protrusions can be understood by the kinetically controlled overgrowth condition, in which the over-growth at corners is favored over facets. We have performed optical measurements on a series of samples with different numbers of protrusions, and summarized the results in Figure. 2.14a and 2.14b. Based on the morphologies of protrusion structures, we have also constructed corresponding models (Figure 2.13) and computed their chiroptical responses to account for the effect of such morphological protrusions (Figure 2.14c and 2.14d). In order to compare experimental with theoretical results and to validate the underlying CD origin and model, we have acquired peak wavelengths from experimental and simulated CD and extinction spectra, and summarized results in Figure 2.9c and 2.9d. It can be seen that both the CD and extinction spectra of resultant chiral Au NRs with protrusions vary consistently with total number of protrusions at the ends, which can be fully rationalized by our modeling. Thus far, the consistency between our experimental results and theoretical computations and modeling for all different chiral Au NCs and NRs has validated our pro-posed chiral mechanism in this important

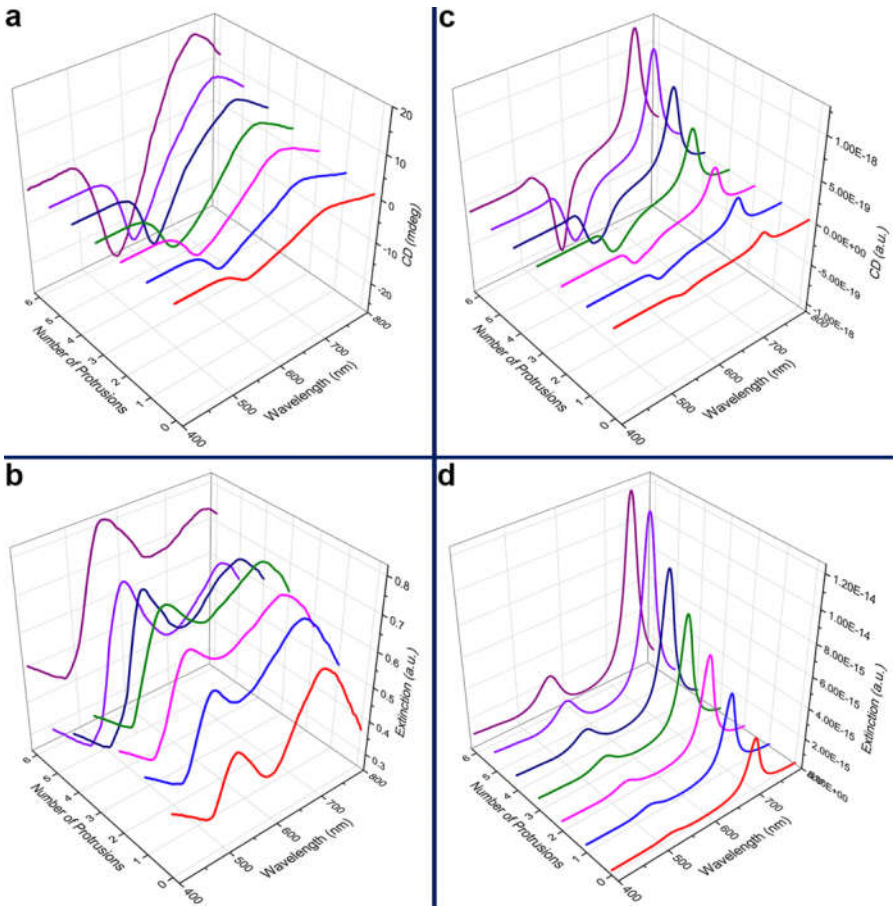

Figure 2.14. The CD and extinction spectra of chiral Au NRs with different number of protrusions at the ends. (a) & (b) Experimental CD and extinction spectra, respectively. (c) & (d) Computed CD and extinction spectra by using the model presented in Figure 2.13, respectively.

class of plasmonic chiral metal nanostructures, offering a guideline to further tailor CD characteristics of chiral nanostructures from the bottom-up.

2.2.4 Chiral hybrid metal-semiconductor nanostructures

It is worth noting that different from other mechanisms for inducing chirality in plasmonic nanostructures by either electromagnetic coupling or assembly, the boundary morphology induced handedness of metal nanostructures has been demonstrated in Figure 2.9 to be very robust with various controls, thus offering a

viable bottom-up chiral materials platform for developing more complex and functional chiral hybrid nanostructures that can potentially integrate different functionalities within a single nanoscale entity to enable synergistic couplings (Figure 2.2), and to explore the emerging chirality-dependent physics and chemistry. For example, exotic nanoscale resonant plasmon-exciton coupling has been achieved in achiral hybrid metal-semiconductor nanostructures [61,62,77]. If similar hybrid nanostructures can be achieved with chiral plasmonic nanostructures, like the chiral Au NCs and NRs from our current work, chirality should provide a new degree of freedom to control nanoscale spin or enantioselective photocatalysis by a chiral local plasmonic field. Figure 2.15 demonstrates the feasibility of developing a new class of chiral hybrid nanostructures and to investigate the evolution of structural and optical characteristics in such hybrid nanostructures. We start with chiral *S*-Au NRs with bone-shaped end morphologies that retain strong CD (Figure 2.13a). Typically, a 2 ml of chiral Au NRs is mixed with 1 ml of 0.2 M CTAB, 30 µl of 0.01 M AgNO3 and 50 µl of 0.1 M ascorbic acid. The pH of the solution is adjusted to ~10 by using NaOH. After aging for 5 mins, the solution is centrifuged twice at 13200 rpm for 10 min, and the product (Au-Ag NRs) is re-dispersed in 2 ml of 0.2 M CTAB. To convert metal Ag shell of Au-Ag NRs to semiconductor Ag_2S shell, the above Au-Ag core-shell NRs solution is mixed with 20 µl of 0.4 mM Na_2S solution. After aging for 30 mins, the solution is centrifuged twice at 13200 rpm for 10 min, and the product (chiral Au-Ag_2S NRs) is dispersed in 2 ml of 0.2 M CTAB. The chiral Au-CdS NRs is achieved by cation exchange process. Typically, the above Au-Ag_2S NRs solution is mixed with 20 µl of 80 mM $Cd(NO3)_2$ solution. The solution is stirred at 60 ^oC, followed by

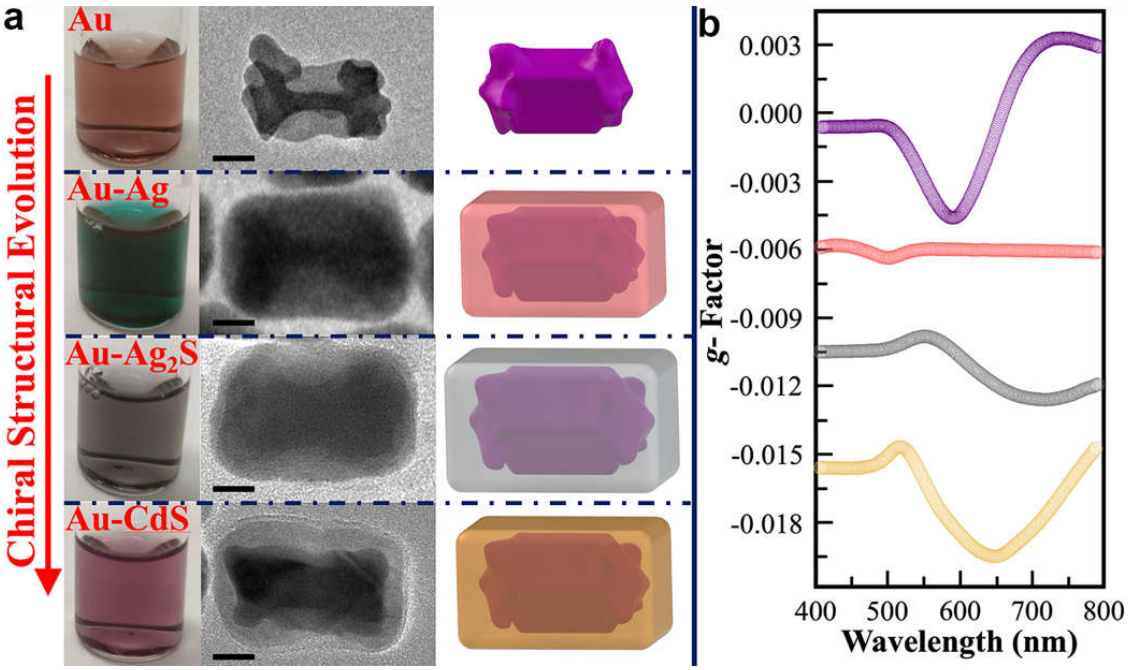

Figure 2.15. Development and characterization of chiral hybrid nanostructures. (a) Step-by-step chiral structural evolution (top to bottom in figure) from chiral metal Au NRs with bone-shape morphology, to Au-Ag core-shell, to Au-Ag_2S and to Au-CdS metal-semiconductor core-shell NRs by chemical conversion. For every step, solution in a glass vial showing good sample dispersion and color (left), TEM image of individual nanostructure with scale bar of 20 nm (middle) and its corresponding model (right) are presented. (b) Experimental dissymmetry *g*-factor measured at each step. Purple, pink, gray and yellow data curves were acquired from the Au, Au-Ag, Au-Ag_2S and Au-CdS NRs, respectively. For comparison and clarity purpose, the curves of the Au-Ag, Au-Ag_2S and Au-CdS NRs are vertically shifted by -0.006, -0.0105 and -0.0155, respectively.

addition of 5 µl of tributylphosphine. The cation exchange process continues for 2 hrs. The solution is centrifuged twice at 13200 rpm for 10 mins, and the product (chiral Au-CdS NRs) is dispersed in DI water. Figure 2.15a and Figure 2.16 show the step-by-step structural and compositional evolution characterized by TEM imaging, with a schematic model, and the corresponding variation of optical properties of different hybrid nanostructures can be evident by examining the color of solutions. We have found that although the starting chiral Au NRs possess bone-shaped end morphology, the overall Au (core)-Ag (shell) NRs become regular rectangular

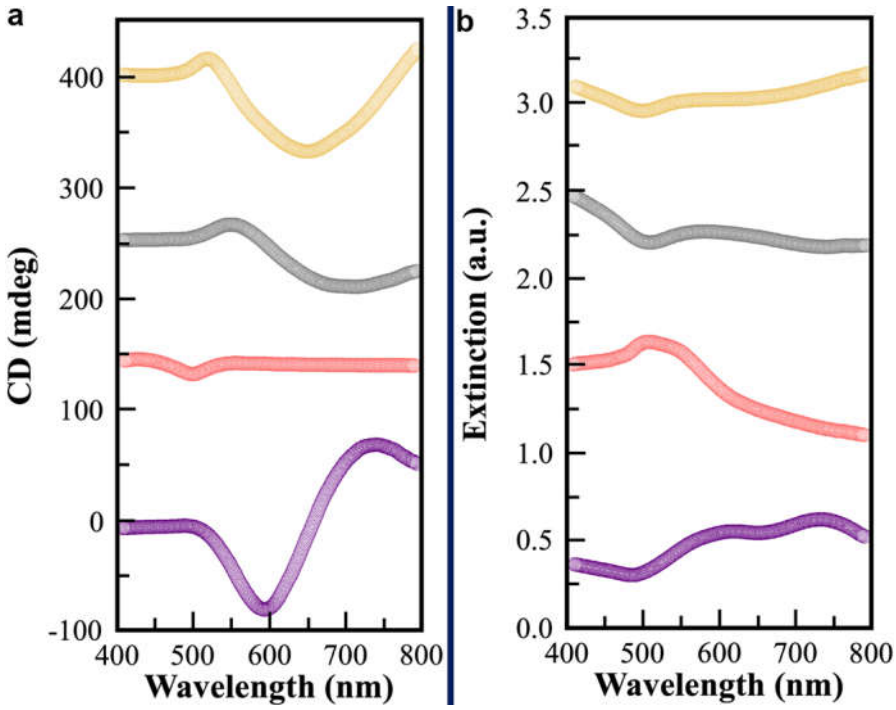

Figure 2.16. Step-by-step optical characterization of hybrid chiral NRs by chemical conversion. (a) & (b) Experimental CD and extinction spectra, respectively. Purple, pink, gray and yellow data curves are acquired from Au, Au (core)-Ag (shell), Au (core)-Ag_2S (shell) and Au (core)-CdS (shell) NRs, respectively. For comparison and clarity purpose, the CD curves of the Au-Ag, Au-Ag_2S and Au-CdS NRs are shifted vertically by 140, 250 and 400, respectively, while the extinction curves of the Au-Ag, Au-Ag_2S and Au-CdS NRs are shifted vertically by 0.85, 1.6 and 2.5, respectively.

cuboids after the overgrowth of the Ag shell while the bone-shaped Au NRs remain intact and visible in the TEM images. The subsequent chemical conversions from the metal Ag to dielectric semiconductor shells (both Ag_2S and CdS) do not alter either the overall cuboid morphology or the central bone-shaped Au core, highlighting the robustness of as-synthesized chiral Au NRs.

We have studied the evolution of CD characteristics (Figure 2.16), and compared the corresponding dimensionless dissymmetry factor (g-factor) in Figure 2.15. There are a few important observations that can be immediately identified from Figure 2.15b:

First and foremost, the hybrid Au-Ag_2S and Au-CdS nanostructures manifest strong CD that originates from the chiral Au core NRs. This observation is consistent with our TEM result confirming that chiral Au NRs remain intact even after multiple overgrowth and harsh chemical conversion processes. This again can be attributed to the robust chirality mechanism by chiral boundary morphology in Figure 2.2; Second, the CD of the Au-Ag core-shell NRs almost disappears after overgrowth of the Ag shell, but is recovered once the Ag shell is converted to the semiconductor Ag_2S shell in the Au-Ag_2S hybrid NRs. The revival of CD features in the Au-Ag_2S hybrid NRs suggest that the chirality of Au NRs is sustained in the process, however the disappearance of CD in the Au-Ag core-shell NRs can be attributed to the fact that both Au and Ag are conductive and the overall morphology of the Au-Ag core-shell NRs becomes even, and the plasmonic electrons are delocalized on the surface of entire core-shell NRs. As a result, the effect of the chiral boundary morphology of Au NRs becomes negligible to the delocalized plasmonic electrons; Lastly, although the CD features are recovered in the hybrid Au-Ag_2S and Au-CdS metal-semiconductor NRs, both the CD peak wavelengths and intensities are varied as compared with the starting chiral Au NRs. Qualitatively, such variation can be attributed to the difference in the dielectric constant of semiconductor shell in the hybrid nanostructures. A more thorough and quantitative comparison is currently under investigation.

2.3 Conclusion

We have developed a facile synthetic method to induce and engineer chirality of small-sized plasmonic Au NCs and NRs from the bottom-up, having achiral crystallographic

lattices. Both experimental and theoretical results have suggested that the observed chirality originates from the nanoscale chiral boundary morphology induced by the broken symmetry of chiral high Miller index facets and is very robust. Because of their small size and robustness of chirality, these as-synthesized nanoscale chiral plasmonic structures can serve as chiral functional building blocks. We have demonstrated a new class of chiral hybrid nanostructures that can integrate multi-functionalities, including chirality, plasmons and excitons at the nanoscale. Our current work opens up a few emerging research avenues. For example, although we have utilized Au as an example, the chiral mechanism based on broken symmetry of chiral high Miller index facets should be general and be readily applied to other achiral inorganic metals. As compared with existing mechanisms for inducing chirality at the nanoscale, chiral boundary morphology in inorganic nanocrystals should offer a robust mechanism for preserving CD characteristics for many practical applications, including enantioselective catalysis. Additional importantly, the availability of hybrid chiral metal-semiconductor nanostructures as demonstrated in our work should offer a new and unique pathway to study various entangled chirality effects, including chirality induced spin selectivity and chiral hot electrons at the nanoscale[78,79].

Chapter 3: Intrinsic Plasmon-Chiral Coupling in the Emerging Hybrid Chiral Nanostructures: A Coupled-Oscillators Analysis

3.1 Introduction

Chiral objects, possessing non-superimposable mirror images often termed as "left-handed" or "right-handed", exhibit distinct properties and behaviors, playing pivotal roles across diverse fields, ranging from chemistry and biology to physics and photonics. For instance, chiral molecules are crucial for numerous biological processes in nature, with their selective interactions with receptors underpinning critical functions such as drug binding and enzyme catalysis[1]. Despite the broad significance of chirality, the majority of research has historically focused on small organic molecules due to their prevalence and synthetic accessibility. However, recent years have witnessed a growing interest in exploring chirality in inorganic materials. Inorganic chiral materials, including chiral metallic and chiral semiconductor nanostructures, offer unique avenues to broaden our understanding and applications of chirality beyond the organic domain[45,80]. These materials exhibit intriguing optical, spintronic and phononic properties, driven and tailored by their chiral geometry and crystal structure, surpassing what can be achieved by organic chiral molecules alone[39,81-84]. Particularly, recent development in bottom-up synthesis techniques have facilitated the creation of emergent inorganic chiral hybrid nanostructures comprising chiral subunit and other functional components[55,62,85]. For instance, integration of achiral plasmonic nanostructures, such as gold and silver metal nanoparticles and nanorods that possess localized surface plasmon resonances (LSPR), with chiral subunits in a hybrid

nanostructure presents an exciting opportunity[16,67]. This integration allows for the exploitation of the distinctive optical properties of both components, resulting in novel chiral hybrid light-matter states and precise control over chiral light-matter interactions at the nanoscale[23,86-88]. However, the study of such hybrid chiral systems remains nascent, and there is pressing need for theoretical investigations to elucidate the underlying coupling physics between LSPR and chiral objects. Herein, a general coupled-oscillators model has been developed to unveil inherent LSPR-chirality coupling in hybrid nanostructures. Predictions from this model indicate various LSPR-mediated chiral effects depending on inherent coupling strengths within the hybrid nanostructure, offering valuable insights to guide the design of chiral hybrid nanostructure with desired chiroptical properties and functionalities. Furthermore, full wave simulation incorporating chiral constitutive equations has been employed to evaluate specific hybrid nanostructures, showcasing excellent agreement with predictions by the coupled oscillators model. Understanding the intrinsic chiral-plasmonic coupling in a hybrid nanostructure holds promise for precise design and innovative applications in areas such as quantum sensing, enantioselective catalysis and chiral optoelectronics[41,79,89-92]. Further theoretical and experimental studies on the coupling between LSPR and chiral objects are imperative for unlocking new functionalities and advancing the development of next-generation chiral nanophotonic devices.

3.2 Oscillator model

3.2.1 Three coupled oscillator model

Figure 3.1 shows schematics of a three-coupled-oscillators model for a chiral hybrid nanostructure consisting of an achiral plasmonic subunit and a chiral subunit with dominant one-dimensional plasmons-chiral coupling. Briefly, in this model, the chiral subunit can be generically described by the Born-Kuhn model[3,93], involving two separated but coupled oscillators along $\boldsymbol{x}$ and $\boldsymbol{y}$ directions, respectively, with a physical separation distance D along $\boldsymbol{z}$ direction and chiral coupling strength $g_{12} = g_{21}$. Qualitatively, under excitation of left or right circularly polarized light with $\boldsymbol{k}$ vector along $\boldsymbol{z}$ and frequency ω, oscillations of the two oscillators for chiral subunit will be either constructive or destructive that is determined by D, leading to different oscillation magnitude and thus circular dichroism (CD). Furthermore, oscillators have also been widely utilized for describing various physical properties of nanoscale plasmonic systems[94,95]. In a hybrid chiral nanostructure consisting of both chiral subunit and achiral plasmonic subunit as illustrated in Figure 3.1, a three-coupled-oscillators model can be utilized by integrating the plasmonic oscillator with the Born-Kuhn chiral oscillators, which is governed by the equations as follows:

$$\begin{cases} u_1'' + \gamma_1 u_1' + \omega_1^2 u_1 + g_{12}u_2 + g_{13}u_3 = -N_c\left(\frac{e}{m}\right)E_1 e^{\frac{ikD}{2}}e^{-i\omega t} \\ u_2'' + \gamma_2 u_2' + \omega_2^2 u_2 + g_{12}u_1 + g_{23}u_3 = -N_c\left(\frac{e}{m}\right)E_2 e^{-\frac{ikD}{2}}e^{-i\omega t} \\ u_3'' + \gamma_3 u_3' + \omega_3^2 u_3 + g_{13}u_1 + g_{23}u_2 = -N_p\left(\frac{e}{m}\right)E_3 e^{-i\omega t} \end{cases} \quad (Eq.3.1)$$

The ω_i and γ_i are the intrinsic resonance frequency and damping parameter of the i-th oscillator, where the i=1 and 2 denote two coupled-oscillators representing chiral subunit and the i=3 is the plasmonic oscillator. The E_i is the projection of the external electric field of the incident light at the i-th oscillator. The $g_{ij}u_j$ represents the coupling interaction applied to the i-th oscillator by the j-th oscillator. The N_c and N_p represent the total number of chiral electrons and plasmonic electrons for chiral and plasmonic oscillators, respectively, which characterize the polarizability of the chiral subunit and plasmonic subunit within the hybrid nanostructure.

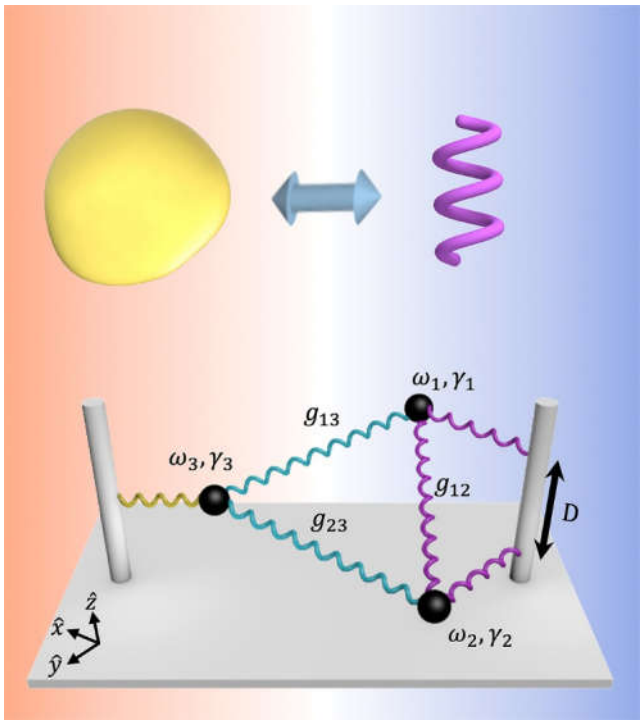

Figure 3.1. Schematic presentation of the three-coupled oscillator model (bottom) describing a hybrid chiral nanostructure (top) comprising an achiral plasmonic subunit (golden) and a chiral subunit (purple).

Different from the nonlocality tensor method that is often applied to calculate the CD of Born-Kuhn coupled oscillator[3,93], we have evaluated the CD of a hybrid chiral nanostructure by directly calculating the difference of energy loss of three oscillators in order to fully account for the integration of the plasmonic oscillator in Figure 3.1[96]. The energy loss of an oscillator system can be calculated by energy dissipation of the damping term of $\sigma_i = \frac{1}{2}\gamma_i\omega^2|u_i|^2$. The total CD from the hybrid nanostructure can therefore be evaluated as the difference of energy loss under left and right circularly polarized light and can be written as:

$$CD = \frac{1}{2}\gamma\omega^2 \sum_i \Delta|u_i|^2 \,, i = 1,2,3 \qquad (Eq.3.2)$$

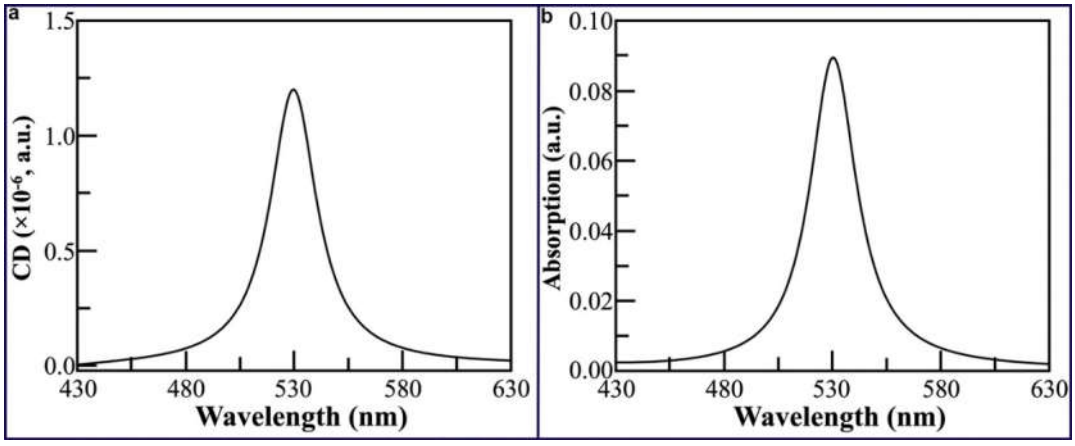

Figure 3.2. Chiral oscillator that is set to have CD peak at 530 nm and is utilized to couple with plasmonic oscillator in our multiple coupled oscillator models. (a) CD and (b) Absorption spectra by following parameters: $\omega_1 = \frac{3\times10^{17}}{530}s^{-1}$; $\omega_2 = \frac{3\times10^{17}}{370}s^{-1}$; $\gamma_1 = 2.8\times10^{13}s^{-1}$; $\gamma_2 = 2.8\times10^{13}s^{-1}$; $g_{12} = 10^{26}s^{-2}$; $D = 0.48\,nm$.

For all our computations in current work, we adopt $N_p/N_c = 100$ to account for different intensities of optical response by the plasmonic and chiral subunits in a hybrid nanostructure. The Born-Kuhn model has been applied to describe both non-degenerate and degenerate scenario depending on whether the frequencies of the two oscillators are the same or not to account for different line shapes of CD peak[97]. We have demonstrated (unpublished) that our model of hybrid chiral nanostructure in Figure 3.1 can be applied to both cases with similar underlying coupling physics, however to better illustrate intrinsic chiral physics and to compare with existing chiral semiconductors like chiral HgS or chiral perovskite nanostructures that have been achieved experimentally, we will use a non-degenerate single CD peak located at 530

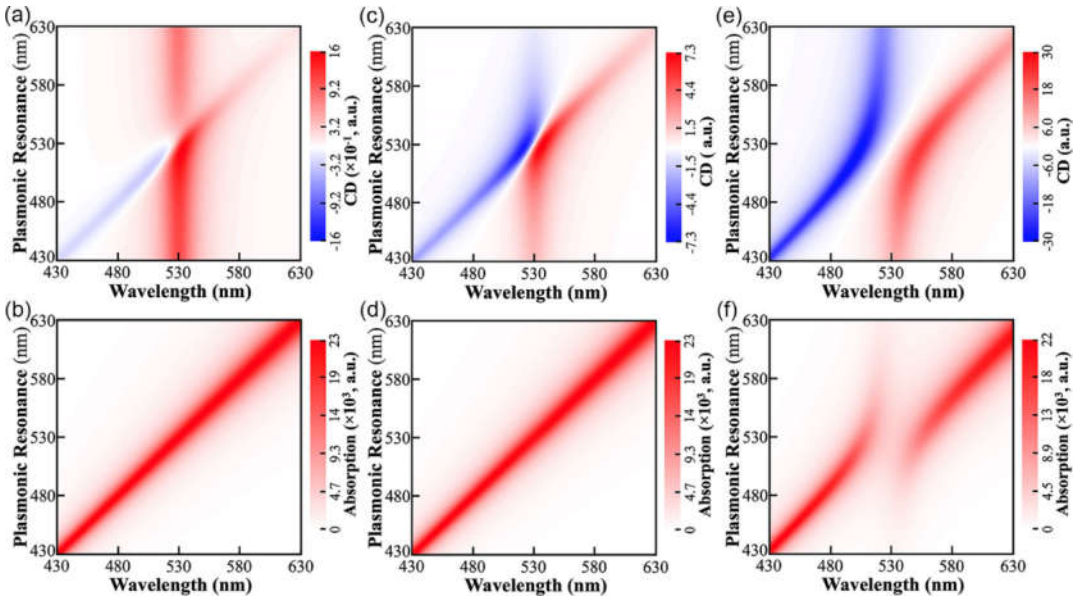

Figure 3.3. Variation of optical characteristics of a chiral hybrid nanostructure with its intrinsic coupling strength between chiral and plasmonic subunits. (a, b) Representative CD and absorption spectra in a weak coupling regime ($g_{13} = -3 \times 10^{26} s^{-2}$); (c, d) Representative CD and absorption spectra in a medium coupling regime ($g_{13} = -3 \times 10^{27} s^{-2}$); (e, f) Representative CD and absorption spectra in a strong coupling regime ($g_{13} = -3 \times 10^{28} s^{-2}$). The magnitudes of CD and absorption are normalized to the corresponding peak intensities of the uncoupled chiral subunit in Figure 3.2.

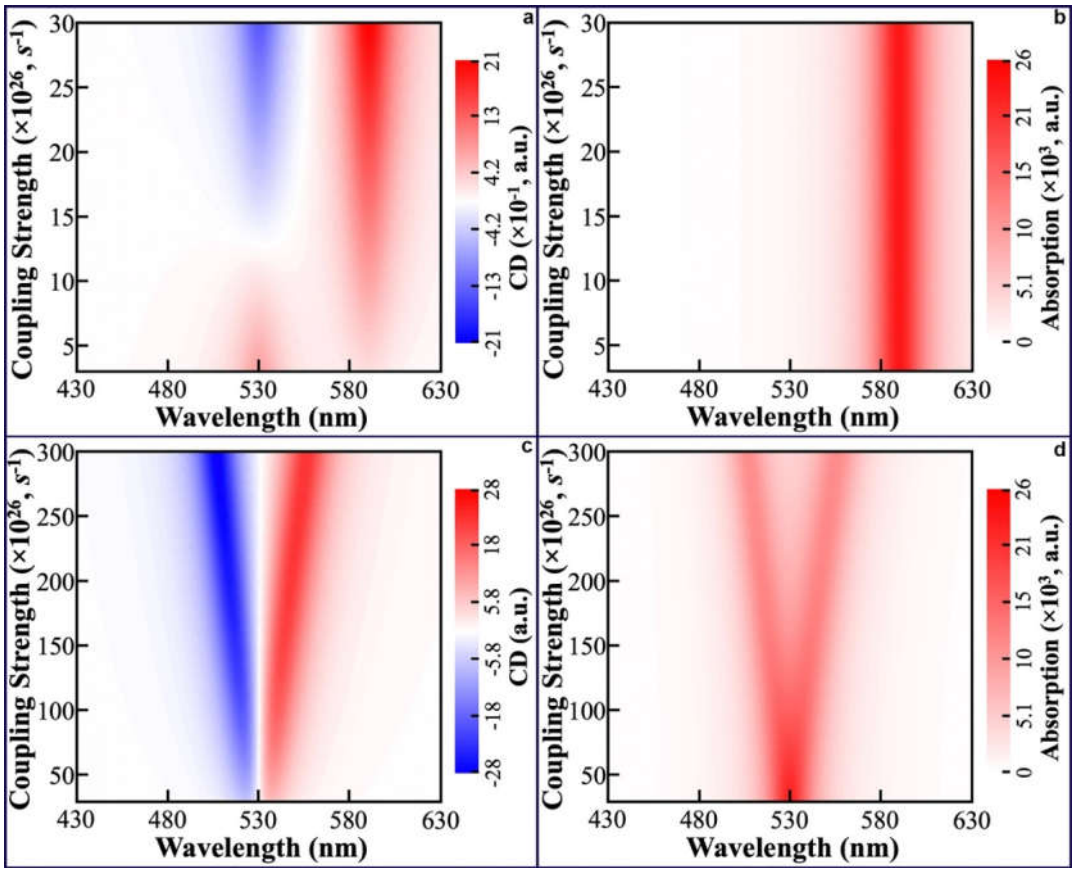

Figure. 3.4. Evolution of optical characteristics with continuously tuned plasmonic-chiral coupling strength across different regimes. (**a**, **b**) The CD and absorption spectra with variation in the coupling strength from weak to medium regimes, respectively. The LSPR wavelength is fixed at 590 nm. (**c**, **d**) The CD and absorption spectra with variation in the coupling strength from medium to strong regimes, respectively. The LSPR wavelength is fixed at 530 nm. The magnitudes of CD and absorption are normalized to the corresponding peak intensities of the uncoupled chiral subunit in Figure 3.2.

nm as an example (Figure 3.2) and explore plasmonic-chiral coupling by tuning the LSPR (ω_3) across this CD peak.

Figure 3.3 compares the total CD and absorption spectra of a hybrid nanostructure with three different intrinsic coupling strengths (i.e., g_{13} and g_{23}) between the plasmonic and chiral oscillators, with variations in the LSPR peak. The evolution of CD and absorption spectra with continuously tunable coupling strength at a fixed LSPR is also

depicted in Figure 3.4. Both Figure 3.3 and 3.4 clearly illustrate the existence of three different coupling regimes, each characterized by unique optical signatures. A notable emergent feature observed across all coupling strengths is the appearance of a new CD band coinciding with the LSPR, despite the plasmonic subunit itself being achiral. This evolving CD feature is termed as an induced plasmonic CD, which arises from confined electrons within the achiral plasmonic subunit, influenced by its neighboring chiral subunit. Across all coupling strengths, negative induced plasmonic CD is observed when the LSPR wavelength is shorter than the CD wavelength of the chiral subunit, and vice versa for positive induced plasmonic CD. Notably, similar observations of induced plasmonic CD have been predicted in scenarios involving plasmonic aluminum nanoparticle coupled to chiral molecules on their surface[98]. In the weak coupling regime, as illustrated in Figure 3.3a and Figure 3.4a, while the CD signal from the chiral subunit at 530 nm remains positive, its peak strength experiences a modest enhancement when the LSPR occurs at a shorter wavelength than the CD peak, and a reduction vice versa, compared to a pure chiral subunit without plasmonic coupling (Figure 3.2a). Importantly, as the coupling strength increases, dramatic modifications to the chirality signature of the chiral subunit can occur. A notable sign inversion from positive to negative CD peak of the chiral subunit is observed when the LSPR wavelength is tuned to be longer than that of CD peak (Figure 3.3c), while the optical absorption of the hybrid structure remains dominated by the achiral plasmonic subunit, akin to the weak-coupling regime (Figure 3.3b and 3.3d). In the strong coupling scenario, evident mode splitting is observed in both CD and absorption spectra (Figure 3.3e and 3.3f), with the degree of splitting increasing with the intrinsic coupling

strength (Figure 3.4c and 3.4d). The observation of cross splitting of the absorption spectra signifies the formation of plasmon-chiral hybrid states[99,100].

3.2.2 Understanding the underlying origins of the total CD

To understand the diverse CD signatures across weak, medium and strong coupling regimes in Figure 3.3, we have meticulously examined the origin of the observed total CD of a hybrid chiral nanostructure as follows. The time varying term, $e^{-i\omega t}$ doesn't appear in the calculation of CD and therefore for the following discussion, the time varying term, $e^{-i\omega t}$ in the equations can be omitted for simplicity, and the Eq. 3.1 can be rewritten as follows:

$$\begin{cases} -\omega^2 u_1 - \mathrm{i}\gamma_1 u_1 + \omega_1^2 u_1 + g_{12}u_2 + g_{13}u_3 = -N_c\left(\frac{e}{m}\right)E_1 e^{\frac{ikD}{2}} \\ -\omega^2 u_2 - \mathrm{i}\gamma_2 u_2 + \omega_2^2 u_2 + g_{12}u_1 + g_{23}u_3 = -N_c\left(\frac{e}{m}\right)E_2 e^{-\frac{ikD}{2}} \\ -\omega^2 u_3 - \mathrm{i}\gamma_3 u_3 + \omega_3^2 u_3 + g_{13}u_1 + g_{23}u_2 = -N_p\left(\frac{e}{m}\right)E_3 \end{cases} \quad (Eq.3.3)$$

To understand the underlying coupling physics between chiral and plasmonic oscillators, we can evaluate chiroptical responses of the coupled oscillator model by separating the external excitation of chiral oscillators and plasmonic oscillator in the system, and evaluate the Eq. 3.1 as the combination of two separated equation sets:

$$\begin{cases} -\omega^2 u_1 - \mathrm{i}\gamma_1 u_1 + \omega_1^2 u_1 + g_{12}u_2 + g_{13}u_3 = -N_c\left(\frac{e}{m}\right)E_1 e^{\frac{ikD}{2}} \\ -\omega^2 u_2 - \mathrm{i}\gamma_2 u_2 + \omega_2^2 u_2 + g_{12}u_1 + g_{23}u_3 = -N_c\left(\frac{e}{m}\right)E_2 e^{-\frac{ikD}{2}} \\ -\omega^2 u_3 - \mathrm{i}\gamma_3 u_3 + \omega_3^2 u_3 + g_{13}u_1 + g_{23}u_2 = 0 \end{cases} \quad (Eq.3.4)$$

$$\begin{cases} -\omega^2 u_1 - \mathrm{i}\gamma_1 u_1 + \omega_1^2 u_1 + g_{12}u_2 + g_{13}u_3 = 0 \\ -\omega^2 u_2 - \mathrm{i}\gamma_2 u_2 + \omega_2^2 u_2 + g_{12}u_1 + g_{23}u_3 = 0 \\ -\omega^2 u_3 - \mathrm{i}\gamma_3 u_3 + \omega_3^2 u_3 + g_{13}u_1 + g_{23}u_2 = -N_p\left(\frac{e}{m}\right)E_3 \end{cases} \quad (Eq.3.5)$$

In the Eq. 3.4, we only have non-zero excitation terms on chiral oscillators, i.e., $E_1 \neq 0$, $E_2 \neq 0$ and $E_3 = 0$. The solutions of the i-th oscillator of this equation set are denoted as $u_{ci\pm}$, where $i = 1, 2, 3$ and '+' and '−' stand for left circularly polarized (LCP) and right circularly polarized light (RCP), respectively; Similarly, in the Eq. 3.5, we only have non-zero excitation terms on plasmonic oscillators, i.e., $E_3 \neq 0$ and $E_1 = E_2 = 0$, and the solutions of the i-th oscillator of this equation set are expressed as $u_{pi\pm}$, where $i = 1, 2, 3$.

The total response of the *i*-th oscillator from the Eq. S15, u_i, can thus be expressed as the sum of $u_i = u_{ci} + u_{pi}$, where $i = 1, 2, 3$.

We thus have:

$$\left|u_{i\pm}\right|^2 = |u_{ci\pm} + u_{pi\pm}|^2 = \left|u_{ci\pm}\right|^2 + \left|u_{pi\pm}\right|^2 + u_{ci\pm}^* u_{pi\pm} + u_{ci\pm} u_{pi\pm}^* \quad (Eq.\ 3.6)$$

Correspondingly, the total CD (Eq. 3.2) can be obtained as:

$$CD = \frac{1}{2}\gamma\omega^2 \sum_i \Delta|u_i|^2 = \frac{1}{2}\gamma\omega^2 \sum_i \Delta\left(|u_{ci}|^2 + \left|u_{pi}\right|^2 + u_{ci}^* u_{pi} + u_{ci} u_{pi}^*\right) = CD_c + CD_p + CD_{cp} \quad (Eq.\ 3.7)$$

where $CD_c = \frac{1}{2}\gamma\omega^2 \sum_i \Delta|u_{ci}|^2$, $CD_p = \frac{1}{2}\gamma\omega^2 \sum_i \Delta\left|u_{pi}\right|^2$, and $CD_{cp} = \frac{1}{2}\gamma\omega^2 \sum_i \Delta\left(u_{ci}^* u_{pi} + u_{ci} u_{pi}^*\right)$, representing different chiral mechanisms.

We have evaluated those three different contributions separately as follows:

(1) The CD_c. The CD_c is only relevant to the excitation of chiral oscillators without the contribution of u_{pi}. Therefore, the CD_c originates from the excitation of chiral oscillators, and represents the intrinsic chiroptical response of chiral subunit in a hybrid nanostructure. Importantly, by comparing with the uncoupled chiral oscillator, the

intrinsic chiral response of chiral subunit in a hybrid nanostructure is modified by the existence of the adjacent achiral plasmonic subunit located within the hybrid nanostructure, and is characterized by the coupling strengths of g_{13} and g_{23}. From the perspective of energy flow and optical excitation, the CD_{c} originates from the excitation of chiral oscillators, and is dominated by the characteristics of chiral oscillator. However, the excitation of chiral oscillator under the external electromagnetic wave can be coupled to its adjacent plasmonic oscillator through the near-field plasmonic-chiral coupling. As a coupled system, all the oscillators could eventually reach dynamic equilibrium. To evaluate such near-field coupling effect here, the CD_{c} can be further quantitatively expressed by two contributions as $CD_c = CD_{\mathrm{g}} + CD_{NP}$, where the CD_{NP} represents the original CD of the pure chiral subunit without being coupled to the plasmonic subunit, and the CD_g originates from the near-field coupling by the plasmonic oscillator, which imposes a small but not negligible modification to the original CD_{NP}.

(2) The CD_p. The CD_p is only relevant to the u_{pi}. In order to compute the quantity of CD_p, we have evaluated excitation of the oscillators system by considering the LCP and RCP separately:

For the LCP excitation: $E = E(\hat{\boldsymbol{x}} + i\hat{\boldsymbol{y}})$, the Eq. 3.5 can be written as:

$$\begin{cases} -\omega^2 u_1 - \mathrm{i}\gamma_1 u_1 + \omega_1^2 u_1 + g_{12}u_2 + g_{13}u_3 = 0 \\ -\omega^2 u_2 - \mathrm{i}\gamma_2 u_2 + \omega_2^2 u_2 + g_{12}u_1 + g_{23}u_3 = 0 \\ -\omega^2 u_3 - \mathrm{i}\gamma_3 u_3 + \omega_3^2 u_3 + g_{13}u_1 + g_{23}u_2 = -N_p\left(\frac{e}{m}\right)E(\hat{\boldsymbol{x}} + i\hat{\boldsymbol{y}})\cdot\widehat{\boldsymbol{u_3}} \end{cases} \quad \text{(Eq. 3.8)}$$

For the RCP excitation: $E = E(\hat{x} - i\hat{y})$, the Eq. 3.5 can be written as:

$$\begin{cases} -\omega^2 u_1 - \mathrm{i}\gamma_1 u_1 + \omega_1^2 u_1 + g_{12} u_2 + g_{13} u_3 = 0 \\ -\omega^2 u_2 - \mathrm{i}\gamma_2 u_2 + \omega_2^2 u_2 + g_{12} u_1 + g_{23} u_3 = 0 \\ -\omega^2 u_3 - \mathrm{i}\gamma_3 u_3 + \omega_3^2 u_3 + g_{13} u_1 + g_{23} u_2 = -N_p \left(\frac{e}{m}\right) E(\hat{\boldsymbol{x}} - i\hat{\boldsymbol{y}}) \cdot \widehat{\boldsymbol{u_3}} \end{cases} \quad \text{(Eq. 3.9)}$$

The only difference between the Eq. 3.8 and Eq. 3.9 is the phase term of the external excitation: $(\hat{\boldsymbol{x}} + i\hat{\boldsymbol{y}}) \cdot \widehat{\boldsymbol{u_3}} = (\hat{\boldsymbol{x}} - i\hat{\boldsymbol{y}}) \cdot \widehat{\boldsymbol{u_3}} \cdot e^{\Delta\varphi}$, where $\Delta\varphi$ represents the phase difference. As a result, their corresponding solutions meet the relationship of $u_{pi+} = u_{pi-} \cdot e^{\Delta\varphi}$, leading to $|u_{pi+}| = |u_{pi-}|$. Consequently, we have concluded that the $CD_p = \frac{1}{2}\gamma\omega^2(\sum_i |u_{pi+}|^2 - \sum_i |u_{pi-}|^2) = 0$. This suggests that there is no net chiroptical response that can be induced by the plasmonic subunit at the absence of excitation of its alongside chiral subunit, although near-field plasmonic-chiral coupling exists.

(3) The $\boldsymbol{CD_{cp}}$. The CD_{cp} involves contributions from both u_{pi} and u_{ci}, strongly suggesting that its origin is the interplay of simultaneous excitations of plasmonic and chiral oscillators, and thus should play a key role in the hybrid nanostructure.

In summary, we can obtain the total CD as:

$$CD = CD_{cp} + CD_c = CD_{cp} + CD_g + CD_{NP} \quad \text{(Eq. 3.10)}$$

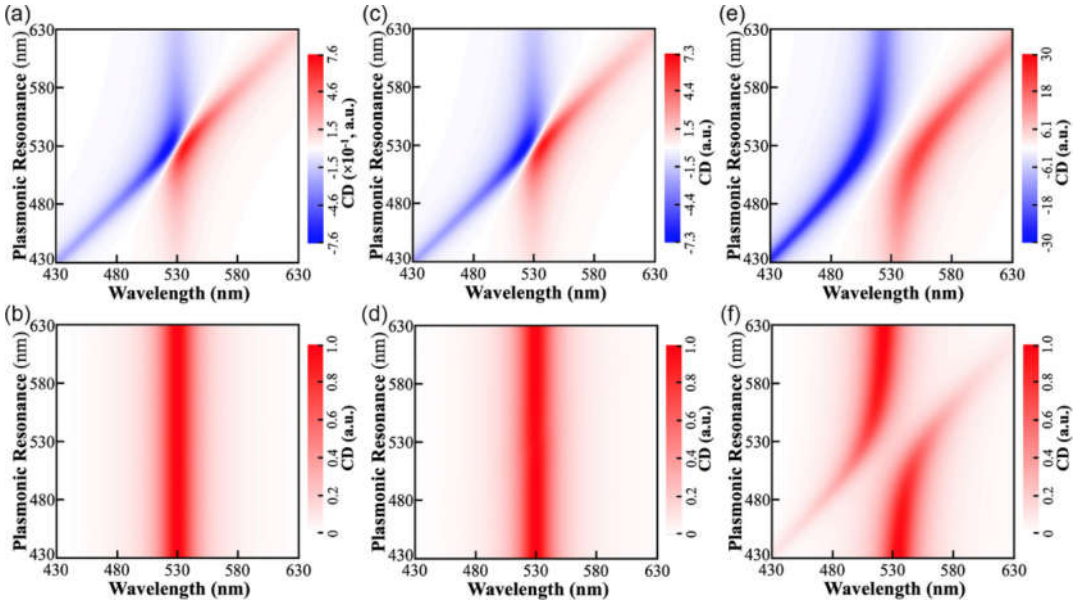

Figure 3.5. Decomposition of total CD based on two different mechanisms, CD_{cp} and CD_{c}. (a), (c), and (e) depicts CD_{cp} maps for weak, medium, and strong coupling examples illustrated in Figure 3.3, respectively. (b), (d), and (f) shows CD_{c} maps for weak, medium, and strong coupling examples illustrated in Figure 3.3, respectively. The magnitude of CD is normalized to the CD peak intensity of the uncoupled chiral subunit in Figure 3.2.

In our current work, we use non-degenerate Born-Kuhn model for chiral oscillator as an example to present and discuss the underlying coupling physics in a hybrid chiral nanostructure, and set the CD peak of pure chiral oscillator to be a positive single peak at 530 nm (Figure 3.2). For simplicity, the orientation of the plasmonic oscillator is set to be $\widehat{\boldsymbol{u_3}} = \hat{\boldsymbol{x}}$ and the chiral subunit is placed at its $\hat{\boldsymbol{x}}$ direction so that $\hat{\boldsymbol{r}} = \hat{\boldsymbol{x}}$. Therefore, we have:

$$\begin{cases} g_{13} = -e^2[3(\widehat{\boldsymbol{u_3}} \cdot \widehat{\boldsymbol{r_{13}}})(\widehat{\boldsymbol{u_1}} \cdot \widehat{\boldsymbol{r_{13}}}) - \widehat{\boldsymbol{u_1}} \cdot \widehat{\boldsymbol{u_3}}]\dfrac{1}{{r_{13}}^3} = -\dfrac{2e^2}{{r_{13}}^3} \\ g_{23} = -e^2[3(\widehat{\boldsymbol{u_3}} \cdot \widehat{\boldsymbol{r_{23}}})(\widehat{\boldsymbol{u_1}} \cdot \widehat{\boldsymbol{r_{23}}}) - \widehat{\boldsymbol{u_2}} \cdot \widehat{\boldsymbol{u_3}}]\dfrac{1}{{r_{23}}^3} = 0 \end{cases} \quad (Eq.3.11)$$

We have chosen three different coupling strengths, $g_{13} = -3 \times 10^{26} s^{-2}, -3 \times 10^{27} s^{-2}, and -3 \times 10^{28} s^{-2}$ to represent weak, medium and strong regimes,

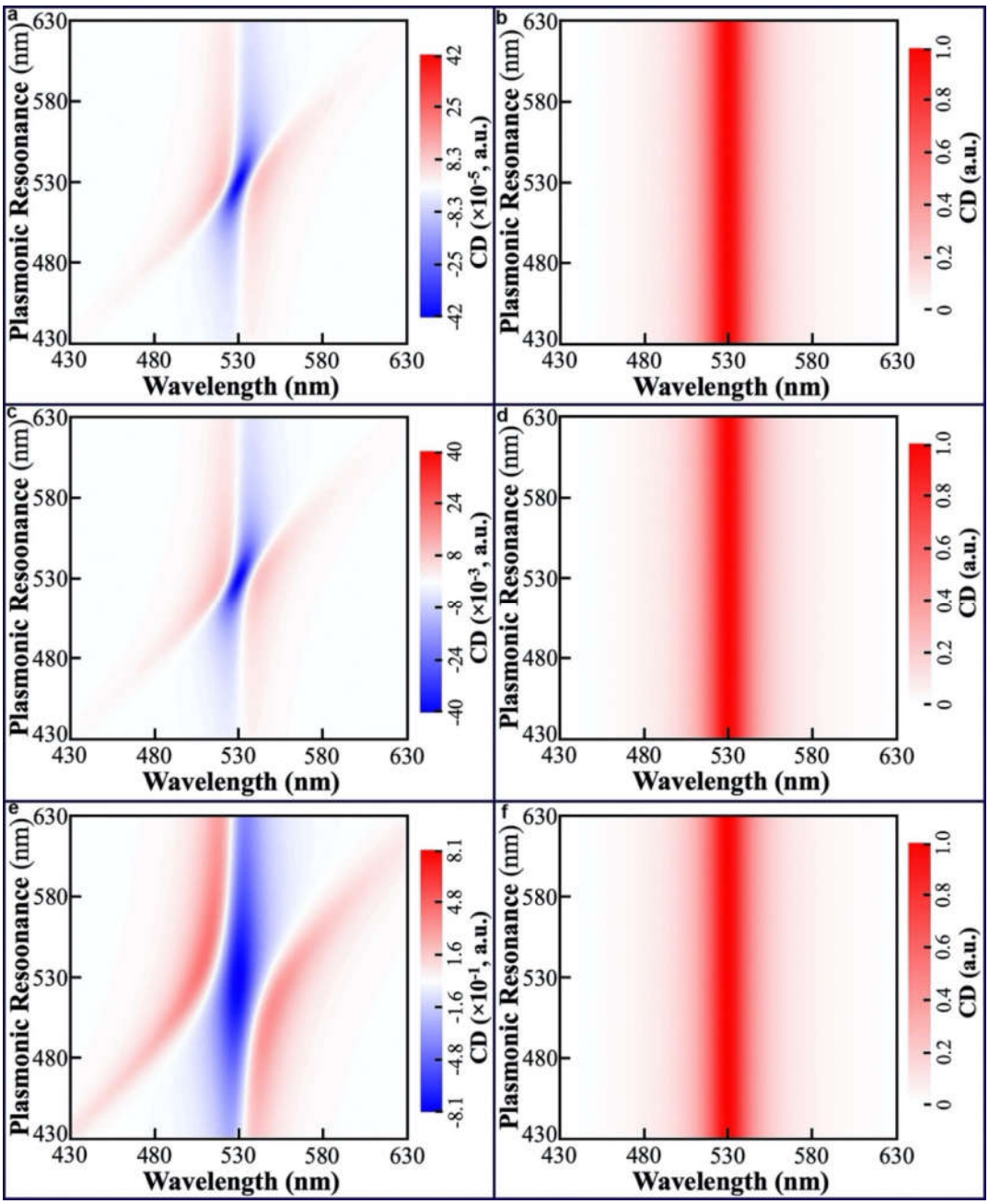

Figure 3.6. Two different chirality contributions to the CD_{c} : (**a**), (**c**) and (**e**) are CD_{g} maps for weak, medium and strong coupling examples illustrated in Figure 3.5, respectively. (**b**), (**d**) and (**f**) are CD_{NP} maps for weak, medium and strong coupling examples illustrated in Figure 3.5, respectively. The magnitude of CD is normalized to the CD peak intensity of the uncoupled chiral subunit in Figure 3.2.

respectively. We have investigated in-depth the total CD in the weak, medium and strong coupling regimes that are presented in Figure 3.3 and Figure 3.4, and present

their different contributions of CD_{cp} and CD_c in Figure 3.5, as well as two different contributions of CD_c, CD_g and CD_{NP}, in Figures 3.6-3.8.

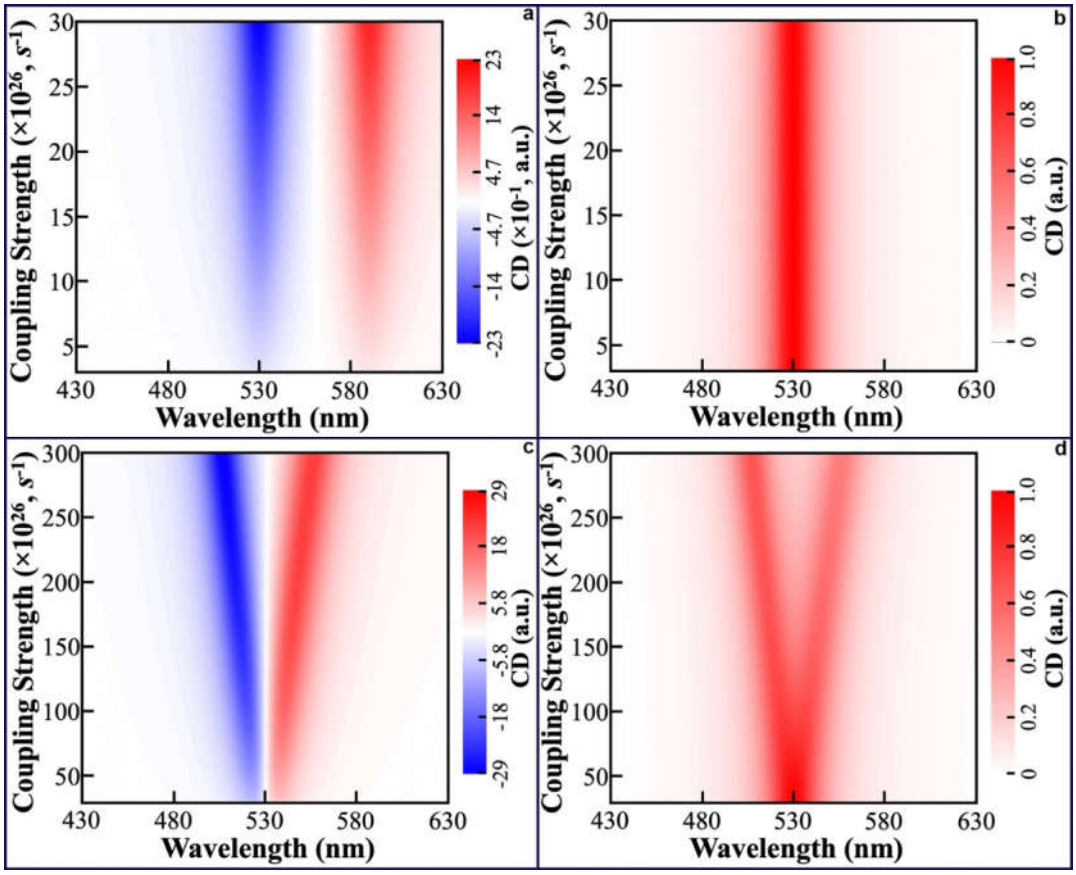

Figure 3.7. Decomposition of total CD in Figure 3.4 based on two different mechanisms, CD_{cp} and CD_{c} . (**a**) and (**c**) are evolution of CD_{cp} with inherent coupling strength from weak-to-medium and medium-to-strong coupling, respectively. (**b**) and (**d**) are evolution of CD_{c} with inherent coupling strength from weak-to-medium and medium-to-strong coupling, respectively. The magnitude of CD is normalized to the CD peak intensity of the uncoupled chiral subunit in Figure 3.2.

Figure 3.5 compares different contributions from CD_{cp} and CD_{c} in the weak, medium and strong coupling examples presented in Figure 3.3. Several key insights can be gleaned immediately: First, CD_{c} maintains a positive sign across all coupling scenarios. Particularly in weak and medium couplings, CD_{c} is predominantly influenced by the

pure chiral oscillator. While a slight modification to the original CD of the chiral oscillator occurs due to the presence of its neighboring plasmonic oscillator (Figure 3.6), this effect is relatively minor compared to the original CD strength from the chiral oscillator, owing to the absence of direct excitation of the plasmonic oscillator; Second, the coupling term, CD_{cp}, distinctly exhibits a phase reversal for all coupling strengths when the LSPR is tuned across the CD peak of the chiral oscillator. The consistent sign inversion in the CD_{cp} map arises from the phase change of the plasmonic oscillator through plasmonic near-field coupling inherent in a hybrid nanostructure. When LSPR peak coincides with CD peak of chiral oscillators, the plasmonic oscillation is in-phase with the driving electric field, resulting in a phase shift of zero degrees. When the excitation wavelength deviates from the LSPR peak, the phase shift between the plasmonic oscillation and the driving field becomes non-zero and opposite, depending on excitation at longer or shorter wavelength than the LSPR peak. Such phase change has led to Fano resonance with asymmetric line shape when a narrow resonance state is coherently coupled with a broad plasmonic feature[101-103]. Similarly, in a hybrid nanostructure where the plasmonic oscillator is coupled to chiral oscillators, at the original CD peak of the chiral oscillator, the LSPR of the plasmonic oscillator occurring at shorter or longer wavelength will exhibit an opposite phase shift of π, resulting in opposite phases of the local electric field by the plasmonic oscillator and serving as the excitation source of coupled chiral oscillators with a sign inversion at the CD peak; Third, while CD_{cp} exhibits consistent sign-inversion characteristics, its magnitude

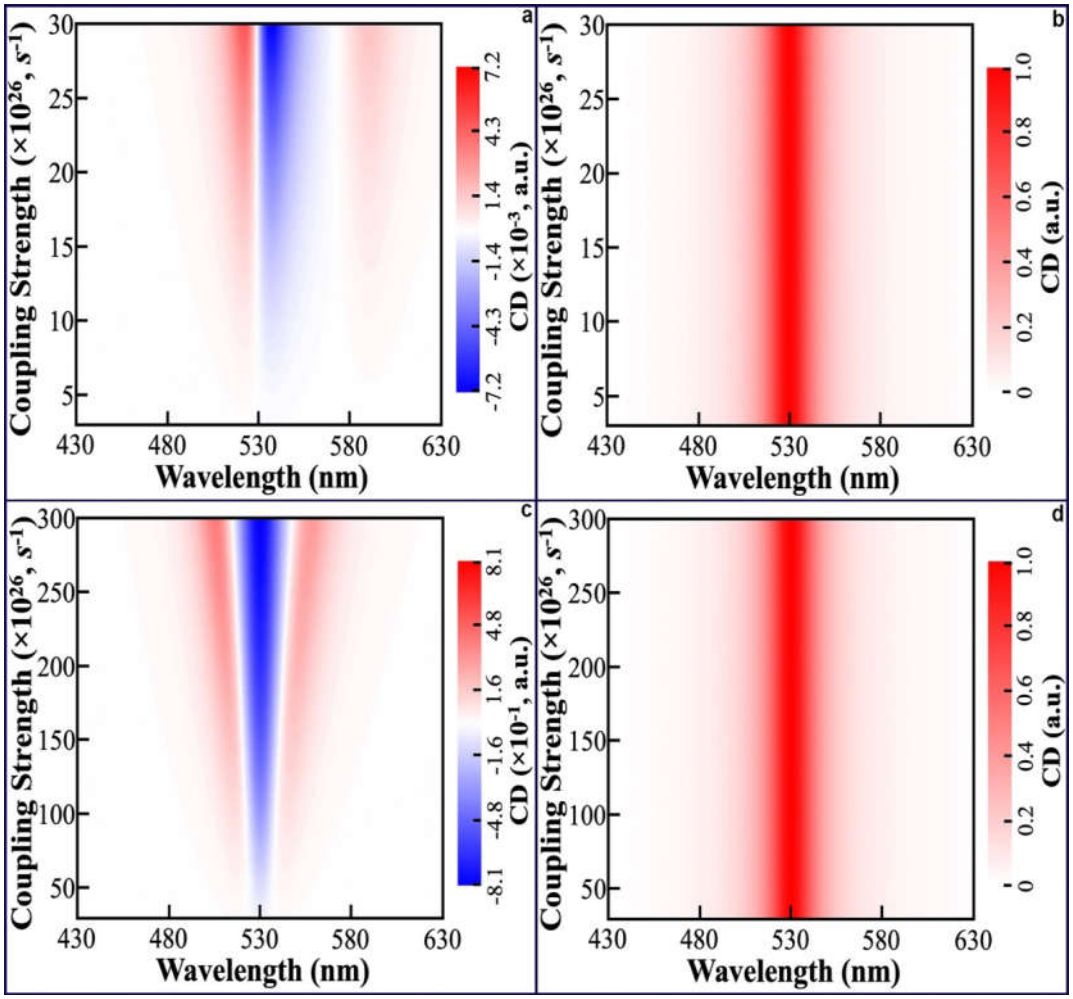

Figure 3.8. Evolution of two different contributions to the CD_{c} maps presented in Figure 3.7: (**a**) and (**c**) are evolution of CD_{g} contribution with inherent coupling strength from weak-to-medium and medium-to-strong coupling, respectively. (**b**) and (**d**) are evolution of CD_{NP} contribution with inherent coupling strength from weak-to-medium and medium-to-strong coupling, respectively. The magnitude of CD is normalized to the CD peak intensity of the uncoupled chiral subunit in Figure 3.2.

depends on the coupling strength between the chiral oscillator and the plasmonic oscillator, while CD_{c} remains relatively constant in the weak and medium coupling regimes. Consequently, the total CD results from the competition between near-field plasmonic coupling and direct external excitation of the chiral oscillator. In a weak coupling, direct external excitation of the chiral oscillator dominates, leading to sign

preservation (positive in Figure 3.3a). Conversely, in a medium coupling, near-field coupling originating from the plasmonic oscillator predominates, resulting in the observed sign-inversion in Figure 3.3c. This can be clearly seen in the evolution of CD with varying coupling strength in Figure 3.7 and 3.8; Lastly, in the strong coupling regime, both CD_{cp} and CD_{c} undergo significant modifications. Consequently, the optical characteristics in this scenario should be considered as the formation of a hybrid electronic state within a hybrid nanostructure, manifesting as clear mode splitting[23,104].

3.2.3 Four coupled oscillator model

It is noteworthy that while we have only considered one plasmonic oscillator coupling in Figure 3.1, our theoretical framework is versatile and readily extends to incorporate multiple oscillators. This capability allows for the description of more complex coupling scenarios, including high dimensional anisotropic coupling between the plasmonic subunit and chiral subunit in a hybrid nanostructure. For instance, if a hybrid nanostructure possesses a structural configuration where a chiral nanoparticle subunit is situated in the middle of a plasmonic nanorod subunit, couplings between the chiral subunit and both the transverse and longitudinal plasmonic modes of the plasmonic subunit must be considered concurrently. To address such two-dimensional anisotropic coupling, the model can be readily expanded by integrating an additional plasmonic oscillator into the existing three-coupled oscillator model, as depicted in Figure 3.9. The equations describing the general framework for the four-coupled oscillator

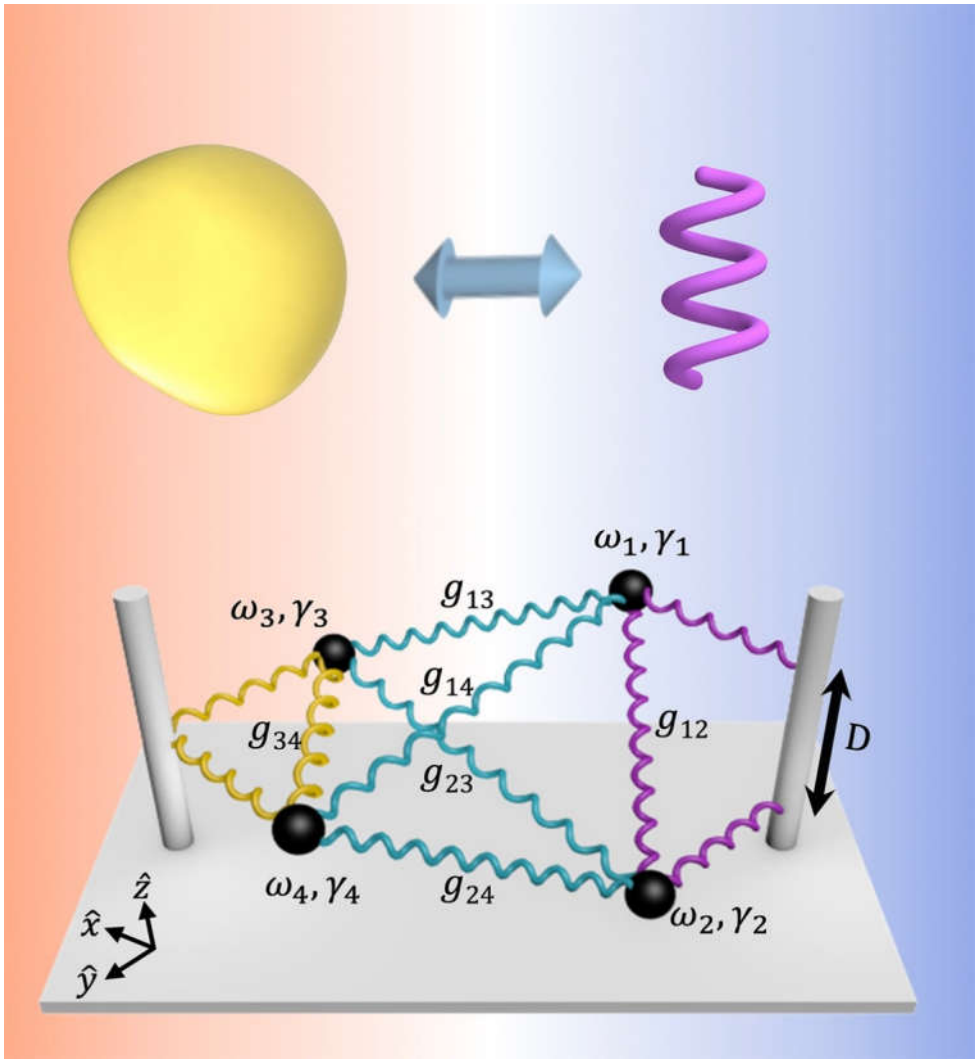

Figure 3.9. Schematics of a four-coupled oscillator model (bottom) to describe hybrid chiral nanostructure (top) possessing inherent anisotropic plasmonic-chiral coupling. The chiral subunit is described by a coupled Born-Kuhn coupled oscillator (1st and 2nd oscillators). To introduce anisotropy, two plasmonic oscillators are employed for achiral plasmonic subunit.

scenario can be formulated similarly to Eq. 3.1 for the three-coupled oscillator model, with addition of corresponding coupling terms:

$$\begin{cases} u_1'' + \gamma_1 u_1' + \omega_1^2 u_1 + g_{12}u_2 + g_{13}u_3 + g_{14}u_4 = -N_c\left(\frac{e}{m}\right)E_1 e^{\frac{ikD}{2}}e^{-i\omega t} \\ u_2'' + \gamma_2 u_2' + \omega_2^2 u_2 + g_{12}u_1 + g_{23}u_3 + g_{24}u_4 = -N_c\left(\frac{e}{m}\right)E_2 e^{-\frac{ikD}{2}}e^{-i\omega t} \\ u_3'' + \gamma_3 u_3' + \omega_3^2 u_3 + g_{13}u_1 + g_{23}u_2 + g_{34}u_4 = -N_3\left(\frac{e}{m}\right)E_3 e^{-i\omega t} \\ u_4'' + \gamma_4 u_4' + \omega_4^2 u_4 + g_{14}u_1 + g_{24}u_2 + g_{34}u_3 = -N_4\left(\frac{e}{m}\right)E_4 e^{-i\omega t} \end{cases} \quad (Eq.\ 3.12)$$

where u_4 is the displacement for the fourth oscillator for anisotropic plasmonic subunit with frequency of ω_4 and new couplings to both existing plasmonic oscillator ($g_{34} = g_{43}$) and chiral oscillator ($g_{14} = g_{41}$ and $g_{24} = g_{42}$). Correspondingly, the total CD of a hybrid chiral nanostructure can be evaluated as:

$$CD = \frac{1}{2}\gamma\omega^2 \sum_i \Delta|u_i|^2, i = 1, 2, 3, 4 \quad (Eq.\ 3.13)$$

To solve the equations, coupling parameters, g_{ij}need to be determined based on the structural configurations. To compare with three-coupled oscillator model in Figure 3.1 and simplify computation, we set the orientations of four oscillators as $\widehat{\boldsymbol{u_3}} = \hat{\boldsymbol{x}}$ and $\widehat{\boldsymbol{u_4}} = \hat{\boldsymbol{y}}$ for plasmonic oscillators and $\widehat{\boldsymbol{u_1}} = \hat{\boldsymbol{x}}$ and $\widehat{\boldsymbol{u_2}} = \hat{\boldsymbol{y}}$ for chiral oscillator, but the result-in underlying physics is general. We will further assume no self-coupling between two plasmonic oscillators, i.e. $g_{34} = g_{43} = 0$. This can often be justified for anisotropic plasmonic nanostructures. For example, the transverse and longitudinal LSPR modes of a metallic plasmonic nanorod are determined independently by its diameter and length, respectively. We considered the relative intensity of optical responses from different portion, and adopt $\frac{N_3}{N_c} = 100$ and $\frac{N_4}{N_c} = 30$ for computation in current work. This allows for comparison with subsequent FEM simulation of specific hybrid nanostructures in Section 3.3.

For the sake of validation and comparison with three-coupled oscillator model, we will initially employ the four-coupled oscillator model to assess a specific scenario involving one-dimensional plasmonic-chiral coupling along *x* axis, denoted as $\hat{\boldsymbol{r}} = \hat{\boldsymbol{x}}$. We can write coupling parameters as:

$$\begin{cases} g_{13} = -e^2[3(\widehat{\boldsymbol{u_3}} \cdot \widehat{\boldsymbol{r_{13}}})(\widehat{\boldsymbol{u_1}} \cdot \widehat{\boldsymbol{r_{13}}}) - \widehat{\boldsymbol{u_1}} \cdot \widehat{\boldsymbol{u_3}}]\dfrac{1}{{r_{13}}^3} = -\dfrac{2e^2}{{r_{13}}^3} \\ g_{24} = -e^2[3(\widehat{\boldsymbol{u_2}} \cdot \widehat{\boldsymbol{r_{24}}})(\widehat{\boldsymbol{u_4}} \cdot \widehat{\boldsymbol{r_{24}}}) - \widehat{\boldsymbol{u_2}} \cdot \widehat{\boldsymbol{u_4}}]\dfrac{1}{{r_{24}}^3} = \dfrac{e^2}{{r_{24}}^3} \\ g_{14} = g_{23} = 0 \end{cases} \quad \text{(Eq. 3.14)}$$

where the r_{13} and r_{24} represent the effective distance between the chiral oscillator and two plasmonic oscillators. In this setup, we designate the ω_4 of the fourth oscillator to have its corresponding LSPR wavelength at 370 nm, while ω_3 of the third oscillator is subject to variation. All other computation parameters remain consistent with those outlined for the three-coupled oscillator model discussed in Figure 3.3. The resultant CD, as predicted by the four-coupled oscillators for this scenario is presented in Figure 3.10. A comparison with the outcomes from the three-coupled oscillator model in Figure 3.3 reveals a similar trend across weak, medium and strong coupling regimes. This conclusion is expected, as the three-coupled oscillator model is developed for one-dimensional coupling and adequately captures its nuances. Nevertheless, this comparison serves as a validation of the consistence of oscillator model framework.

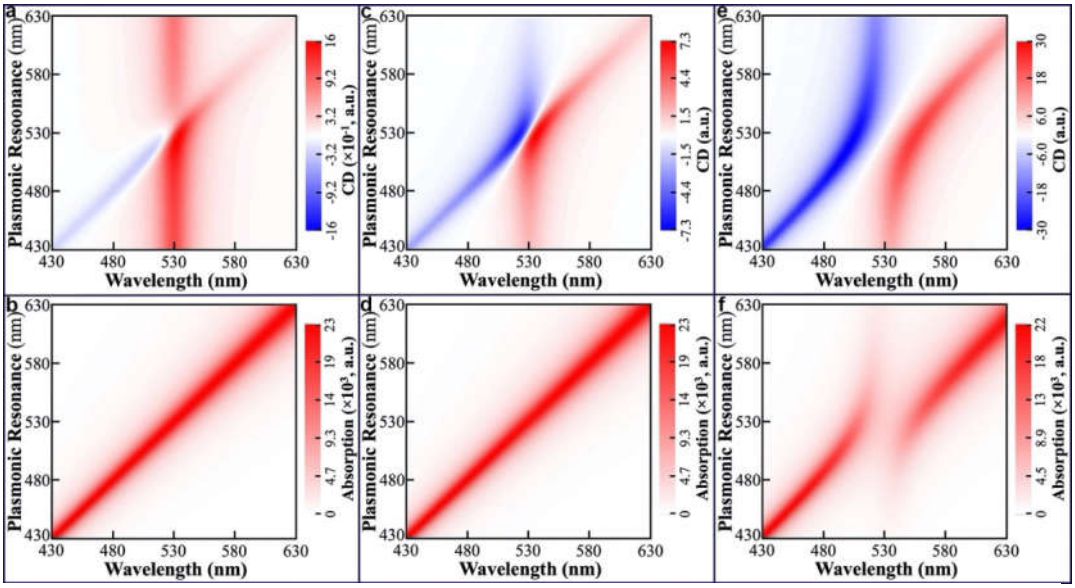

Figure 3.10. Application of the four-coupled oscillator model to scenarios with one-dimensional plasmonic-chiral coupling. (**a**, **b**) representative CD and absorption in a weak coupling regime ($g_{13} = -3 \times 10^{26}\ s^{-2}$; $g_{24} = 1.5 \times 10^{26}\ s^{-2}$) ; (**c**, **d**) representative CD and absorption in a medium coupling regime ($g_{13} = -3 \times 10^{27}\ s^{-2}$; $g_{24} = 1.5 \times 10^{27}\ s^{-2}$) ; (**e**, **f**) representative CD and absorption in a strong coupling regime ($g_{13} = -3 \times 10^{28}\ s^{-2}$; $g_{24} = 1.5 \times 10^{28}\ s^{-2}$); All results are consistent with predictions from the three-coupled oscillator mode in Figure 3.3. The magnitudes of CD and absorption are normalized to the corresponding peak intensities of the uncoupled chiral subunit in Figure 3.2.

Furthermore, we have employed the four-coupled oscillator model to evaluate an anisotropic scenario in which there exist a sizable coupling between the fourth oscillator and chiral oscillator along $\hat{\boldsymbol{r}} = \hat{\boldsymbol{y}}$. In this situation, the three-coupled oscillators model is not sufficient. We thus have:

$$\begin{cases} g_{13} = -e^2[3(\widehat{\boldsymbol{u_3}} \cdot \widehat{\boldsymbol{r_{13}}})(\widehat{\boldsymbol{u_1}} \cdot \widehat{\boldsymbol{r_{13}}}) - \widehat{\boldsymbol{u_1}} \cdot \widehat{\boldsymbol{u_3}}]\dfrac{1}{{r_{13}}^3} = \dfrac{e^2}{{r_{13}}^3} \\ g_{24} = -e^2[3(\widehat{\boldsymbol{u_2}} \cdot \widehat{\boldsymbol{r_{24}}})(\widehat{\boldsymbol{u_4}} \cdot \widehat{\boldsymbol{r_{24}}}) - \widehat{\boldsymbol{u_2}} \cdot \widehat{\boldsymbol{u_4}}]\dfrac{1}{{r_{24}}^3} = -\dfrac{2e^2}{{r_{24}}^3} \\ g_{14} = g_{23} = 0 \end{cases} \quad \text{(Eq. 3.15)}$$

All other computation parameters remain consistent with aforementioned scenario, and the computed CD is summarized in Figure 3.11 for a medium coupling strength. It is

evident that the evolution of CD spectra with the LSPR of the third plasmonic oscillator (Figure 3.3c) is distinctly different from Figure 3.11. This discrepancy can be qualitatively attributed to the anisotropic plasmonic-chiral coupling, underscoring the necessity of the four-coupled oscillator model for this scenario.

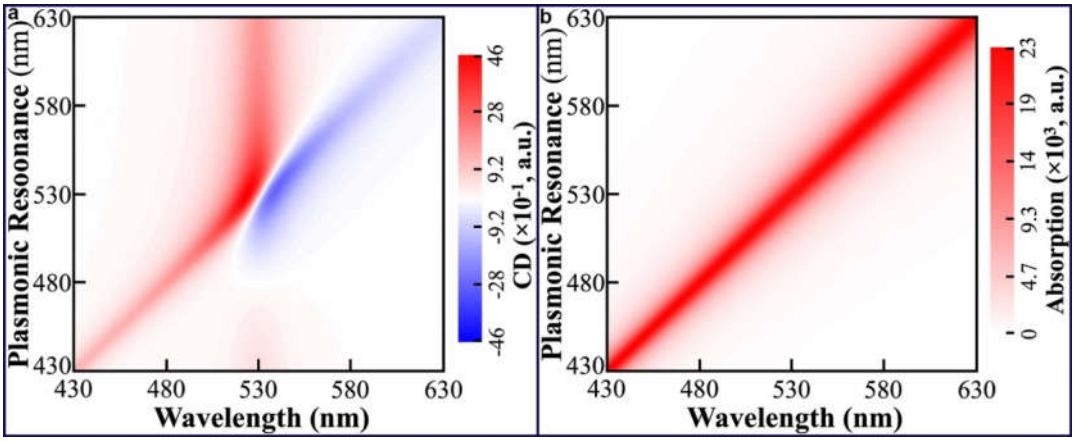

Figure 3.11. Application of the four-coupled oscillator model to a scenario with two-dimensional anisotropic plasmonic-chiral coupling along $\boldsymbol{x}$ and $\boldsymbol{y}$ direction and medium coupling strength ($g_{13} = 1.5 \times 10^{27}\ s^{-2}$; $g_{24} = -3 \times 10^{27}\ s^{-2}$). (**a**) CD and (**b**) absorption maps when the LSPR is tuned across CD peak of chiral oscillator. The magnitudes of CD and absorption are normalized to the corresponding peak intensities of the uncoupled chiral subunit in Figure 3.2.

3.3 Numerical simulation

3.3.1 Methods

We would like to highlight that the theoretical framework of oscillator model in section 3.2 is general and intrinsic without contingent on specific geometry of hybrid nanostructure, and the coupling strength and direction are the only consideration factors in determining underlying coupling physics. Therefore, our understanding and results from the oscillator model can offer a valuable design guideline for materials and structural configuration of hybrid chiral nanostructures with desirable chiroptical response. To evaluate optical response of specific hybrid nanostructures, we have constructed the model and performed the FEM simulation with COMSOL Multiphysics 6.0 software.

We have employed a similar simulation setup and procedure consistent with prior literatures[8,67]. Briefly, a hybrid nanostructure with specific structural configuration and compositions is embedded in an achiral environment, which is set to be vacuum for the current work. To compute specific hybrid chiral nanostructures and compare them with the theoretical oscillator model, we utilize parameters as outlined in Figure 3.12 for the chiral subunits in all structures that can possess a CD peak at 530 nm. These parameters are chosen to resemble chiral materials such as HgS and perovskites, which have been successfully synthesized experimentally. The dielectric function of Ag is acquired from previous literatures[105,106].

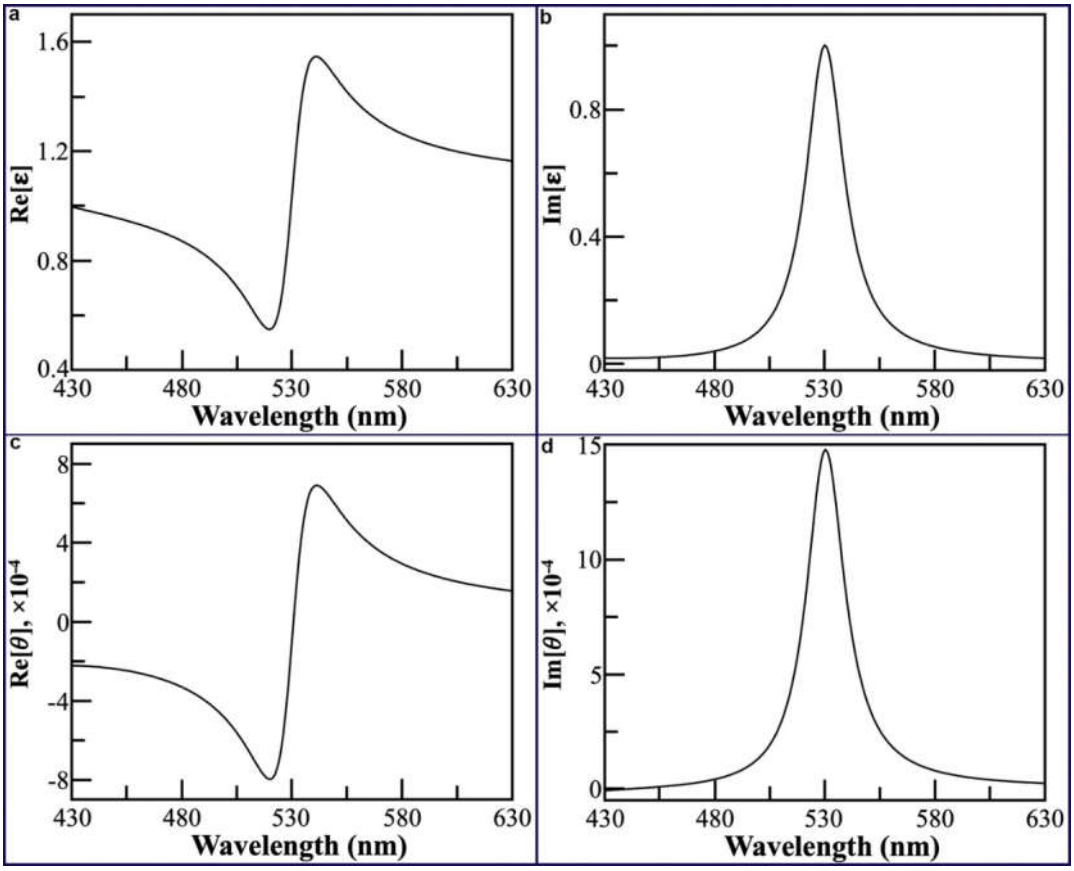

Figure 3.12. Dielectric function and chiral parameters of chiral semiconductor subunit utilized for FEM simulation. (**a**, **b**) real and imaginary portion of dielectric function, respectively. (**c**, **d**) real and imaginary portion of chiral parameter,

We would like to delve further into the critical considerations necessary when employing FEM simulations for computing and analyzing small CD signals. For FEM simulations, the numerical error typically remains several orders of magnitude smaller than the cross section. In most cases, this numerical error is neglectable. However, the CD signal, which represents the difference in cross-section under left and right circularly polarized light, is much smaller than the cross section itself. In the current study, the CD signal ranges from 10^{-4} to 10^{-6} of the cross-section magnitude. Therefore, it is crucial to further minimize numerical errors to accurately represent the CD signal. We have employed symmetric mesh to reduce the numerical error for all the simulated hybrid structures. Additionally, we have devised a method to separate the true CD signal from the numerical errors using chiral media theory. In our model, we treat the chiral subunit as isotropic non-magnetic chiral media, described by constitutive equations in terms of dielectric function (ε), relative permeability (μ), and chirality parameter (θ), all of which are wavelength dependent:

$$\begin{cases} \boldsymbol{D} = \varepsilon \boldsymbol{E} + \dfrac{i\theta \boldsymbol{B}}{c} \\ \boldsymbol{H} = \mu^{-1}\left(\boldsymbol{B} + \dfrac{i\theta \boldsymbol{E}}{c}\right) \end{cases} \qquad (Eq.3.16)$$

where c is the light speed. θ quantifies the chiral asymmetric media. If θ=0 is set for all wavelength, it provides the constitutive equations for achiral media. The terms of $\varepsilon \boldsymbol{E}$ and $\mu^{-1}\boldsymbol{B}$ represent achiral components, while the terms of $\frac{i\theta \boldsymbol{B}}{c}$ and $\frac{i\mu^{-1}\theta \boldsymbol{E}}{c}$ represent chiral components in the equations. The chiral term is typically much smaller compared to the achiral term. To facilitate analysis, we introduce the chirality scale parameter (χ), with θ expressed as $\theta = \chi\theta_0$, where $\chi = 1$ represents the right scale and θ_0 is the chirality parameter which is wavelength dependent. By tuning χ, we can manipulate θ proportionally. Consequently, the $\vec{D}$ and $\vec{H}$ can be expressed as functions of χ: $\boldsymbol{D} = \boldsymbol{D}(\chi)$ and $\boldsymbol{H} = \boldsymbol{H}(\chi)$. As the cross section (σ) is determined by integrating $\boldsymbol{D}$ and $\boldsymbol{H}$, we can express σ as $\sigma = \sigma(\chi)$. Performing a Taylor expansion on $\sigma(\chi)$, we obtain $\sigma(\chi) = a_0 + a_1\chi + O(\chi^2)$, where a_0 and a_1 are the Taylor coefficients for zero- and first- order χ terms, respectively, and $O(\chi^2)$ represents the sum of higher order χ terms. The CD signal can be expressed based on the difference in cross-section

under left and right circularly polarized light ('+' under the excitation of left circularly polarized light and '−' under right circularly polarized light):

$$CD(\chi) = \sigma_+(\chi) - \sigma_-(\chi) = a_{0,+} - a_{0,-} + (a_{1,+} - a_{1,-})\chi + O(\chi^2) \qquad (Eq.3.17)$$

During simulation, each term is subject to numerical errors. For example, we write numerical error of $a_{0,+}$ and $a_{1,-}$ as $Er(a_{0,+})$ and $Er(a_{1,-})$. The calculated CD from simulation can be written as:

$$CD(\chi) = (a_{0,+} - a_{0,-}) + Er(a_{0,+}) - Er(a_{0,-}) + [(a_{1,+} - a_{1,-}) + Er(a_{1,+}) - Er(a_{1,-})]\chi + O(\chi^2) \quad (Eq.3.18)$$

By letting $\chi = 0$, theoretically $CD(0)$ should be equal to 0, implying $a_{0,+} - a_{0,-} = 0$. Therefore, we have $CD(0) = Er(a_{0,+}) - Er(a_{0,-})$, and the $CD(0)$ is equal to the zero-order numerical error. By subtracting $CD(0)$ from $CD(\chi)$, we obtain the zero-order numerical error corrected $CD_{corrected}$ as follows:

$$CD_{corrected}(\chi) = CD(\chi) - CD(0) = [(a_{1,+} - a_{1,-}) + Er(a_{1,+}) - Er(a_{1,-})]\chi + O(\chi^2) \quad (Eq.3.19)$$

In our cases, the first-order numerical error and higher order terms can be neglected. Figure 3.13 provides a typical analysis of our simulation results by using the example of Ag nanorod and chiral medium sphere. We have conducted simulations of the hybrid chiral nanostructure by setting the length of nanorod to be 86 nm and varying the chirality scale parameter χ. As observed in Figure 3.13, the $\frac{CD_{corrected}(20)}{20}$, $\frac{CD_{corrected}(10)}{10}$, $\frac{CD_{corrected}(5)}{5}$ and $CD_{corrected}(1)$ almost overlap, indicating that the computed CD signal after subtracting the zero-order numerical error follows a linear dependence on χ. This error checking further validates our simulation results.

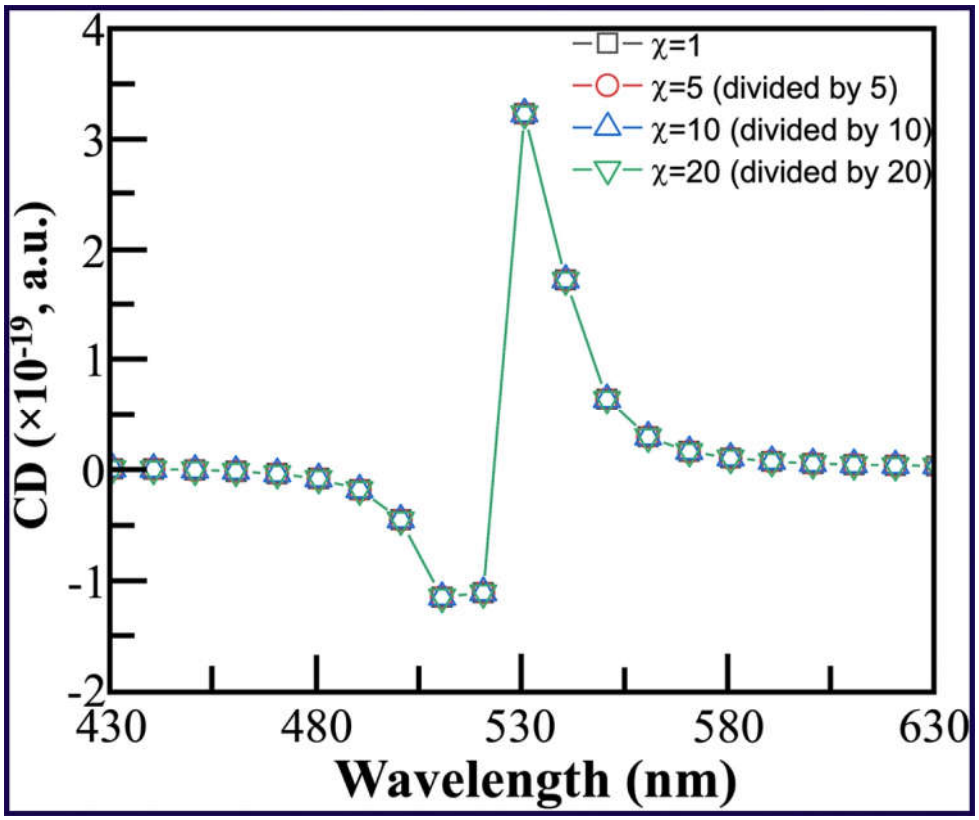

Figure 3.13. The computed CD of hybrid nanostructure of Ag nanorod and chiral medium sphere with different chiral scale parameter χ. The length of nanorod subunit is fixed to be 86 nm. Zro-order numerical error is subtracted. For the case of $\chi = 5, 10$ and 20, the computed CD are divided by 5, 10 and 20, respectively. It can be seen that the $\frac{CD_{corrected}(20)}{20}$, $\frac{CD_{corrected}(10)}{10}$, $\frac{CD_{corrected}(5)}{5}$ and $CD_{corrected}(1)$ curves agree very well in our simulation setting.

3.3.2 Achiral Ag nanrod and a chiral semiconductor nanoparticle

To facilitate a direct comparison with theoretical predictions summarized in Figure 3.3, we have chosen a chiral semiconductor subunit for FEM computation that can possess a CD peak around 530 nm with materials parameters summarized in Figure 3.12, resembling a few nanoscale chiral semiconductors that have been achieved experimentally, including chiral cinnabar HgS and perovskites[8,107-109]. We have first evaluated a chiral hybrid nanostructure consisting of an achiral plasmonic Ag

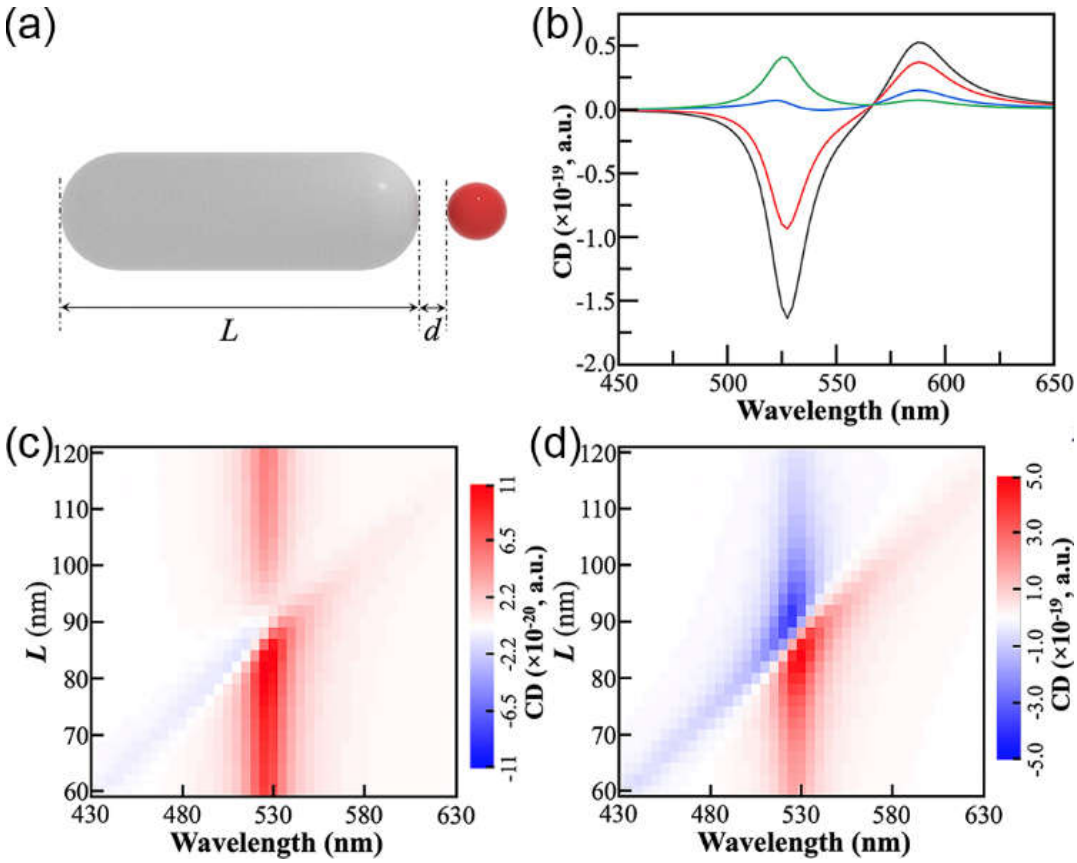

Figure 3.14. A hybrid chiral nanostructure comprising a Ag nanorod (grey) with a diameter of 30 nm and a length of *L*, along with a spherical chiral semiconductor (red) with a diameter of 10 nm, positioned at the end of the nanorod at a distance of *d*. (a) Schematic representation of structural configuration. (b) Computed CD spectra at different *d*: 1 nm (black), 5 nm (red), 20 nm (blue), and 40 nm (green). (c) Variation of CD with *L* at the fixed *d*= 40 nm. (d) Variation of CD with *L* at the fixed *d*= 1 nm.

nanorod and a chiral semiconductor nanoparticle located at the end of nanorod with structural configuration shown in Figure 3.14a. We have chosen Ag nanorods based on considerations that it can have both longitudinal and transverse LSPR modes and the wavelength of its longitudinal mode can be tuned by simply varying its length (Figure 3.15)[73]. Figure 3.14b compares different CD spectra at different gap distance *d*, while maintaining the length of Ag nanorod as 104 nm (corresponding to the longitudinal LSPR peak at 590 nm). Two features can be immediately identified from

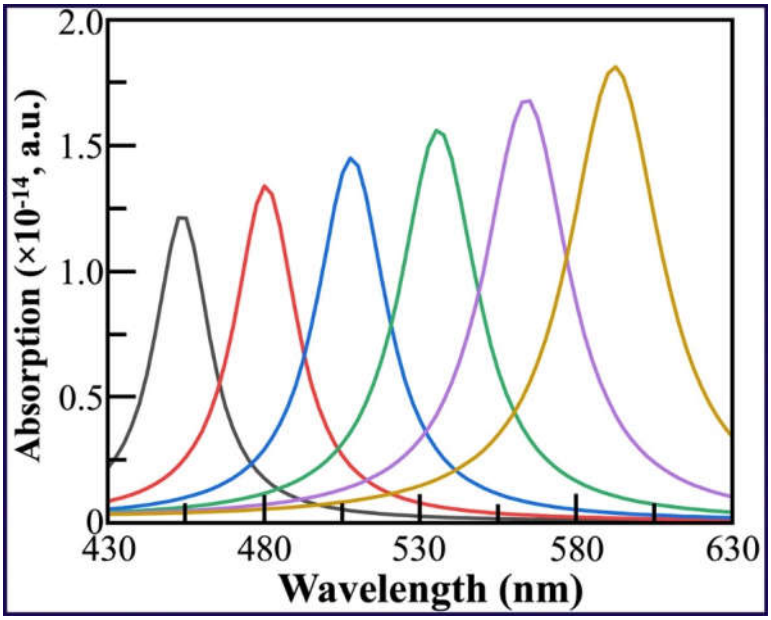

Figure 3.15. Tunable longitudinal LSPR wavelength by length of Ag nanorods. The spectra are computed by FEM simulation for Ag nanorods with fixed diameter of 30 nm but varying length *L*: Black, 66 nm; Red, 74 nm; Blue, 82 nm; Green, 90 nm; Purple, 98 nm; Dark Yellow, 106 nm.

Figure 3.14b: First, a new positive CD peak appears at 590 nm, and the central wavelength remains unchanged when *d* is varied but its magnitude increases as *d* decreases. Second, the sign of original CD peak of chiral nanoparticle changes from positive to negative when the *d* becomes smaller. The appearance of new CD peak that is consistent with peak wavelength of longitudinal LSPR of Ag nanorods suggests that it is an induced plasmonic CD and is caused by its neighboring chiral nanoparticle. As a result, when the *d* is reduced, near-field coupling between Ag nanorods and chiral nanoparticle is enhanced, leading to larger induced CD signal. Furthermore, observation of sign inversion of CD peak at 530 nm agrees with prediction in Figure 3.4 by our three-coupled oscillator model: when the d is varied from large to small, the coupling strength between Ag nanorod and chiral nanoparticle is tuned accordingly from weak to medium coupling, leading to a sign

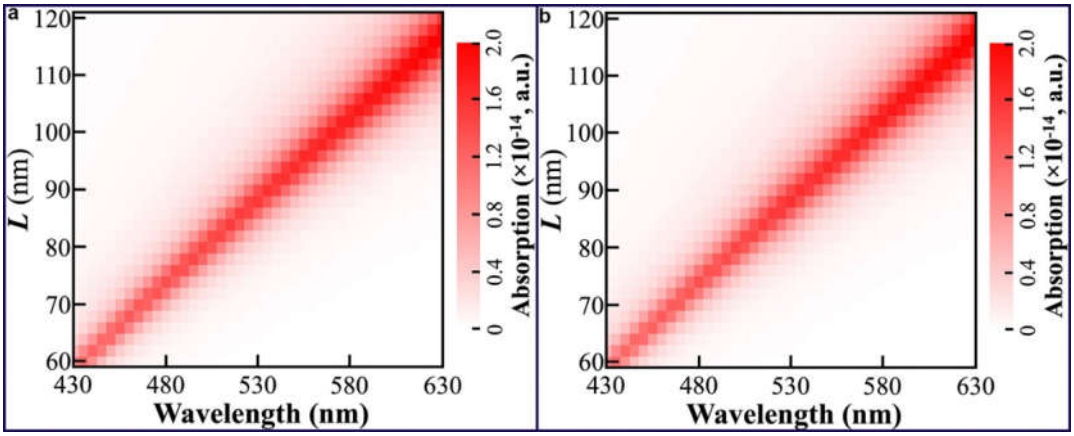

Figure 3.16. Evolution of absorption of hybrid nanostructure in Figure 3.14 with length of Ag nanorods at the different gap distance. (**a**) *d*= 40 nm. (**b**) *d*= 1 nm.

change of CD of chiral subunit. Moreover, we have investigated the evolution of CD with the length of Ag nanorod in the hybrid nanostructure at two gap distances of 40 nm (weak coupling) and 1 nm (medium coupling), as shown in Figures 3.14c and 3.14d, respectively. Corresponding variation in the absorption spectra are provided in Figure 3.16. Figures 3.14c and 3.14d show distinct dependence of CD on L, however, both scenarios show excellent agreement with Figures 3.3a and 3.3c for the weak and medium coupling regimes, respectively. Figure 3.17 provides CD and absorption maps at two more distances (5 nm and 20 nm), which shows how the CD sign inversion evolves and the transition from weak to medium coupling regimes occurs around 20nm distance. This control simulation substantiates the CD mechanism discussed in Figure 3.5, in which the total CD is determined by the competition of two different types of chiral coupling processes.

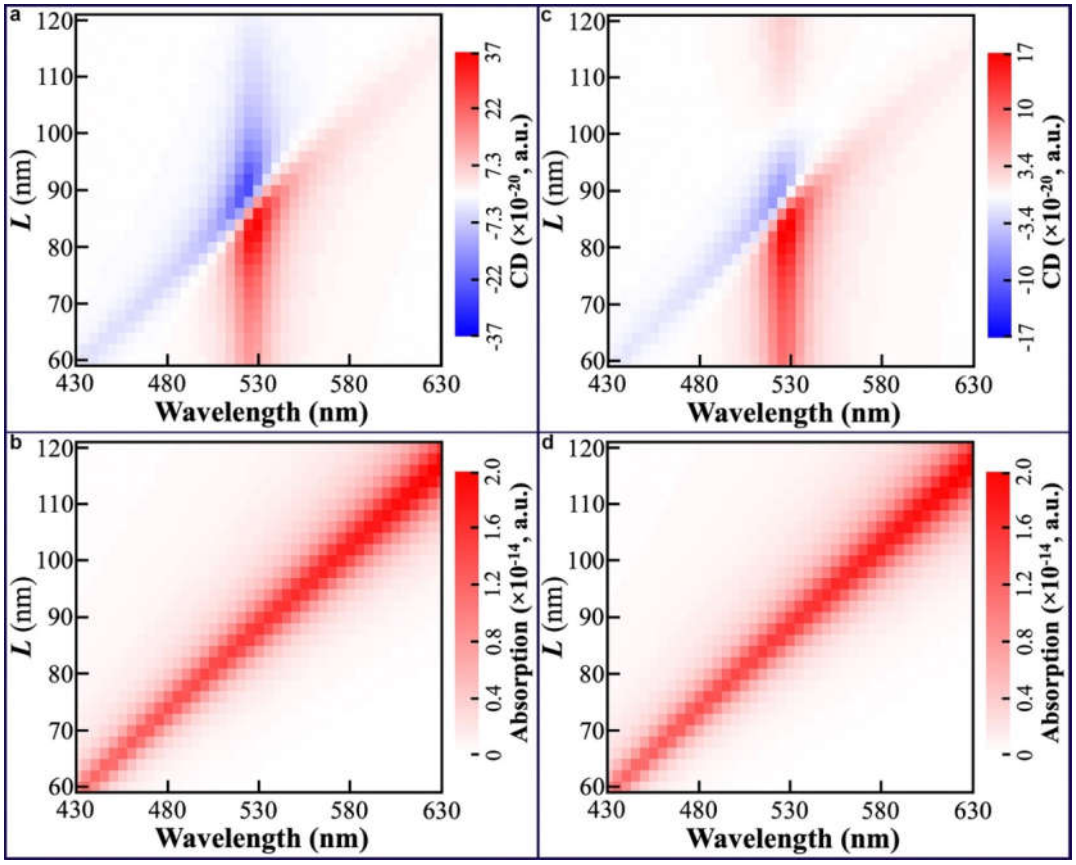

Figure 3.17. Evolution of CD and absorption of hybrid nanostructure in Figure 3.14 with *L* at different gap distance. (**a**, **b**) CD and absorption mapping for *d*= 5 nm, respectively. (**c**, **d**) CD and absorption mapping for *d*= 20 nm, respectively.

It is noteworthy that in the depicted configuration where the chiral semiconductor nanoparticle is positioned at the end of the nanorod, as illustrated in Figure 3.14a, the coupling between the plasmonic and chiral subunits is primarily governed by the longitudinal LSPR mode. Consequently, our three-coupled oscillator model adequately address the underlying chiral physics in this scenario, notwithstanding the anisotropic nature of the Ag nanorod. Importantly, we have also evaluated another hybrid chiral nanostructure by placing the chiral semiconductor subunit in the middle of achiral plasmonic nanorod subunit but with close distance (Figure 3.18). In this

structural geometry, two- dimensional anisotropic couplings from both the longitudinal and transverse modes need to be considered. We have computed its optical response with results presented in Figure 3.18 and found that although absorption feature of this new hybrid chiral nanostructure is still dominated by the plasmonic subunit, its CD characteristics is completely different from Figure 3.14c, and cannot be interpreted by the three-coupled oscillator model due to the fact that higher dimensional anisotropic coupling in this configuration cannot be negligible. Nevertheless, our four coupled oscillator model can precisely predict anisotropic features uncovered by FEM simulation and shows excellent agreement (Figure 3.11), further validating our oscillator model and highlighting its versatility, scalability and effectiveness to elucidate intricate underlying coupling physics inherent in various hybrid chiral nanostructures.

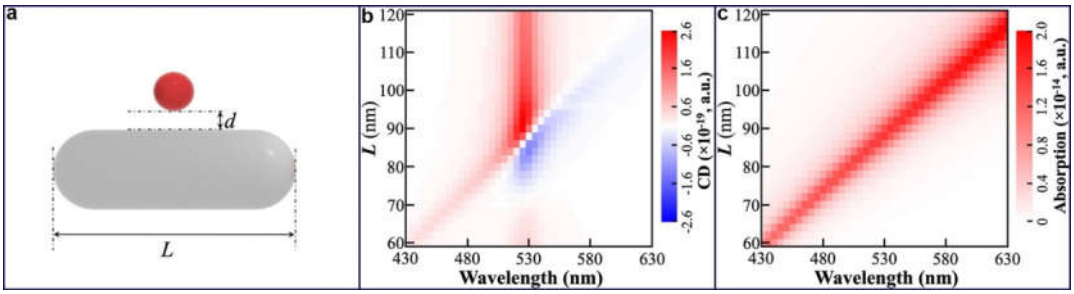

Figure 3.18. Hybrid chiral nanostructure featuring a plasmonic Ag nanorod coupled with a chiral semiconductor nanoparticle positioned in the middle of the nanorod with a close distance. (**a**) Schematic representation of the structural configuration. (**b**) Evolution of CD spectra with varying lengths of nanorods. (**c**) Evolution of absorption spectra with varying lengths of nanorods. The simulations are conducted with *d* of 1 nm and a chiral nanoparticle diameter of 10 nm, while the length *L* is adjusted.

3.3.3 Achiral Ag bowtie and a chiral semiconductor nanoplate

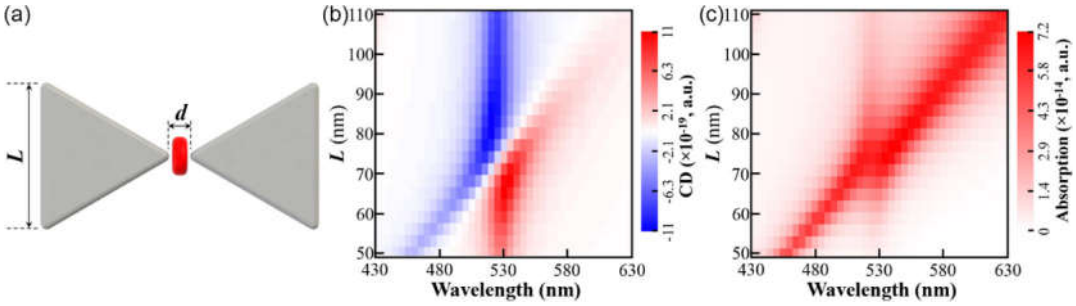

Figure 3.19. Hybrid chiral nanostructure composed of a plasmonic Ag bowtie subunit (whose thickness is 20 nm with side length of *L* and a gap distance of *d*) and a chiral semiconductor nanoplate subunit (whose diameter and thickness is 20 nm and 8 nm, respectively) at the center. (a) Schematic representation of structural configuration. (b) and (c), Evolution of CD and absorption spectra with *L*, respectively, while *d* is fixed at 10 nm.

Additionally, we have investigated another type of hybrid chiral nanostructure consisting of an achiral plasmonic bowtie subunit with a chiral semiconductor nanoplates in the center, showcasing one-dimensional plasmonic-chiral coupling (Figure 3.19a). By tuning the dimensions of the bowtie plasmonic subunit, the peak wavelength of LSPR at the center of structure can be tuned, and a significant enhancement (hotspot) of electromagnetic field in the regime confined by the two apexes of the bowtie subunit can be achieved at the small *d* (Figure 3.20). The

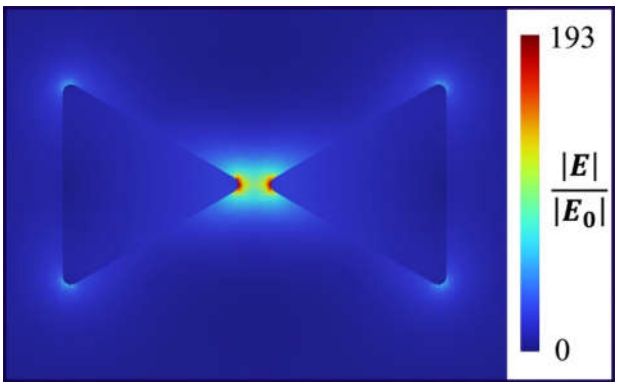

Figure 3.20. Normalized electric field enhancement at the resonances in plasmonic Ag bowtie subunit in Figure 3.19 with *d* of 10 nm. The color scale bars show the normalized electric field amplitude relative to the incident field E_0.

resonance wavelength tunability as well as strong ability of the bowtie subunit to enhance the local electromagnetic field amplitude is promising to enable strong inherent coupling strength with chiral subunit in a hybrid nanostructure. The resulting CD (Figure 3.19b) and absorption (Figure 3.19c) clearly exhibit existence of a mode splitting feature around the CD peak of chiral subunit, and two split band with opposite CD emerges, which are accurately captured by our three-coupled oscillator models.

3.4 Conclusion

In summary, we have developed a theoretical coupled oscillator model to describe and elucidate the underlying chiral coupling physics of a novel hybrid chiral nanostructures, which consists of an achiral plasmonic subunit and a chiral semiconductor subunit. This emergent hybrid chiral nanostructure can serve as an important testbed for exploring fundamental plasmonic-chiral coupling and various new chiroptical phenomena. Three different coupling regimes (weak, medium and strong) with manifestation of distinct CD characteristics have been predicted, depending solely on the intrinsic coupling strength. Additionally, our model elucidates the underlying mechanisms behind these different coupling regimes, shedding light on the competition among various coupling processes defined by the hybrid chiral nanostructures. Notably, our oscillator model is generalizable and not constrained by specific structural configurations, making it applicable to a wide range of hybrid systems that can be achieved by the bottom-up or top-down techniques. Although we have mainly employed the simplest three-coupled oscillator model as an example to apply for a hybrid chiral nanostructure possessing a

one-dimensional plasmonic-chiral coupling scenario, the concept of coupled oscillators can be further extended to incorporate more oscillators to address more complex coupling scenarios, including higher dimensional anisotropic plasmonic-chiral coupling. To that, a four-coupled oscillator model is also presented in the current work, highlighting the scalability and generality of proposed model. Through validation using FEM simulations of a few concrete hybrid nanostructures, we have further demonstrated excellent agreement between coupled oscillator model predictions (from both three and four- coupled oscillators) and numerical simulations, further substantiating the validity and reliability of our coupled oscillator model. All these together has suggested that a simple coupled oscillator model can provide a robust framework for further exploration of intricate chiral coupling processes inherent in the emergent hybrid chiral nanostructures with deep insights, and also offer a rational materials design guideline for the future advancement of hybrid chiral nanostructures with desirable chiroptical properties and enhanced functionalities for broad applications. Last but not the least, by extending our coupled oscillator model with generalized parameters and high-order coupling terms that are recently developed in literatures[96,110], we expect to gain deeper understanding of non-linear optical response like higher- harmonic CD that might be enabled in a sophistically designed hybrid chiral nanostructure with inherent plasmonic-chiral coupling. Moreover, the validation of our oscillator model using FEM simulations sets the stage for experimental verification of theoretical predictions, through the fabrication and characterization of actual hybrid chiral nanostructures, which will be essential for advancing our understanding and harnessing the potential of these structures for practical applications

in fields such as plasmonic chiral switch, plasmon-enhanced chiral sensing and chiral photon emitters[18,111,112]. With the increasing interest in chiral nanophotonics and the ongoing developments in nanofabrication techniques[113,114], our coupled oscillator model presents a powerful tool for advancing both fundamental understanding and practical applications in this burgeoning field.

Chapter 4: Nanoscale characterization of chiral gold nanoparticles with optical atomic force microscopy

4.1 Introduction

Recent years have witnessed rising studies in nanoscale chirality in the realm of inorganic materials due to their profound physics as well as intriguing application across chemistry to spintronics.[1-4,27-42] As discussed in previous chapters, there have been great efforts and advancements in introducing chirality into inorganic nanostructure as well as the theoretical models and numerical simulations to explain the underlying mechanism. Meanwhile, the characterization techniques for microscopic chirality are still nascent. Most chiroptical characterization has been limited to ensemble measurement (Figure 4.1) because of the historical reasons and the difficulty to access the subwavelength resolution due to diffraction limit. Lacking spatial resolution leads to an unpleasant gap between the experimental observation and numerical/theoretical understanding. For example, there is inevitable inhomogeneity among the chemically synthesized nanoparticles concerning the geometry and optical properties, which require individual characterization. Furthermore, the spatial dependent features in plasmonic nanostructures predicted by theoretical and numerical studies are vital for a deep understanding of chiral mechanism as well as the applications for enantiocatalysis[62,78], polarization light control[96,115,116] and etc. However, all of these are unfortunately out of scope in ensemble measurements.

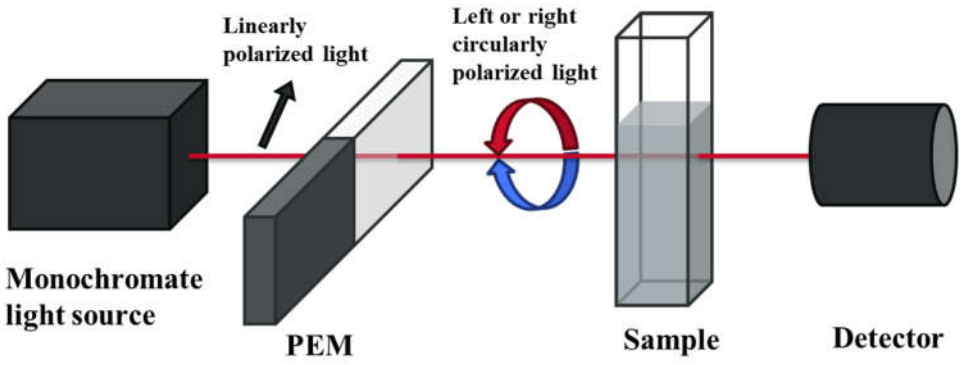

Figure 4.1. The schematic of a commercial CD machine for ensemble measurement.

Because of diffraction limit it's difficult for far field measurement to characterize the local chiroptical response as it's usually within sub-wavelength range. Researchers have made a few attempts on a single particle level measurement on chiral nanoparticles with different methods. For example, researchers performed single-particle circular differential scattering spectroscopy on plasmonic nanoparticle-protein complexes[18,26]. The single-particle circular differential scattering spectroscopy is performed on a dark-field microscope setup. Left and right circularly polarized light and oil immersion condenser are used to create evanescent wave excitation. Scattering signal is collected by objective followed with slit aperture. In such experiment, they are able to detect the single particle level signal of the structural chirality of plasmonic aggregates and plasmon-coupled circular dichroism induced by chiral proteins. With similar principle, single particle extinction/scattering circular dichroism were measured in different samples.[28,117,118] Another technique developed is single particle photothermal dichroism[119,120]. The photothermal effect of the chiral plasmonic particles can lead to an enhanced photoluminescence of electrons in the f orbital of Er^{3+} ions. The photoluminescence signal is collected with a confocal microscope and the relative intensity is used as an indicator of photothermal effect.[119]

By comparison under different circularly polarized excitation, people are able to measure the photothermal dichroism of single particle. In both cases, people have been using confocal microscopy to perform single particle level circular dichroism measurement. However, an obvious drawback is that such measurements are still limited by spatial resolution and cannot provide dichroism mapping on the fine geometry features.

Atomic force microscopy (AFM) was first invented by IBM scientists in 1985. With feedback control on the tip, the movement of tip can record the morphological information of samples down to atomic resolution based on force interaction of tip and sample.[121] AFM has demonstrated application in a wide range of disciplines from biological samples to novel 2D materials. Recent years have witnessed a development of integrating optical microscopy with AFM system which enables characterization of local optical properties with nm level spatial resolution.[122-126] As comparison, far field optical measurements are limited by the diffraction limit and cannot reach the subwavelength resolution. Two major techniques of integration of optical measurement and AFM are photo induced force microscopy (PiFM)[122-124], which is also referred as AFM-IR, and scanning near field optical microscopy (SNOM).[125,126] In SNOM, the near field optical signal is collected as the AFM probe scanning over the sample. Particularly, scattering type SNOM (s-SNOM)[126] collect the tip-sample scattering light under light excitation. The intensity and phase of the scattering light are extracted based on interference technique and could be used to derive the optical property (e.g. dielectric function) of the sample. On the other hand, PiFM detects the photo induced tip-sample force interaction under light excitation by monitoring and

analyzing the small perturbation in the AFM tip movement. The intensity and phase of the photo induced tip-sample force reveal a interplay of local optical and mechanical properties of the sample.[123]

In this Chapter, we developed a new technique of the polarization dependent PiFM measurement. This new technique enables us to characterize the near field chiroptical response of the chiral plasmonic nanoparticles, which is beyond the capabilities of far field chiroptical measurement. We anticipate that such technique would provide exciting opportunities for direct characterization of nanoscale chirality and lay the groundwork for manipulation and application of local chirality.

4.2 Experiment

4.2.1 Optical AFM setup

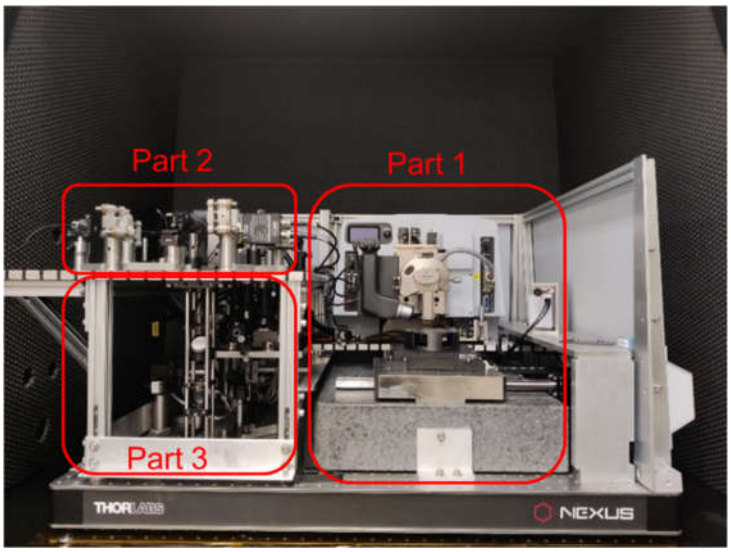

Figure 4.2. The photo of our modified Bruker optical AFM apparatus. Part 1: Bruker AFM system; Part 2: Home-built top excitation optical path and s-SNOM optical path; Part 3: Home-built bottom excitation optical path.

Our experiment is based on a modified commercial Bruker optical AFM apparatus (Figure 4.2). There are a few unique modifications for our polarization dependent

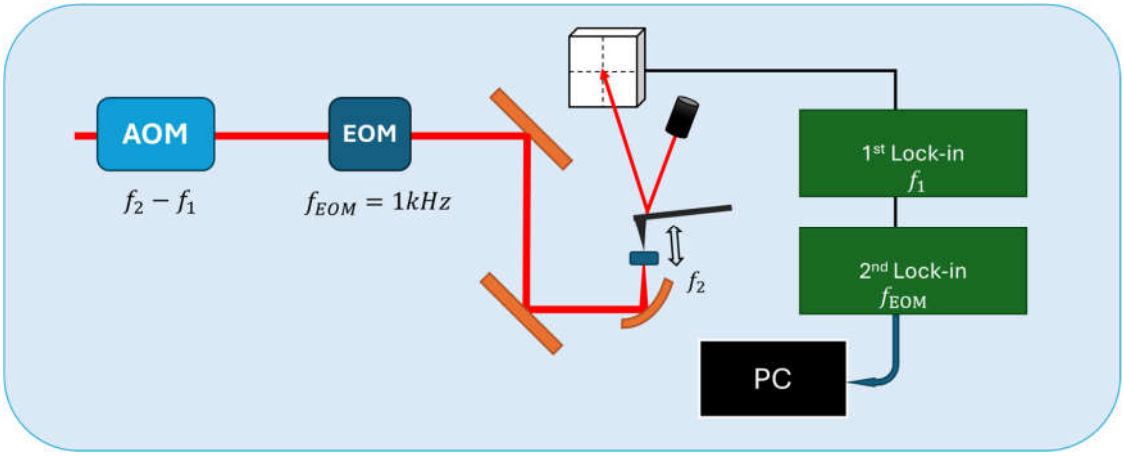

Figure 4.3. Cascading detection scheme of the polarization dependent PiFM measurement. The 638nm diode laser is first amplitude modulated by AOM at $f_2 - f_1$ and then polarization modulated by EOM at $f_{\mathrm{EOM}} = 1k\mathrm{Hz}$ The cantilever deflection signal is firstly demodulated at f_1 and then demodulated at f_{EOM} to get the polarization dependent signal.

optical AFM measurement that can be summarized below. We utilize a cascading detection scheme shown in Figure 4.3 for the polarization dependent PiFM measurement. Typically, the AFM controller drive the cantilever tip at its 2nd intrinsic oscillation mode f_2 and monitor the cantilever movement at 1st intrinsic oscillation mode f_1 as the optical AFM signal. An external 638nm diode laser is used for excitation with the modulation of an acoustic optical modulator at $f_2 - f_1$ to induce the PiFM signal at f_1. An electro-optical modulator (EOM) is used to modulate the polarization of incident laser between left and right circularly polarized light at 1kHz to create the differential PiFM signal. Differently from the commercial setup, we use a bottom excitation optical path rather than the original top excitation optical path (Part 2 in Figure 4.2). In the original top excitation optical path, the excitation laser has a right angle of incidence to the tip and therefore excites both the tip dipole and sample. The interaction of tip dipole and sample can be destructive or constructive coupling depending on the phase relation which causing issue to single out our

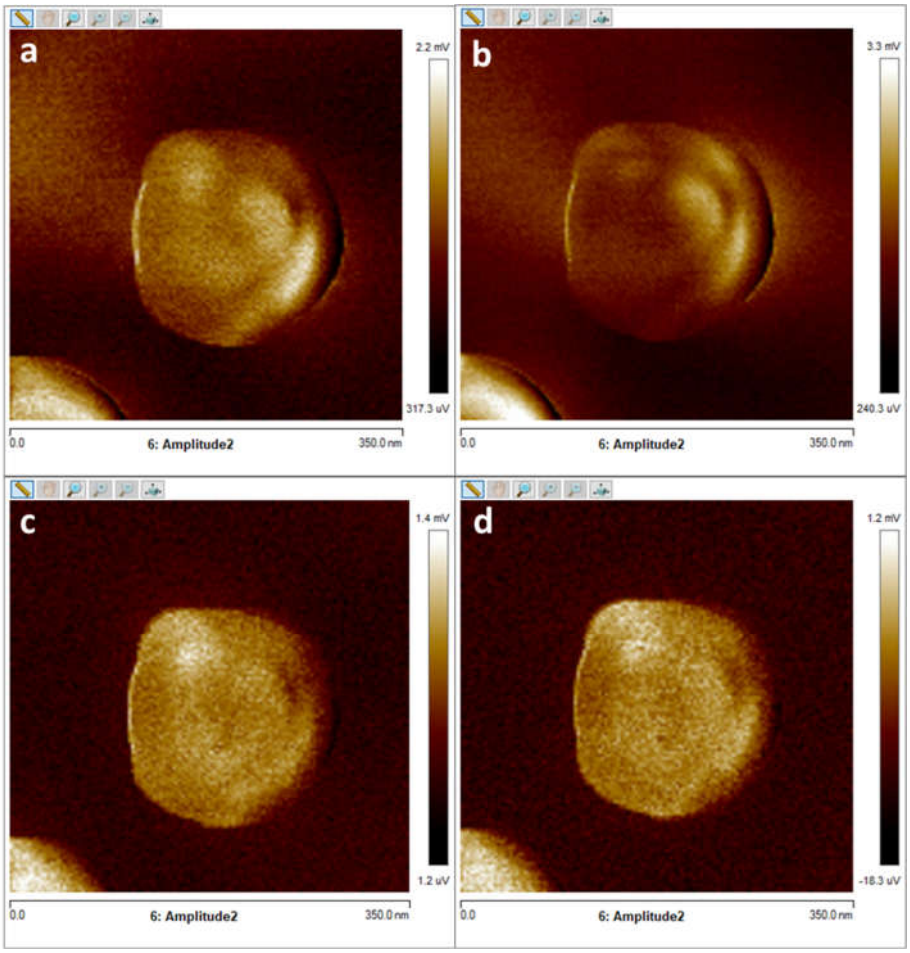

Figure 4.4. PiFM result of the same particle under (a&b) top excitation with (a) LCP and (b) RCP and (c&d) bottom excitation with (c) LCP and (d) RCP. The strong tip-sample coupling in top excitation scheme leads to very different results from top and bottom excitation scheme.

interested signal from the sample itself.[127-129] In the bottom excitation optical path, the electric field of incident laser is perpendicular to the tip dipole avoiding the direct excitation of the tip dipole. Figure 4.4 presents the PiFM results of the same gold nanoparticle from top and bottom excitation, which show a clear difference. For the bottom excitation path in our experimental setup, a fast-steering mirror (FSM) and off-axis parabolic (OAP) mirror are installed with OEM controllers. A new sample stage and OAP holder were designed and 3D printed by UMD Terrapin Works. The old optical table was replaced with the new optical table is machined by the workshop

in Laboratory for Physical Sciences (LPS). A homebuilt LabVIEW program is developed for control and optimization of FSM and OAP.

For the signal collection, the cantilever deflection signal is detected by the quadrant photodiode detector. The 1st lock-in demodulated the signal at f_1 to give the optical AFM signal which is sent to the 2nd lock-in. The 2nd lock-in demodulate the PiFM signal at $f_{\mathrm{EOM}} = 1k\mathrm{Hz}$ to give the polarization differential signal.

4.2.2 Sample preparation and characterizaton

Chiral helicoid Synthesis. The chiral helicoid III for the characterization is synthesized following the previous literature.[14] The 1-2nm gold seed nanoparticles are prepared by the following procedure: 2.5ml 0.2M CTAC, 125ul 10mM $HAuCl_4$, 2.15ml H_2O are mixed, which followed by rapid injection of 0.45ml 10mM ice cold $NaBH_4$ solution with stirring. The solution quickly turns brown. After 2min stirring, the solution is left for 1h incubation at 30°C for next step usage. Prepare two bottles of solutions A and B: for both, mix 5ml 0.2M CTAC, 4.47ml H_2O, 250ul 10mM $HAuCl_4$, 5ul 10mM KI and 220ul 0.1M AA. Firstly, add 55ul 1-2nm gold seed solution into solution A while stirring. After 5s, solution A turns pink, add 55ul solution A into solution B while stirring. After 10s, the solution B is left for incubation for 3 hours. The synthesized gold nanooctahedra are collected by 2 times centrifugation and redispersion into 1ml DI water. For synthesis of chiral helicoid III, mix 0.3ml 0.2M CTAB, 0.2ml 10mM HAuCl4, 4.15ml H_2O, 0.775ml 0.1M AA, 12ul 2.5mM L-GSH, 20ul gold nanooctahedra seed solution. The mixture is left

undisturbed at 30°C for 90mins before 2 times centrifugation and redispersion into 1ml DI water.

Preparation of the PiFM sample. Fused silica substrates are cleaned with piranha solution and DI water first and then immersed in 5mM 3-aminopropyltriethoxysilane (APTES) solution and left for drying. The 3-aminopropyltriethoxysilane molecules are used for immobilization of the chiral helicoids. One drop of the chiral helicoid III solution is added onto the pretreated substrate and left for drying in the air. The extra 3-aminopropyltriethoxysilane molecules are saturated by a quick dipping of the whole fused silica substrate in 1% HCL solution which are followed by washing out by DI water with a few rounds and drying in the air.

Characterizations. For SEM characterization, the samples are prepared using a similar method for preparation of PiFM sample. Tescan XEIA FEG SEM equipped with a field emission gun from Maryland Nanocenter at the University of Maryland was applied. Typical TEM imaging parameters were: 10 keV electron landing energy and, 4 s acquisition time. The circular dichroism (CD) and absorption spectra of solutions samples are simultaneously acquired on a commercial JASCO J-815 spectrometer at room temperature using a cuvette with light path of 1.0 cm.

FEM Simulation. We have performed FEM simulation to evaluate both extinction and CD properties of chiral nanostructures by using a commercial COMSOL Multiphysics 6.0 software. The 3D models of chiral Au helicoid are firstly constructed by using a different commercial 3D modeling software (SOLIDWORKS), and then are imported to the FEM solver (COMSOL). The chiral

Au helicoid model is encapsulated by a spherical shell with size of the maximum excitation wavelength as the achiral environment and its outer surface set as perfect matching layer (PML) boundary. For the simulation of ensemble measurement of CD and absorption, the dielectric function of environment is always set to be that of water in order to simulate the measurement condition (in DI water). Because of the low anisotropy, we only calculate the incident wave in one direction. For the simulation of near field electric field of chiral helicoid in PiFM measurement, a box of fused silica substrate is placed underneath the chiral helicoid and the dielectric function of environment is set to be that of air. The dielectric function of Au is from the literature[106].

4.3 Result and discussion

4.3.1 Ensemble measurement and simulation.

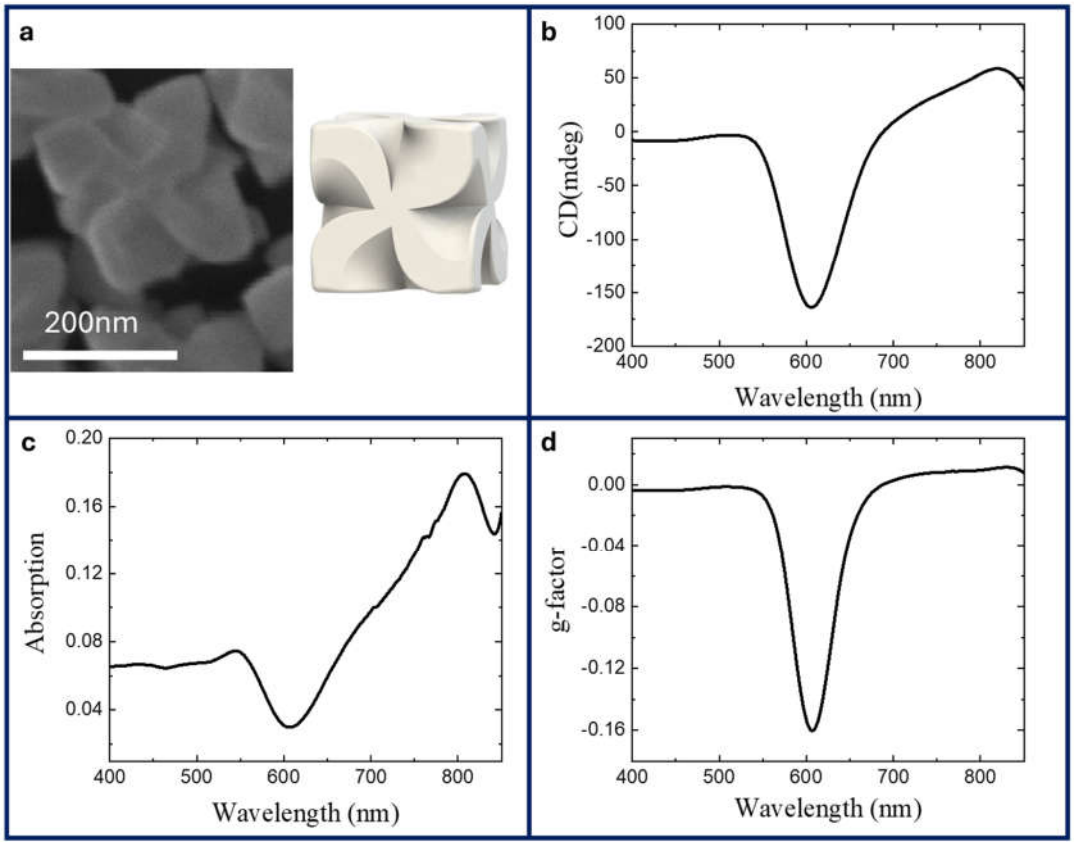

Figure 4.5. Chiral helicoid nanoparticles. (a) SEM image and 3D model of the chiral helicoid nanoparticles. Scale bar: 200nm. (b) CD, (c) absorption and (d) g-factor spectra by the ensemble optical measurement of the chiral helicoid nanoparticles solution.

In Figure 4.5a, SEM characterization of the synthesized chiral helicoid nanoparticles shows a clear chiral geometry and a 3D model of the chiral helicoid created in SolidWorks is also presented to highlight the chiral features. Each face of the chiral helicoid consists of four highly clockwisely curved arms. The side length of the chiral helicoid is about 170nm. Ensemble optical measurements of the chiral helicoid show a strong CD peak at 605nm with a g-factor of -0.16.

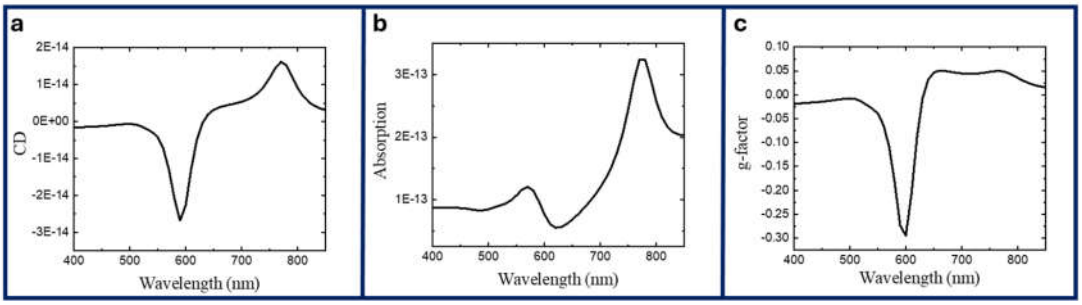

Figure 4.6 The simulated CD and absorption result of the chiral helicoid nanoparticle. (a) CD, (b) absorption and (c) g-factor spectra of the chiral helicoid nanoparticle.

Based on the 3D model in Figure 4.4a, we ran a finite element method simulation of the chiroptical response of the chiral helicoid nanoparticle using COMSOL. The simulation results are presented in Figure 4.6. We can see that the CD and absorption spectra are consistent with the measured spectra. Meanwhile, the simulated g-factor has the maximum amplitude of -0.3 compared to the experiment maximum g-factor of -0.16. This difference can be contributed to the inhomogeneous shape distribution of chiral helicoid nanoparticles in measurements.

4.3.2 Polarization dependent PiFM

The geometric feature of the chiral helicoid nanoparticle is firstly characterized by silicon tip (TESP from Bruker). The silicon tip has a tip radius of about 7nm and therefore is able to resolve the chiral feature of the nanoparticle (See Figure 4.7a). The polarization dependent optical AFM result of the same chiral helicoid nanoparticle is measured with a platinum coated tip (ARROW-NCPt from NanoWorld). The result is shown in Figure 4.7b to 4.7f. The ARROW-NCPt tip has a

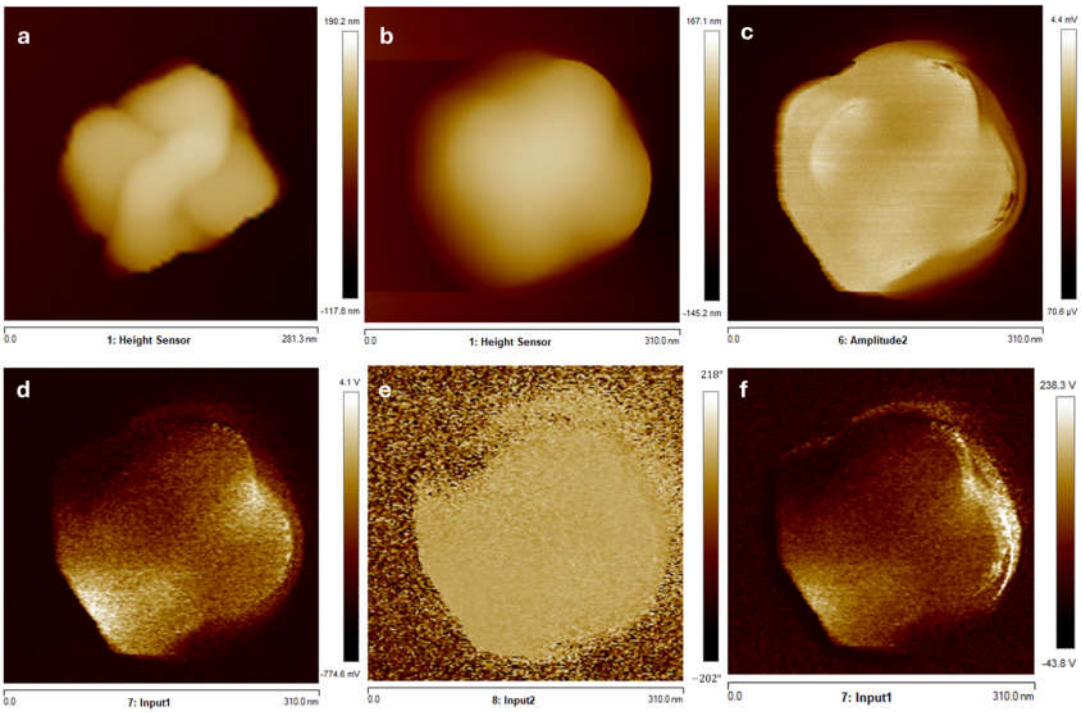

Figure 4.7. Polarization optical AFM measurement of chiral helicoid nanoparticle. (a) the AFM image of the chiral helicoid particle with silicon AFM tip (TESP). (b) the corresponding AFM image of the same nanoparticle with Pt coated tip (ARROW-NCPt). (c) The average optical AFM signal of left and right circularly polarized excitation light. (d,e) The (d) amplitude and (e) phase of the differential optical AFM signal of left and right circularly polarized excitation light. (f) calculated g-factor map calculated based on (c) and (d).

tip radius of about 25nm and therefore cannot resolve the fine geometric feature as shown in Figure 4.7b. We can only barely tell the gaps between the curved arms. As shown in Figure 4.7c, the PiFM signal, however, presents some fine features. The four corners present a brighter contrast. There are some artifacts on the top right and bottom right corners due to the fluctuation of tip oscillation frequencies at the contact of tip and helicoid corners. Figure 4.7d and e present the amplitude and phase of differential signal of the left and right circularly polarized excitation light. The outer edge of the protruding curved arms gives stronger signals. Meanwhile, the whole

helicoid surface presents a constant phase $120°$ showing a constant sign of differential signal over the whole surface. Moreover, we can calculate the g-factor map shown in Figure 4.7f based on the differential PiFM and averaged PiFM signal.

Before further analysis of the data, we firstly review the physical mechanism of the PiFM signal. There are two major processes[122] which contribute to the PiFM signal I:

$$I = I_{PT} + I_{OF}$$

Where I_{PT} describes the PiFM signal from photothermal effect and I_{OF} describes the PiFM signal from optical force effect.

In the physical process of photothermal effect, the absorption of incident laser induces a local heating of sample which leads to a local thermal expansion of sample. The photo induced thermal expansion modifies the tip-sample interaction and thus perturbates the AFM cantilever movement, which is picked up as the cantilever deflection signal. In this mechanism. the acquired PiFM signal should be linear to the thermal expansion coefficient and local temperature. For plasmonic gold nanoparticles, the thermal relaxation and heat transfer within the plasmonic helicoid is in the time scale of a few ns[130]. As a comparison, the excitation laser pulse width in our measurement is hundreds of ns. Therefore, in our current measurement the temperature over the particle can be considered homogeneous. This means that the PiFM signal from photothermal effect should be homogeneous over the whole particle.

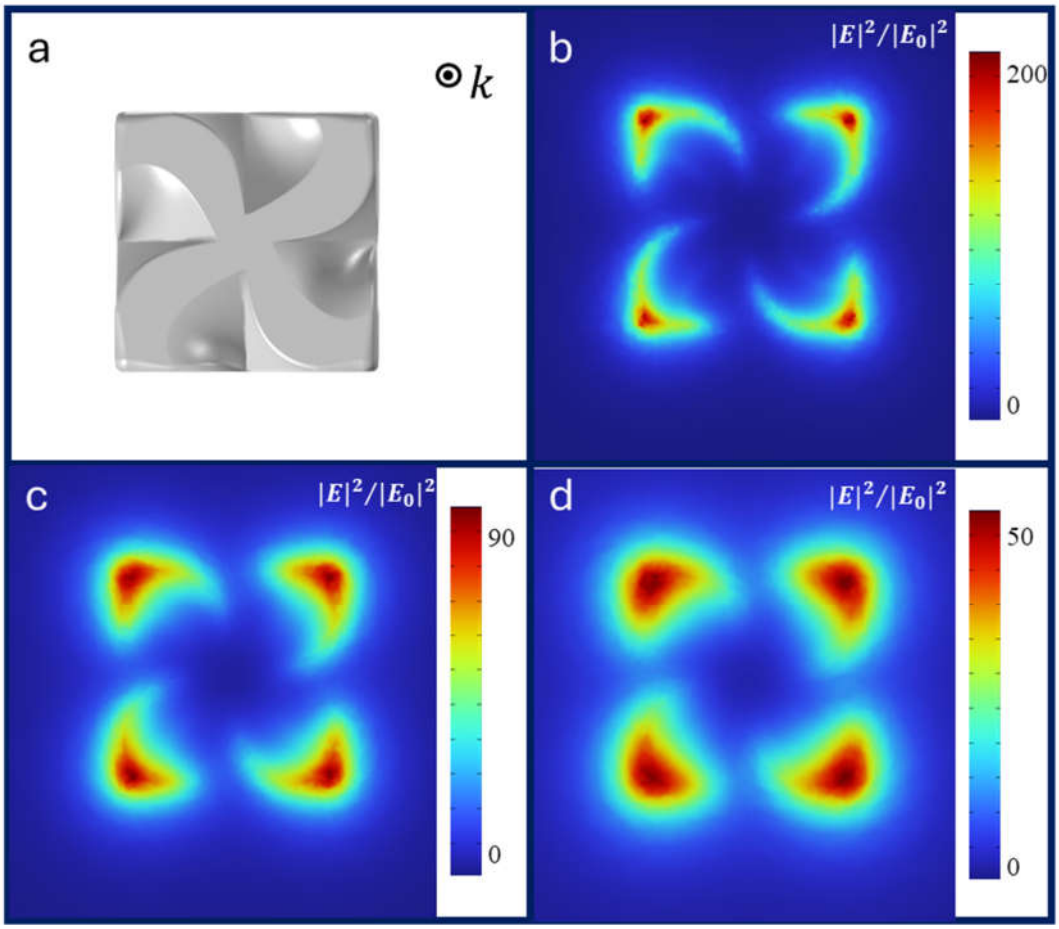

Figure 4.8. The simulated average electric field distribution of left and right circularly polarized excitation. (a) The top view of the chiral helicoid in the simulation. The excitation light is along out of plane direction. (b,c,d) Simulated averaged $|\boldsymbol{E}|^2/|\boldsymbol{E_0}|^2$ of left and right circularly polarized excitation 638nm light at (b) 5nm, (c) 10nm, (d) 15nm higher than the helicoid top face. $|\boldsymbol{E_0}|$ is the intensity of the incident electric field.

The other origin of PiFM signal is the optical force. The response of the tip to near field electric field can be modeled as a dipole. The near electric field around the tip imposes a time-averaged electromagnetic field to the tip[122,131]. The averaged force $\langle F \rangle$ can be expressed as:

$$\langle F \rangle = \alpha \nabla [\boldsymbol{E}]^2/4$$

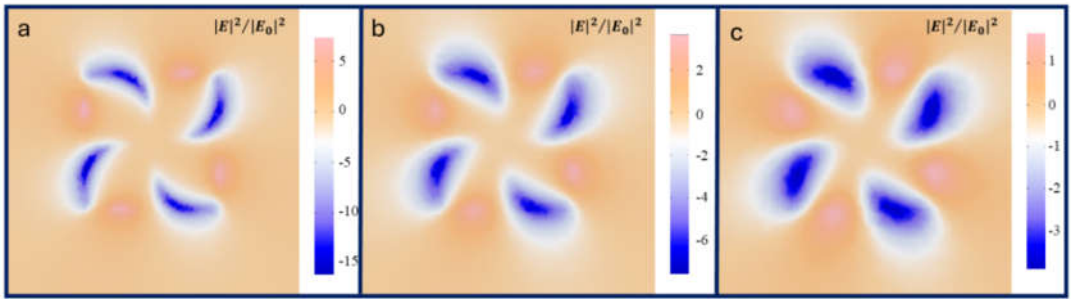

Figure 4.9. The differential electric field distribution of left and right circularly polarized excitation. (a,b,c) Simulated differential $|\boldsymbol{E}|^2/|\boldsymbol{E_0}|^2$ between left and right circularly polarized excitation 638nm light at (a) 5nm, (b) 10nm, (c) 15nm higher than the helicoid top face. $|\boldsymbol{E_0}|$ is the intensity of the incident electric field.

Where α is the polarizability of the tip dipole and $\lceil \boldsymbol{E} \rceil$ is the electric field at the position of tip dipole. Therefore, the optical force signal I_{OF} is relative to the square of near field electric field $|\boldsymbol{E}|^2$. From simulation, we can see that $|\boldsymbol{E}|^2$ are position dependent over the particle surface and also height dependent. We ran the FEM simulation of the chiral helicoid nanoparticle on fused silica substrate with bottom excitation and plot the averaged (Figure 4.8) and differential (Figure 4.9) square of near field electric field at the different height over the sample. The amplitudes are normalized to the intensity of incident electric field. In the measurement, the tip is in tapping mode with an average tip-sample distance of ~10nm. Therefore, we choose heights of 5nm, 10nm and 15nm to compare to our measurement. Notably, the three different height shows reasonable consistent features.

Because the optical force is dependent on the $\lceil \boldsymbol{E} \rceil^2$, we expect the optical force induced PiFM signal I_{OF} present similar spatial dependence as the simulated $|\boldsymbol{E}|^2/|\boldsymbol{E_0}|^2$ maps. Meanwhile, as we previously analyzed, the photothermal induced PiFM signal I_{PT} is expected to be uniform over the surface of the whole particle and therefore shouldn't change the spatial dependence of overall PiFM signal. We expect

that the measured PiFM signal $I = I_{OF} + I_{PT}$ shows the similar spatial dependence as the simulated $|\boldsymbol{E}|^2/|\boldsymbol{E_0}|^2$ maps. This allows us to directly compare the measured averaged and differential PiFM maps with the simulated $|\boldsymbol{E}|^2/|\boldsymbol{E_0}|^2$ map. Comparing Figure 4.7c with Figure 4.8, we can see that the spatial dependence of the average PiFM signal shows a reasonable agreement with averaged $|\boldsymbol{E}|^2/|\boldsymbol{E_0}|^2$ map. The stronger electric field at the four corners corresponding to the stronger averaged PiFM signal at the four corners. In Figure 4.9, the differential $|\boldsymbol{E}|^2/|\mathbf{E_0}|^2$ is strongest at the outer edge of the curved arms. This agrees with the fact that our measured differential PiFM signal in Figure 4.7c,d is also the strongest at the outer edge of the protruding curved arms. The disagreement of the measured differential signal and the simulation map can be attributed to the difference in the shape of this particular measured particle (see Figure 4.7a) and the simulation model.

4.4 Conclusion

In this chapter, we have developed the polarization dependent measurement of single plasmonic nanoparticles using chiral helicoid as an example with modified commercial optical AFM apparatus. Using cascading detection scheme, we were able to directly measure the differential PiFM signal. By analysis of the origin of the PiFM signals, our measured PiFM signal origins from a combination of optical force and photothermal expansion. We are looking forward to acquiring more data using different excitation wavelengths and different nanoparticles to build stronger correlation between the measurement and simulation. Nevertheless, this measurement technique enables us to direct characterize the near field of the chiral plasmonic structures, which provides a valuable tool to understand the couplings of the chiral

plasmonic resonance and generation of chiral optical field. Application of this technique on chiral plasmonic, semiconductor and molecule heterodyne complex would give direct evidence of intermedium coupling and the local chiral response and thus provide important insights into the application of such structures in chiral sensing, spin manipulation and etc.

Chapter 5: Spin-chiral measurement of chiral hybrid metal-semiconductor nanoparticles with ultrafast laser system

5.1 Introduction

The significance of chirality has been overwhelmingly addressed in various fields, ranging from understanding of evolution of life processes (e.g., origin of biological homochirality in nature), enantioselectivity in chemical reactions, to recent discovery of unusual large spin polarization through chiral organic molecules for Spintronics[1,79,132-141]. Most of the works has been limited to biological and organic chiral molecules. For example, chiral molecules have been found to exhibit chirality-induced spin selectivity (CISS) even at room temperature, in which spin state can be polarized by the existence of chiral molecules, as evidenced by experimental observation of spin-polarized photoemission and transport[41,132,142]. Furthermore, while many theoretical research efforts have shed light on the CISS with qualitative understanding of experimental results, a complete quantitative theory of the effect is still under scrutiny, and its microscopic origins are insufficiently understood, requiring substantial more work in both experiment and theory[143-152]. As compared with long history of chirality in biological and organic chiral realms, study of similar chirality-spin interplays in inorganic chiral structures has just started and been limited, mainly due to substantial challenges in achieving chiral inorganic structures as well as effective experimental techniques for measuring chirality-spin interactions. As compared with biological and organic systems, chiral crystalline inorganic materials and chiral hybrid structures as presented in Chapter 2 should offer better control of periodicity and

morphology from the atomic scale, thus representing unique test beds to understand and tailor chiroptical response and chirality-spin couplings.

So far, the major experimental technique for studying the CISS is based on electron/spin transport. However, various optical techniques have been developed to interrogate spins, including the time-resolved Faraday rotation (TRFR) or Kerr rotation (TRKR)[153]. As compared with spin transport techniques, time-resolved optical approaches can offer substantial advantages including absence of resistance mismatch and time-resolved capability.

In this chapter, we focus on low-temperature time-resolved optical studies of a new family of chiral hybrid nanostructures comprising chiral plasmonic metal cores and monocrystalline semiconductor quantum shells. The availability of chiral hybrid metal-semiconductor nanostructures can provide a platform to explore new chiral light-matter-spin interactions, thus enabling chiral Floquet engineering at the nanoscale[152, 154, 155].

5.2 Materials Design and Experimental Methods

5.2.1 Materials Synthesis and Characterizations

In this section, we describe step-by-step synthesis and characterizations of a new family of chiral hybrid nanostructures consisting of chiral Au nanocubic core and semiconductor CdS quantum shell with different structural parameters, which can provide a valuable platform for exploring emerging chirality-spin interactions at the nanoscale.

Synthesis of chiral Au nanocubes (NCs). The synthesis of chiral Au NCs follows the recipe of our previous work in Chapter 2.[16] The Au seed NCs are synthesized by a revised seed-mediated method.[63] Typically, 1 ml of Au seed NCs solution is added into 3 ml of 80 mM CTAC solution. A. 30~40 µl of 70 µM L-cysteine (or D-) solution is added and the mixed solution is kept stirring for 30 mins to have the cysteine molecules adsorbed on the surface of Au NCs. The mixed solution is centrifugated by 13200 rpm for 10 mins and the supernatant is discarded to remove the extra cysteine molecules in solution. The centrifugation process is repeated once. The precipitate is then redispersed into 1 ml of DI water, followed by addition of 3 ml of 80 mM CTAC solution and 200 µl of 0.1M ascorbic acid under stirring. 500 µl 1 mM $HAuCl_4$ solution is slowly injected into the mixture solution by syringe pump for 30 minutes. The chiral

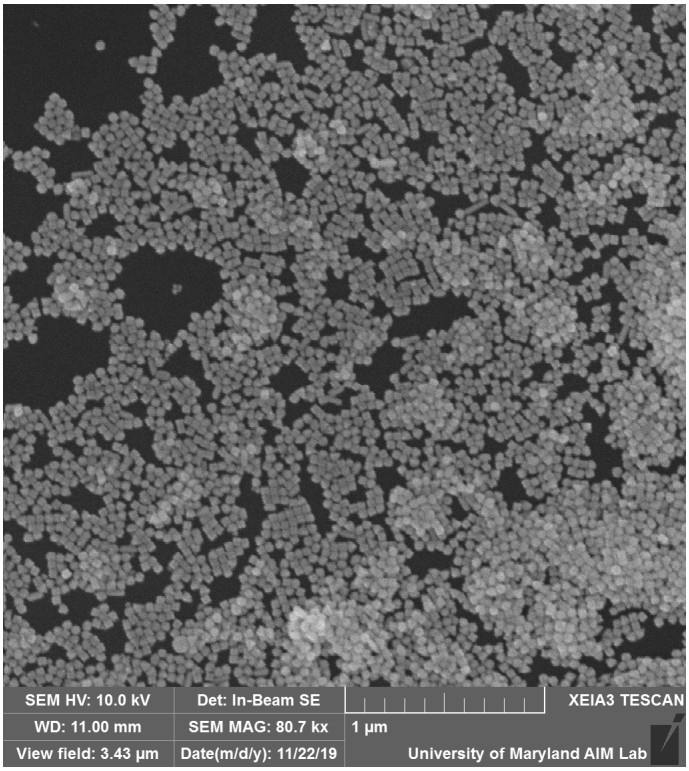

Figure 5.1. SEM image of typical chiral Au NCs utilized for growing chiral hybrid nanostructures.

Au NCs are washed out by centrifugation and redispersed into 4ml DI water. Typical quality of chiral Au NCs for the study presented in this Chapter is shown in Figure 5.1.

Synthesis of chiral Au@Ag core-shell nanoparticles (NPs): Typical, 1ml of chiral Au NCs are added into 8.1ml Di water and 1ml 0.2M CTAC solution. The mixture is put into a 60°C oil bath. Typically, 500ul 2mM $AgNO_3$ and 500ul 50mM AA were added drop by drop simultaneously into the mixture with active stirring. For thickness control of the Ag shell, 250ul 2mM $AgNO_3$ and 250ul 50mM AA are used for thinner shell and 750ul 2mM $AgNO_3$ and 750ul 50mM AA are used for thicker shell. The reaction is left for 3hrs in the 60°C oil bath. Finally, the chiral Au@Ag core-shell NPs are collected by centrifugation and redispersion into 4ml DI water.

Preparation of S precursor: 128mg S powder is added into 10ml oleylamine and 20ml oleic acid. The mixture is purged with N_2 and kept under the protection of N_2 for the whole process. The mixture is put in a 100°C oil bath and kept stirring for 20hrs. The S powder should be almost dissolved completely and gives a brown-orange colored solution. Undissolved S powder is removed by centrifugation at 8000rpm for 10mins. The supernatant is then diluted by 30ml toluene and kept for future use.

Synthesis of chiral Au@CdS nanoparticles (NPs): 1ml chiral Au@Ag NPs are centrifugated and redispersed into 1ml DMF. Meanwhile, 0.4ml S precursor and 10ul 1-decanethiol are added into 2ml toluene while stirring. The 1ml Au@Ag DMF solution is added into the previous mixture drop by drop. The reaction is left for 1hr at room temperature and the chiral Au@Ag_2S NPs are collected by centrifugation and redispersion into 2ml toluene. For synthesis of chiral Au@CdS NPs, 20ul oleylamine,

40ul oleic acid and 500ul 20mg/ml $Cd(NO_3)_2$ methanol solution are added into the 2ml chiral Au@Ag_2S toluene solution. The mixture is put in 50°C oil bath and kept stirring. 20ul TBP is added into the mixture to initialize the reaction. After 1hr stirring, the mixture is taken out and put in the sonication bath for better dispersion. The full reaction is reached by 2hrs in the 50°C oil bath under active stirring. Finally, the chiral Au@CdS NPs are collected by centrifugation with addition of 2ml ethanol and redispersion into 2ml toluene. For thickness control of the CdS shell, Au@Ag NPs with different thickness of Ag shell are used.

Synthesis of chiral Au@Ag_2S@CdS nanoparticles (NPs): 1ml chiral Au@Ag NPs are centrifugated and redispersed into 1ml DMF. Meanwhile, 40ul S precursor, 60ul oleylamine, 120ul oleic acid and 10ul 1-decanethiol are added into 2.18ml toluene while stirring. The 1ml Au@Ag DMF solution is added into the previous mixture drop by drop. The small amount of S precursor led to incomplete conversion of Ag to Ag_2S. Only an outer layer of Ag is converted to Ag_2S and left the inner layer of Ag intact. The reaction is left for 1hr at room temperature and the chiral Au@Ag@Ag_2S NPs are collected by centrifugation and redispersion into 2ml toluene. For synthesis of chiral Au@Ag@CdS NPs, 20ul oleylamine, 40ul oleic acid and 500ul 20mg/ml $Cd(NO_3)_2$ methanol solution are added into the 2ml chiral Au@Ag@Ag_2S toluene solution. The mixture is put in 50°C oil bath with active stirring. 20ul TBP is added into the mixture to initialize the reaction. After 1hr stirring, the mixture is taken out and put in the sonication bath for better dispersion. Full reaction is reached by 2hrs in the 50°C oil bath under active stirring. The chiral Au@Ag@CdS NPs are collected by centrifugation with addition of 2ml ethanol and redispersion into 2ml toluene. For the final step, 0.4ml

S precursor was added into the 2ml toluene solution of chiral Au@Ag@CdS NPs and the mixture is kept stirring at room temperature for 1hr. The resultant chiral Au@Ag2S@CdS NPs are collected by centrifugation with addition of 2ml ethanol and redispersion into 2ml toluene.

Phase transfer of chiral Au NCs from aqueous phase to oil phase: 1ml chiral Au NCs are centrifugated and redispersed into 1ml DMF. Meanwhile, 0.4ml S precursor is added into 2ml toluene while stirring. The 1ml chiral Au NCs in DMF is added into the previous mixture drop by drop. The mixture is left for 1hr stirring at room temperature and the chiral Au NCs are collected by centrifugation and redispersion into the mixture of 2ml toluene and 100ul oleylamine. The dispersion of chiral Au NCs in toluene is further improved by sonication in 50°C water bath for 2hrs and stirring overnight. The S precursor should create Au-S bonds at the surface of the chiral Au NCs and thus promote the ligand exchange. The CD of the chiral Au NCs remains after the transfer.

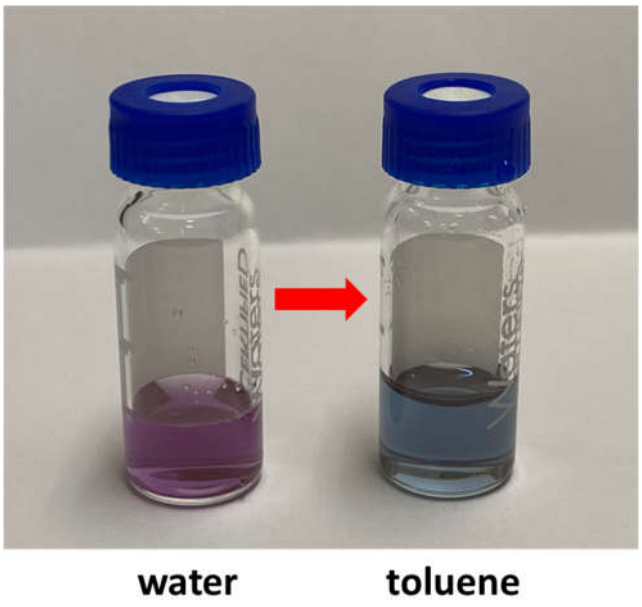

Figure 5.2. Phase transfer of chiral Au-CdS nanostructures from aquesous to toluene phase with excellent dispersion.

Figure 5.3. Photo of typical chiral Au-CdS thin films for low temperature optical spin measurements

Preparation of thin films samples for low temperature optical study: For low temperature optical spin measurements, it is crucial to achieve optically clear thin films with reduced light scattering. Typically, a stock solution of Poly(vinyl butyral-co-vinyl alcohol-co-vinyl acetate) (PVB) with $M_w \sim$ 50,000-80,000 in toluene (1:3 volume ratio) is prepared and is kept stirring until the polymer solution becomes clear. The chiral nanostructures transferred from aqueous phase are dissolved in toluene with concentration finely adjusted for optimum optical density of final thin film sample, and then mixed homogeneously with PVB stock solution. A few drops of mixture solution of chiral nanostructures in PVB are added into a pre-cleaned microscope slide. In order to ensure high quality and homogeneous free-standing thin films with minimum light scattering, extra care are needed for controlling such as evaporation speed of mixture solution by adjusting environmental pressure to avoid rapid evaporation of solvent.

Once the film is dry with desired optical density, it could be peeled off by adding liquid nitrogen into the backside of microscope slide, while the thin film side is protected by dry clean N2 gas to avoid water condensation during the peel-off step. It is important to note that for our current study, the density of colloidal chiral nanostructures is always kept sufficiently low to avoid inter-particle coupling or interactions. A typical optically clear chiral nanostructure thin film is shown in Figure 5.3.

Characterizations. For TEM, EDS mapping and linescan characterizations, all samples were prepared by adding one drop of solution containing desired nanostructures onto the 300 mesh copper grids with carbon support film (Ted Pella, 01820) and the 400 mesh copper grids with ultrathin carbon film on lacey carbon support film (Ted Pella, 01824). A JEM 2100 LaB6 and a JEM 2100 FEG TEM/STEM equipped with a field emission gun from Maryland Nanocenter at the University of Maryland were applied. Typical TEM imaging parameters were: 200 keV electron landing energy, 108 μA beam current, 0.5 s acquisition time and 2004 pixel by 1336 pixel digital resolution. The circular dichroism (CD) and absorption spectra of solutions samples are simultaneously acquired on a commercial JASCO J-815 spectrometer at room temperature using a cuvette with light path of 1.0 cm.

5.2.2 Low-Temperature All-Optical Spin Measurements and Chiral Spin Manipulations

Figure 5.4 shows schematically our home-built setup for low-temperature optical spin measurements and manipulations. All optical measurements in our current work are performed at 2K in a magneto-optical superconducting magnet system (SM4000-8) from Oxford Instruments with magnetic field up to 7 T. This temperature is achieved

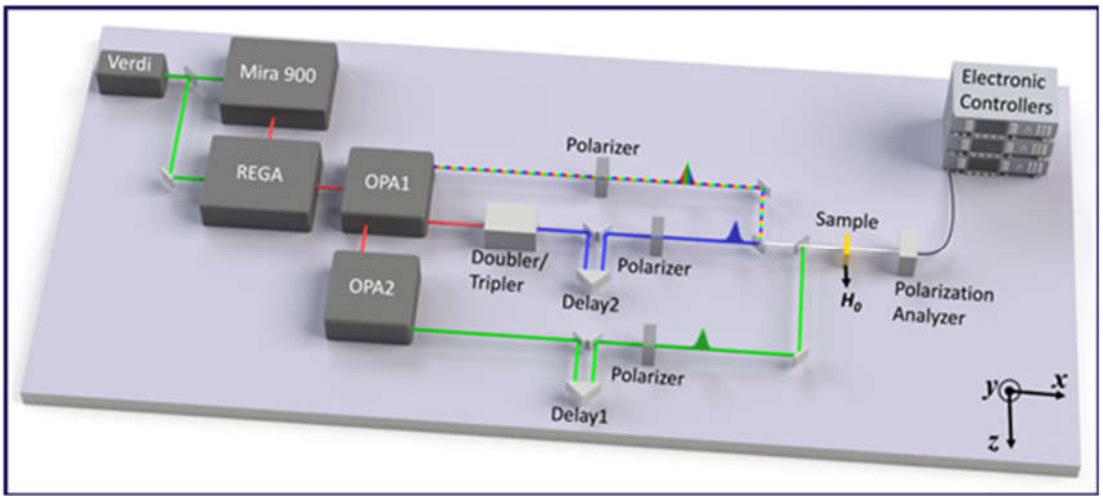

Figure 5.4. Home-built apparatus for ultrafast all-optical chiral-spin measurements. The laboratory reference coordinates are shown. All TRFR measurements are performed in the Voigt geometry.

by fully opening the needle valve to fill the sample space with LHe and pumping the sample space to reduce vapor pressure of LHe (the stable base temperature around 2 K could be achieved after a few minutes). All solution and solid samples were always prepared freshly right before loading to magneto-optical cryostat to avoid sample degradation. Under our experimental conditions in current work, we have not yet found any evidence of sample damage.

All ultrafast optical spectroscopy measurements in our current work were performed with the same laser system (Figure 5.4) that is designed and configured to meet experimental requirements for different samples and chiral-spin measurements and manipulations. The whole laser system is based on Coherent's regenerative amplifier laser (RegA) with home-made optical parametric amplifiers (OPAs): A 18 W CW solid-state 532 nm laser acts as pumps for both Ti:S and RegA simultaneously to generate seed laser input for OPA. Two OPAs are used in the system operating at 256 kHz repetition rate, producing multiple 100 fs pulses of energy tunable monochromatic

beam in the range of 0.55-1.15 eV (infrared OPA1) and 1.65-2.82 eV (visible OPA2), respectively. A home-made frequency doubler/tripler is also used with OPA1 to produce laser pulse in the range of 2.06-3.01 eV. Ultrafast broadband whitelights are also simultaneously produced by both OPAs. It is worth noting that the whitelight continuum from OPA typically exhibited a significant chirp (i.e., different wavelength components are temporally separated in whitelight pulse), and needed to be corrected if it is used as a time-resolved probe pulse. The chirp correction is carried out under second order approximation (i.e., the chirp of white-light continuum could be described as $\Delta t\left(\lambda\right)=C_0+C_1\lambda+C_2\lambda^2$), which is enough for our current work. We have used a routine two-photon absorption measurement to determine pump-probe cross correlation for the chirp correction[156]. Briefly, the monochromatic pump and the whitelight probe are spatially overlapped in a zinc oxide sample and the time delay is scanned for each transmitted whitelight component with selected photon energy. After collecting all the time-resolved data across the whole spectral range of whitelight, a second order polynomial fit is applied to fit the data with the above function. Once the coefficient C_i (i =0, 1, 2) are determined they could be used to add a corrected temporal offset to time-resolved measurements to correct the chirp effect. Single wavelength component of the whitelight pulse can be selected by using a mini-monochromator (Optometrics Corp.) and is generally used as a probe pulse to detect the spin polarization. Laser pulse width is often compressed before sample with home-made pulse compressor by using prism pairs and is calibrated with an autocorrelator from Femtochrome Research Inc. (Model FR-103MN).

Our all-optical spin experiments always involve three main key components: spin initialization along the laser propagation direction by using either circularly polarized or linearly polarized ultrafast optical pulse with the selective photon energy and intensity at the zero time delay (the circularly polarized pulse was created by the achromatic zero-order quarter waveplates with retardation accuracy of $\pm\lambda/100$ from Newport Corp.); spin detection by using linearly polarized probe pulse with the selective photon energy and intensity at any time delay Δt (the linearly polarized pulse was created by using a Glan-Thompson linear polarizer with high extinction ration more than 100,000 from Newport Corp.); a third ultrafast optical pulse with selective photon energy and intensity at the pre-determined time delay Δt_{tip} is applied to excite chiral plasmons of Au core in some experiments. The arrangements of all above ultrafast lasers are often needed to be configured and adjusted from Figure 5.4 to meet experimental requirements of different samples and experimental purposes. Typically, monochromatic output of visible OPA2 was used for spin initialization, and the monochromatic output of infrared OPA1 was used to produce the echo pulse train by using together with a home-made frequency doubler/tripler. In order to improve detection sensitivity, a home-made laser power stabilizer with feedback is always applied in optical path to reduce static noise level to below 0.1%. For every laser pulse a mechanical optical chopper with different modulation frequency is applied for lock-in detection. We have found that the lock-in detection at the sum frequency (that is generated from home-made circuit) and in a cascade detection scheme could efficiently isolate the effect of unexcited or partially excited quantum structures. All these considerations are crucial to achieve the high quality of the data presented in the current

study. For all the optical measurements in our current work, all pulse intensities are always adjusted and kept low enough to avoid potential Auger process and biexciton effects[157,158]. In general, the number of excited electron-hole pairs was always kept one order of magnitude (or more) lower than the total number of quantum structures in the focus volume (~ 75 μm in diameter).

In a regular TRFR measurement, the pump pulse arrives at the zero-time delay, spin polarization in sample at Δt is measured by a linearly polarized probe pulse with a home-made circuit, whose polarization plane is rotated by an amount proportional to the spin magnetization along the laser propagation direction. The zero-delay time is always corrected for the chirp of OPA laser as described above. When the in-plane magnetic field $\boldsymbol{H_0}$ is applied, the pump-injected spins comprise a coherent superposition of states quantized along the field direction and separate in energy by the Zeeman splitting. As the system evolved in time, the energy difference between the spin states produces a quantum beating of spin magnetization along the optical path, resulting in an oscillatory Faraday rotation of the time delayed linearly polarized probe pulse at the Larmor frequency (ν_L) that is field and sample dependent. Such TRFR technique has been successfully employed to study ensemble spin dynamics of colloidal nanostructures, including colloidal II-VI quantum dots and quantum shells[159-168]. From prior experimental and theoretical studies, it is generally believed that the spin observed in such colloidal semiconductor structures in various optical studies can be assigned to excitons due to quantum confinement effect. For example, more thorough investigation of size dependent excitonic *g*-factors showed good agreement between experiments and theories. From our TRFR measurement our *g*-factors also

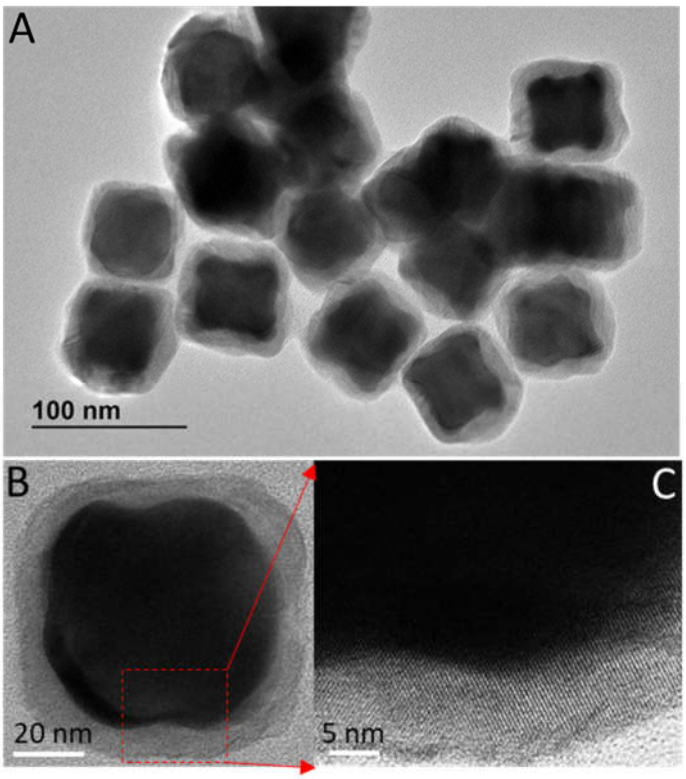

Figure 5.5. Chiral Au NCs (core)-CdS (shell) samples. (A) Typical large scale TEM image. (B) TEM image of individual chiral nanostructure. (C) High-resolution TEM of area highlighted in (B), showing single crystallinity of CdS quantum shell.

show good agreement with prior assignment of excitonic *g*-factors[162]. To that, we believe that the spin dynamics from the colloidal nanostructures investigated in our current study originated from excitons.

5.3 Results and Discussions

Figure 5.5 shows a typical sample quality of as-synthesized chiral *L*-Au NC (core)-CdS shell hybrid nanostructures, highlighting the existence of unique monocrystalline semiconductor shell, even though the morphology of Au core possesses inhomogeneous and uneven structural features. The exceptional quality CdS quantum shells can be attributed to the non-epitaxial synthetical method in our materials growth[55,62], and offer the basis of our study of chiral-spin interactions at the nanoscale. Dramatically, when different handedness of Au NCs are used as core for growing hybrid Au-CdS nanostructures, the hybrid nanostructures also become handed, and the hybrid nanostructures manifest opposite handedness depending on the handedness of chiral Au NC cores, as shown in Figure 5.6A. By comparing with pure chiral Au NCs with same handedness as presented in the Chapter 2, it is worth noting that the CD characteristics of hybrid Au-CdS nanostructures are completely different from their chiral core, which cannot be simply attributed to the change of the dielectric environment of chiral core NCs. This suggests the existence of inherent

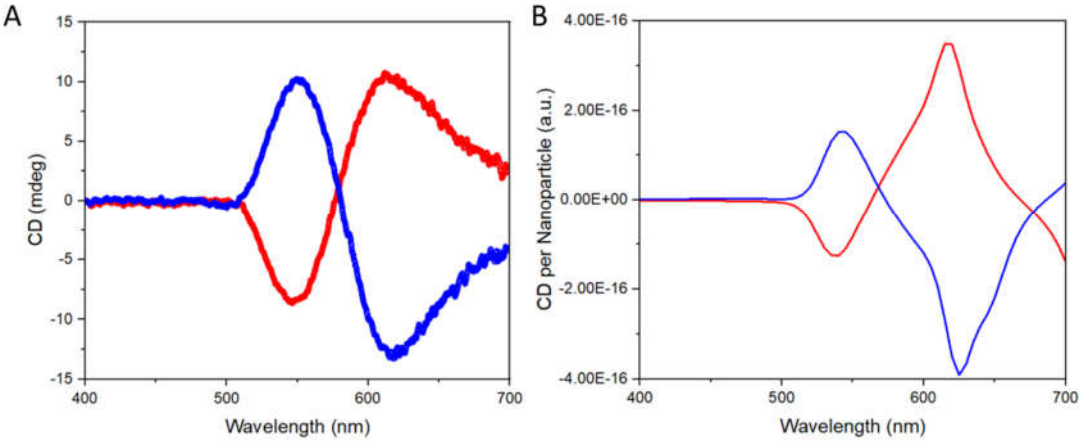

Figure 5.6. CD spectra of chiral Au NC-CdS hybrid nanostructures. (A) Experimental data. Red circles: (*L*-Au)-CdS; Blue circles: (*D*-Au)-CdS. (B) FEM simulated data of single chiral hybrid nanostructure. Red curve: (*L*-Au)-CdS; Blue curve: (*D*-Au)-CdS.

coupling between chiral core and its intimately contacted semiconductor shell. We have performed FEM simulation of CD spectra at the single nanostructure level (Figure 5.6B). Our simulation results have shown good agreement with experimental results, and addressed the CD features manifested in the hybrid chiral nanostructures.

We have studied spin dynamics of CdS quantum shells in chiral Au NCs-CdS hybrid nanostructures by performing TRFR measurements in Voigt geometry. Samples with various structural parameters, including handedness of core and thickness of shells, have been investigated and compared. Optical excitation of electrons from the valence to conduction states in many semiconductors follows optical selection rules, similar to the atoms and molecules. As a result, a circular polarization state of the incident excitation laser pulse is mandatory in a TRFR measurements in Voigt geometry in order to achieve non-zero initial spin polarization due to moment conservation in an optical excitation governed by the optical selection rules, while the

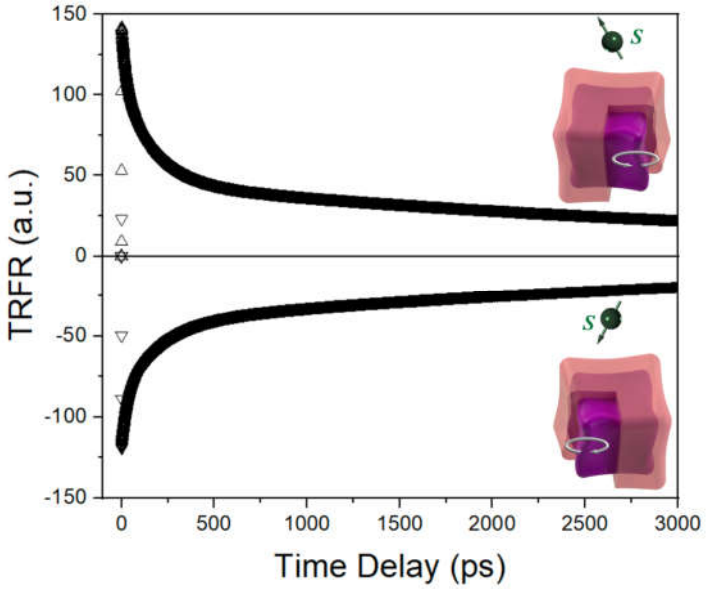

Figure 5.7. Zero-field TRFR spectra acquired by linearly polarized optical excitation. Upper triangles: (*L*-Au)-CdS; Down triangles: (*D*-Au)-CdS.

linear polarization state of incident beam, which can be considered as a linearly combination of left- and right- handed circularly polarized states, often lead to a null spin polarization in an undoped and unstrained semiconductor.

Figure 5.7 presents and compares the zero-field TRFR spectra of (*L*-Au) -CdS and (*D*-Au) -CdS samples that possess identical structural parameters of Au core and CdS shell except that the handedness of chiral Au core is opposite between two samples. Different from conventional TRFR measurements, the data are acquired by using linearly polarized optical excitation, which are supposed to result in a null spin polarization. The energies of both pump and probe pulses are tuned to match with the bandgap of CdS quantum shell, in which the pump pulse is 2.61 eV (1.72 mW) and the probe pulse is 2.49 eV (0.33 mW). Both pump and probes are linearly polarized. However, our data clearly show the appearance of large spin polarization in both samples, but with opposite sign of TRFR signal during the whole spin decay process. The zero-field spin life time of (*L*-Au) -CdS and (*D*-Au) -CdS samples are found to be ~3900 ps and 3700 ps, respectively. Two conclusions can be immediately drawn from the observations in Figure 5.7: First, the chirality inherent in the hybrid nanostructures (Figure 5.6) can lift the degeneracy of spin states in the semiconductor shells; Second, the spin polarization direction is dependent on the handedness of hybrid nanostructure.

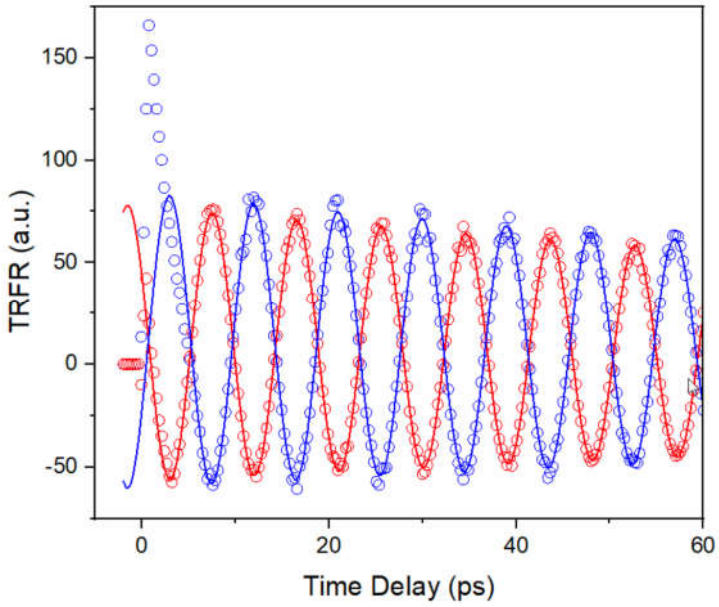

Figure 5.8. TRFR spectra at 4.2T acquired by linearly polarized optical excitation. Red circles: (*L*-Au)-CdS; Blue circles: (*D*-Au)-CdS. Red and blue are corresponding curve fittings.

In order to elucidate the observed non-zero TRFR signal under linearly polarized optical excitation in Figure 5.7, we have performed magnetic field-dependent studies in the Voigt geometry of TRFR experiments. Figure 5.8 shows the TRFR data acquired at the presence of horizontal magnetic field of $\boldsymbol{H_0}$=4.2 T, but under the optical excitation of linearly polarized pump pulses as employed in the Figure 5.7. A clear spin precession about the $\boldsymbol{H_0}$ is observed, confirming that the spin polarization can indeed be initialized by linearly polarized optical pulse in chiral hybrid nanostructures, and the opposite orientations of initial spins are uniquely determined by the handedness of their structures. We have used the following equation to fit TRFR spectra:

$$S_x(t) = S_0 \cdot e^{-\frac{t}{T_2^*}} \cdot \cos(2\pi\nu_L t + \phi_0) + A_1 + A_2 \cdot e^{-\frac{t}{\tau_0}}$$

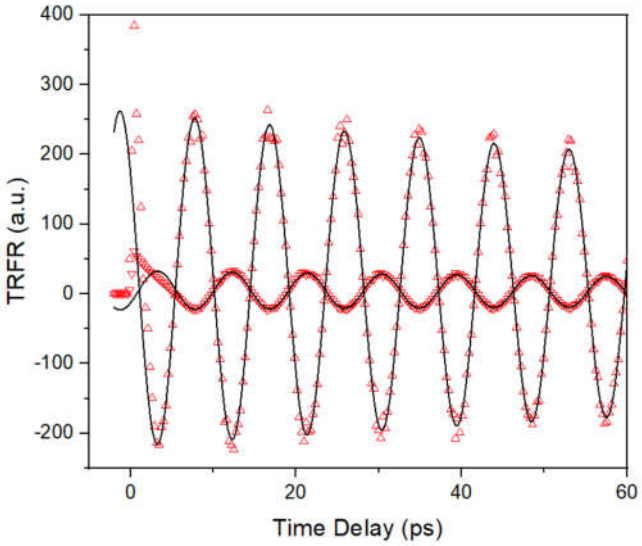

Figure 5.9. TRFR spectra at 4.2T acquired by circularly polarized optical excitation for the (L-Au)-CdS sample. Red up triangles: right- circularly polarized optical excitation; Red down triangles: left- circularly polarized optical excitation. Black soild curves are corresponding curve fittings.

where $S_x(t)$ represents the spin projection along x-axis at the time t, yielding the time-dependent TRFR signal. S_0 is the magnitude of initialized spin polarization (along x) by the optical excitation. ν_L, T_2^* and ϕ_0 are spin Larmor precession frequency, transverse lifetime and phase, respectively. A_1, A_2 and τ_0 are fitting parameters for background in a time-resolved optical measurement. The ν_L can be used to evaluate the Lande g-factor by the relationship of $\nu_L = \frac{g \cdot \mu_B \cdot H_0}{h}$, where μ_B and h are Bohr magneton and Planck constant, respectively. The fittings between theoretical and experimental data are excellent, yielding the g-factors of both samples are 1.88 and 1.89, respectively. Our measured g-factors agree with the range of those of CdS semiconductors reported from literatures[162,168,169].

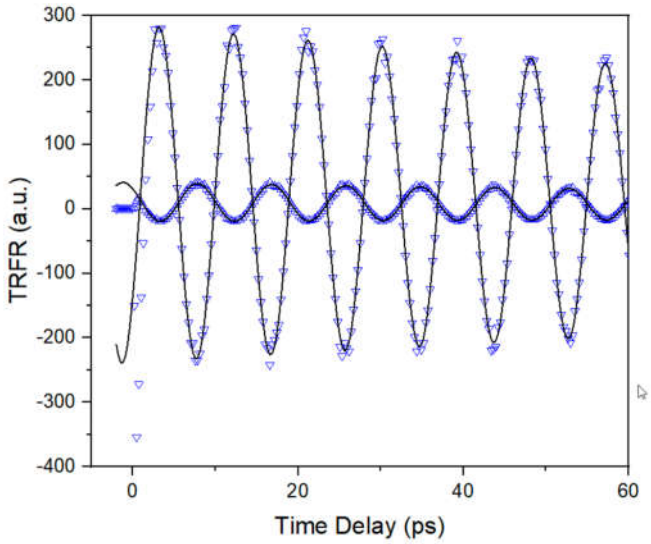

Figure 5.10. TRFR spectra at 4.2T acquired by circularly polarized optical excitation for the (*D*-Au)-CdS sample. Blue up triangles: right- circularly polarized optical excitation; Blue down triangles: left- circularly polarized optical excitation. Black soild curves are corresponding curve fittings.

We have further explored spin dynamics in chiral hybrid nanostructures by initializing spins through circularly polarized optical excitations, and summarized results in Figures 5.9 and 5.10. The experimental conditions (i.e. energy and power) for acquiring the results in Figures 5.9 and 5.10 are the same as that for Figure 5.8, except that the polarization of pump pulses are circularly polarized light. By comparing with results in Figure 5.8, there are a few observations: (1) Both left- and right- circularly polarized optical pump pulses can initialize spins in chiral hybrid nanostructures with opposite orientation of spin polarization. However, different from conventional achiral semiconductors, in which left- and right- circularly polarized light can result in equal magnitude of spin polarization but opposite orientation, such symmetry is broken in chiral hybrid nanostructures. Instead, the right- circularly polarized pump pulses can polarize substantially more spin than the left-circularly polarized light for the chiral (*L*-Au) -CdS sample, and vice versa for the (*D*-Au) -CdS

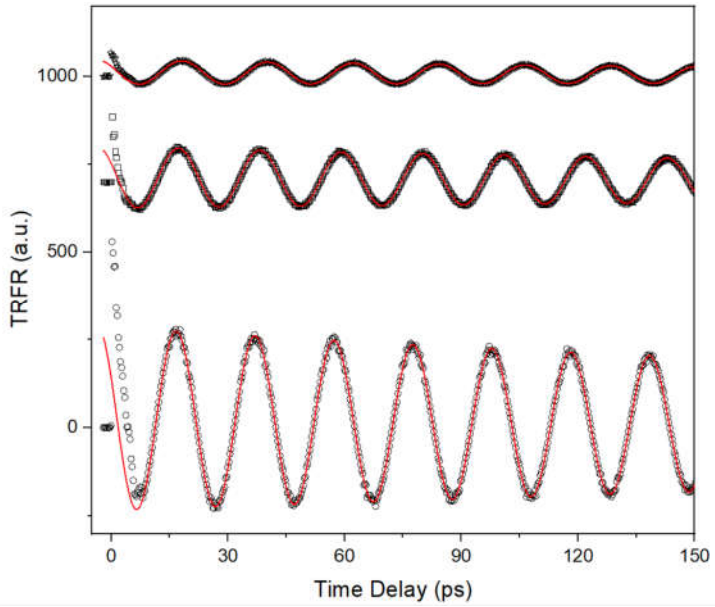

Figure 5.11. TRFR spectra of (*L*-Au)-CdS samples with three different CdS shell thickness at 1.8T. Spins are initialized by the linearly polarized optical excitation. Black circles: ~4.5nm; Black squares: ~7.5nm; Black stars: ~11nm. Square and star data are vertically shifted 700 and 1000, respectively, for the clarity purpose.

sample with opposite helicity. The difference in the magnitude of spin initialization can be more than ~ 8 times; (2) By comparing with spin initialization induced by linearly polarized pump pulses, one helicity of light can result in more spin polarization with same orientation, while the other helicity of light can only induce much weaker spin polarization with opposite orientation; (3) By comparing the *g*-factors determined from the TRFR spectra between the linearly polarized and circularly polarized pump pulses, we have found that they are the same. This confirms that the nature of spin polarization originated from the inherent handedness of the chiral hybrid structures is the same as that of spins induced by the conventional circularly polarized light; (4) By comparing with the CD characteristics in Figure 5.6, in which no measurable CD is observed in the wavelength regime of 400-500nm, the underlying mechanism of observed chirality induced spin polarization cannot be due

to imbalanced optical absorption of left- and right- circularly polarized light by the CdS quantum shells.

Furthermore, we have synthesized three different chiral hybrid (*L*-Au)-CdS nanostructures, in which the chiral Au NC cores remain the same but with three different averaged CdS shell thickness of 4.5nm, 7.5nm, and 11nm, respectively. We have compared their spin dynamics under linearly polarized optical excitations. Figure 5.11 shows one example at the $\boldsymbol{H_0}$=1.8T. A clear shell thickness dependence can be found. Three spin precessions manifest different Larmor frequencies at the presence of same external magnetic field, suggesting different *g*-factors. It has been found that the *g*-factor of semiconductors at the nanoscale shows strong size dependent due to quantum confinement. Our observation is consistent with the quantum confinement effect. Importantly, the initial magnitude of spin polarization induced by the pump pulses, $|S_0|$, shows strong dependence on the shell thickness. For the ~4.5nm CdS shell, the $|S_0|$ is almost 7 times of that from the ~11nm shell. This control experiment lends the support that the chirality induced spin polarization inherent in chiral hybrid Au-CdS nanostructures might be related the interface between chiral core and semiconductor shell.

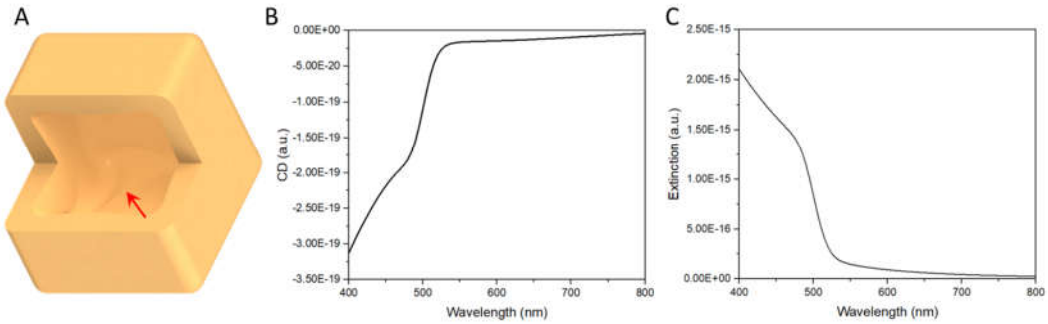

Figure 5.12. (A) Structure of the CdS shell in a chiral hybrid (*L*-Au)-CdS nanostructure. Inhomogeneous features (highlighted by red arrow) can be found to exist in the inner surface, which is imprinted from chiral *L*-Au NC core. (B) and (C) Computed CD and extinction spectra per CdS quantum shell from the structure presented in (A).

It is worth noting that the origin of chirality of Au NCs has been confirmed to be originated from the imbalanced exposure of chiral high Miller index facets on the surface of Au NCs (see also Chapter 2), and the chiral surface features of *L*-Au or *D*-Au NCs uniquely determine their handedness, resulting in chiral plasmons. If such uneven chiral surface features disappear by, for example, the overgrowth of another metal layer (Ag) with uniform outermost surface, their handedness can be diminished. However, this fact also suggests that the chiral surface features originating from the Au cores can be in-principle imprinted to the inner surface of semiconductor CdS quantum due to their intimate and seamlessly contact with chiral Au core during the non-epitaxial growth process.

To further explore this possibility and its potential effect in the observed chirality-induced spin polarization, we have constructed a model of CdS quantum shell in the hybrid structure by considering the fact that the structural chiral features on the surface of chiral Au cores can be imprinted to the inner surface of CdS shells during the non-epitaxial growth process (Figure 5.12A), and performed the FEM simulation

to evaluate its chiroptical response (Figure 5.12B). The model presented in Figure 12A is built by simply removing the chiral Au core in a hybrid (*L*-Au)-CdS structure utilized for computation in Figure 5.6B without further modification, thus representing the intrinsic property of CdS shell in a hybrid chiral nanostructure. Interestingly, our computations in Figure 5.12B have clearly revealed that the structural features appeared in the inner surface of CdS shell are chiral, and can induce intrinsic chirality of the CdS quantum shells in a chiral hybrid nanostructure. The computed CD magnitude of pure CdS shell by this mechanism is very small, thus making it negligible and impossible to detect in a hybrid chiral nanostructure as a whole (Figure 5.6B). Nevertheless, the existence of chiral characteristics in the inner surface of CdS shell could modify its electronic and spin properties.

There exist three possible mechanisms to understand chirality induced spin polarization observed in the chiral hybrid (*L*/*D*-Au)-CdS nanostructures: (1) Chiral Au NC core might have chirality induced magnetism. Recently, evidences showing that chiral molecules on the surface of metals or magnetic materials can alter their intrinsic magnetic properties have been reported[39,170-174]. We also performed a control experiment by measuring TRFR of pure chiral *L*-Au NCs, but so far we have not found any evidences that our chiral Au NCs possess magnetic properties; (2) Spins that are optically excited in the CdS quantum shell can be selectively scattered by its chiral inner surfaces to favor one particular spin states[144,145,150]; (3) The appearance of chiral structural features on the surface of semiconductor CdS shell might modify its spin-orbit coupling (SOC) and lift the degeneracy of spin levels to induce spin polarization[175].

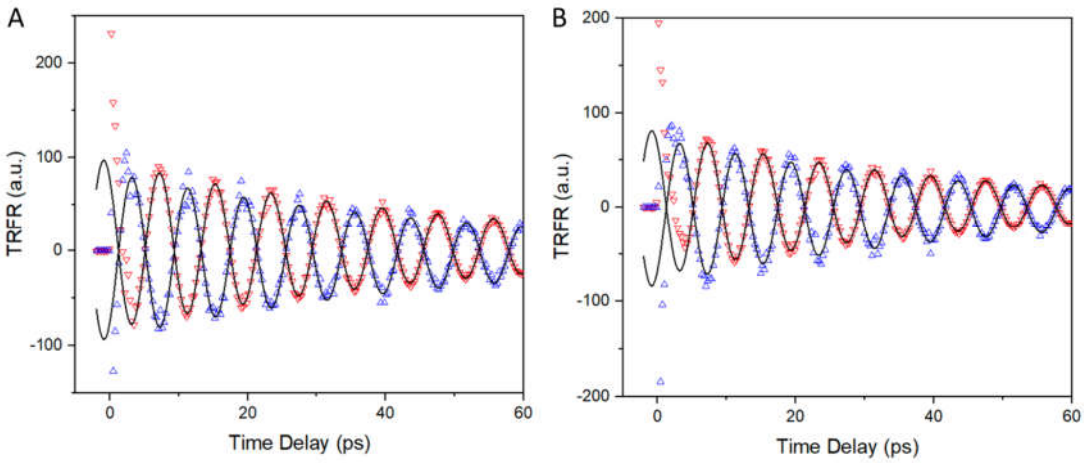

Figure 5.13. TRFR data at 4.5T acquired by the circularly polarized optical spin excitations. (A) (*L*-Au)-Ag_2S-CdS sample. (B) (*D*-Au)-Ag_2S-CdS sample. Down- and up- triangles are data acquired by using left- and right- circularly polarized pump pulses in a TRFR measurement, resepectively.

To confirm the effect of chiral interface in our observed chirality induced spin polarization experimentally, we have designed a new type of chiral hybrid nanostructures (*L*/*D*-Au)-Ag_2S-CdS comprising of two shells, Ag_2S and CdS shells, in which the outer most CdS shell doesn't have intimate contact with the surface of chiral *L*/*D*-Au NC core during the growth process. Therefore, the structural imprinting process observed in the prior chiral (*L*-Au)-CdS hybrid nanostructures should no longer be applied to the outermost CdS quantum shell. As a results, in contrast to the ((*L*/*D*-Au)-CdS samples, no chiral structural features should exist in the inner surface of CdS in the (*L*/*D*-Au)-Ag_2S-CdS samples. We have performed similar TRFR measurements with the (*L*-Au)-Ag_2S-CdS and (*D*-Au)-Ag_2S-CdS samples, and compared with their counter parts of (*L*-Au)-CdS and (*D*-Au)-CdS. Importantly, we have not observed net spin polarization in TRFR measurements for both samples by using linearly polarized optical excitation. Instead, when employing the circularly polarized optical excitations with same energy and average power in the

TRFR measurements of (*L*-Au)-Ag_2S-CdS and (*D*-Au)-Ag_2S-CdS samples, equal spin populations can be selectively induced with opposite orientations, and the spin orientation is merely determined by the helicity of light during the optical excitations and is independent on the handedness of chiral Au cores, as shown in Figure 5.13. This represents a stark contrast to those observations from the (*L*/*D*-Au)-CdS samples, suggesting that the CdS quantum shells in such samples behave as conventional semiconductors and their optical excitation is governed by the unmodified optical selection rules.

The interplay between light and matter has been the foundation of many fundamental physical and chemical processes with various applications. Harnessing light-matter interactions has been an intensive research field, and in-principle can allow operation of quantum states under new physical principles. For example, the optical Stark effect has enabled coherent quantum control schemes of spins and charges in semiconductors by "dressing" the energy levels. When a matter becomes chiral, chirality can emerge as a novel tuning knob in light-matter interactions as well as their enabled quantum controls. We have explored the emerging light-chiral matter interactions in our as-synthesized chiral hybrid nanostructures that uniquely integrate chiral plasmons with semiconductor at the nanoscale.

Experimentally, measuring differential polarization absorption/transmission between left- and right- circularly polarized light has been demonstrated to be a powerful tool to probe momentum-dependent quantum control dynamics[61,176,177]. We have modified such measurement scheme in our current study. In our experiment, we have set the circularly polarized ultrashort probe pulse to measure differential polarization

absorption of CdS quantum shell at the fixed probe energy and various time delay, while the energy of linearly polarized pump pulse at $\Delta t = 0$ is tuned to across the 1st plasmonic CD band of chiral Au NC core around 558nm. The differential polarization absorption of probe pulses is measured by using a PEM that provides modulation of left- and right- circularly polarized light at 50 kHz. Both (*L*-Au)-Ag_2S-CdS and (*D*-Au)-Ag_2S-CdS samples are studied by this scheme, and their results are presented in Figure 5.14. For both samples, a clear peak with maximum differential polarization absorption can be seen at the zero-time delay between the pump and probe pulses when the pump energy matches with the CD peak. However, the sign of peak is opposite between these two samples, showing the dependence on the handedness of hybrid nanostructures. A few important implications can be immediately obtained from this experiment: (1) The appearance of differential polarization absorption only occurs when the pump and probe overlap at the $\Delta t = 0$, confirming that our observation is a pump-dependent process. The time duration of the differential polarization absorption peak is ~150 fs, and the underlying light-chiral matter coupling is an ultrafast process; (2) Because the chiral plasmonic energy of Au core is much smaller than the bandgap energy of CdS shell (see Figure 5.12), the pump itself cannot directly excite charge or spin carriers in the CdS quantum shell. The sizable differential polarization absorption measured at the excitonic energy of CdS quantum shell suggest that excitation of chiral plasmons of the Au core can modify spin states of CdS shell through virtual light-matter coupling, similar to the a.c. optical Stark effect; (3) Although we have detected similar differential polarization absorption spectra from both samples with different handedness, the sign of their differential

polarization absorption is opposite, and is handedness dependent; (4) The structural handedness dependent differential polarization absorption immediately suggests that when the chirality is integrated in a light-matter coupling process, a net spin splitting of electrons can be induced, similar to Zeeman splitting at the presence of external magnetic field, and the orientation of chiral plasmons induced effective magnetic field ($\boldsymbol{H_{chiral}}$) is along the laser direction and uniquely defined by the structural chirality introduced.

This light-chiral matter coupling revealed in Figure 5.14 has never been observed before, and is unique in our chiral hybrid nanostructures due to the nanomaterials design. Importantly, availability of ultrafast light induced $\boldsymbol{H_{chiral}}$ provides a viable approach to single spin manipulation by applying a light-induced torque, $\boldsymbol{\tau}$ to the spin: $\boldsymbol{\tau} = (g \cdot \mu_B)\boldsymbol{S} \times \boldsymbol{H_{chiral}}$, where $\boldsymbol{S}$ is electron spin. As a direct result of this light induced torque, spin can be rotated from its original polarization with a rotation angle determined by the orientation of spin $\boldsymbol{S}$ and intensity of $\boldsymbol{H_{chiral}}$ (the orientation of $\boldsymbol{H_{chiral}}$ is fixed by the handedness of chiral hybrid nanostructure, as shown in Figure 14). To demonstrate spin manipulation by the $\boldsymbol{H_{chiral}}$, we have designed following

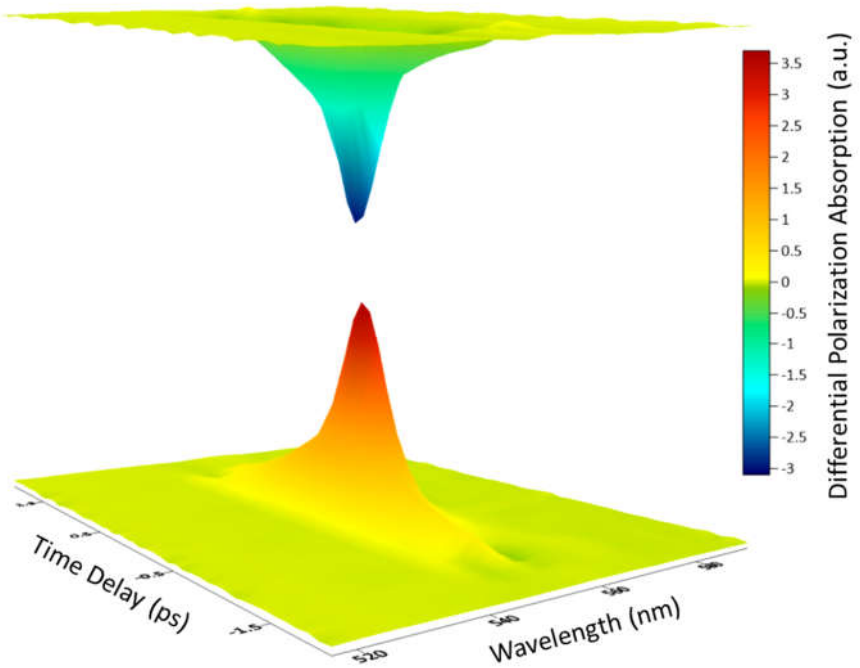

Figure 5.14. Temporal and spectral mapping of differential polarization absorption of CdS shell in a chiral hybrid nanostructure as a function of excitation wavelength of chiral plasmons and time delay. (Bottom) (*L*-Au)-Ag_2S-CdS sample. (Top) (*D*-Au)-Ag_2S-CdS sample. data at 4.5T acquired by the circularly polarized optical spin excitations. (A) (*L*-Au)-Ag_2S-CdS sample. (B) (*D*-Au)-Ag_2S-CdS sample. Down- and up- triangles are data acquired by using left- and right- circularly polarized pump pulses in a TRFR measurement, resepectively.

experimental sequence. A circularly polarized laser pump pulse (whose energy is tuned to 2.49 eV) is applied at $\Delta t = 0$ along the *x*-axis to create spin initialization, $\boldsymbol{S_0}$ (either -*x* or +*x*). An external d.c. magnetic field $\mathbf{H_0}$ is applied along the *z* axis to induce spin precession about this field. A linearly polarized probe pulse whose energy is tuned to 2.61 eV is applied at different time delay Δt to monitor spin orientation with time (i.e. before and after application of tipping pulse). For spin manipulation, $\boldsymbol{H_{chiral}}$ is induced by applying a linearly polarized tipping pulse with energy tuned to match with the CD peak at 2.21eV. For our current study, this tipping pulse is always

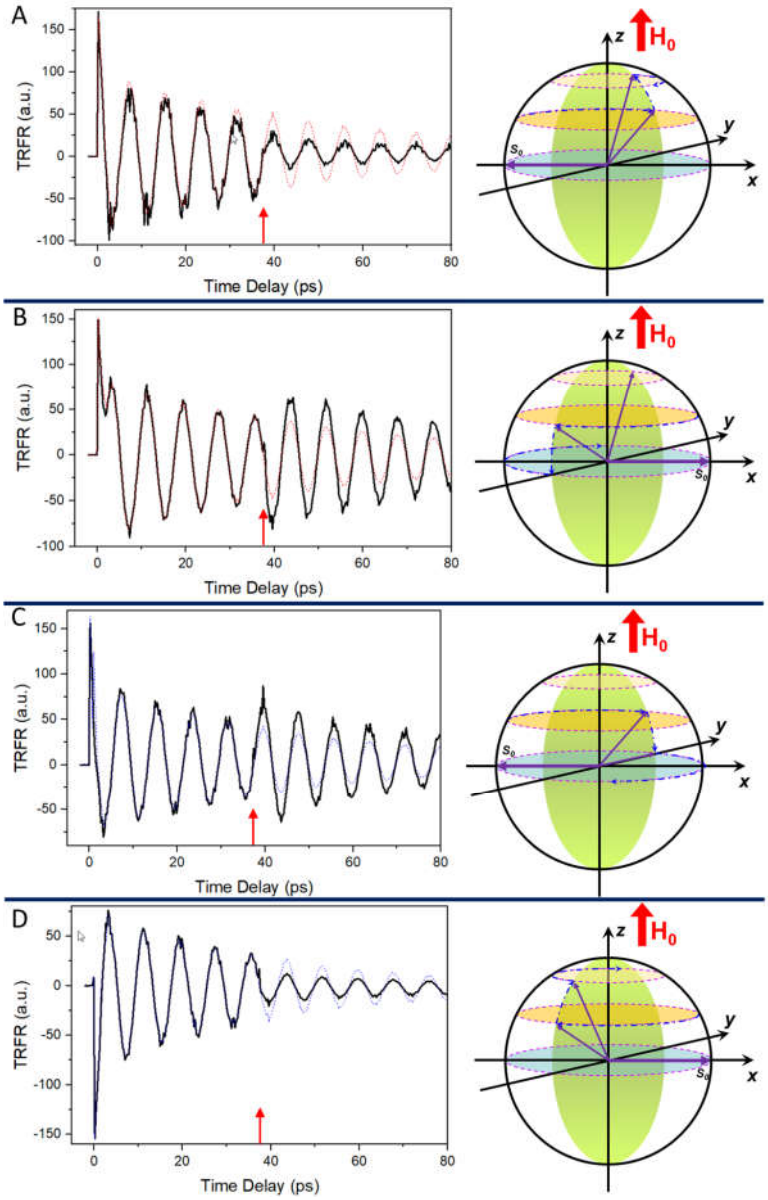

Figure 5.15. Ultrafast spin manipulation of CdS quantum shell by $\boldsymbol{H}_{chiral}$. A linearly polarized tipping pulse with energy of 2.21eV is always applied at $\Delta t = 37.29\ ps$ (red arrow). An external magnetic field is applied at H_0=4.5T to induce spin precession. Bloch sphere is presented on the right for each manipulation to elucidate spin control path. To evaluate effect of $\boldsymbol{H}_{chiral}$, a TRFR trace (dashed curve) without application of the tipping pulse is also acquired under the same pump and probe conditions and is presented for comparison. (A) Spin is initialized by using left- circularly polarized pump in (*L*-Au)-Ag_2S-CdS sample; (B) Spin is initialized by using right- circularly polarized pump in (*L*-Au)-Ag_2S-CdS sample; (C) Spin is initialized by using left-circularly polarized pump in (*D*-Au)-Ag_2S-CdS sample; (D) Spin is initialized by using right- circularly polarized pump in (*D*-Au)-Ag_2S-CdS sample.

applied at the fixed time delay $\Delta t = 37.3\ ps$. This specific time delay is selected based on g-factor and external magnetic field so that the spin is pecessed to the y-axis at the arrival of the tipping pulse, which should provide maximum $\boldsymbol{\tau}$. Because the orientation of $\boldsymbol{H_{chiral}}$ is determined by the structural handedness, we have studied both (L-Au)-Ag_2S-CdS and (D-Au)-Ag_2S-CdS samples. In order to illustrate proposed spin manipulation process and assist our understanding of the underlying physics, Figure 5.15 summarizes results for four scenarios with different combinations of orientation of initialized spins and $\boldsymbol{H_{chiral}}$. The Bloch sphere in the laboratory reference frame is also used to elucidate spin rotation. A few important findings from this experiment are summarized below. First, for each sample, by comparing with TRFR trace acquired without application of tipping pulse (dashed curves), the tipping pulse applied can either reduce or enhance TRFR magnitude, depending on the orientation of initial spin, $\boldsymbol{S_0}$. The change of TRFR amplitude can be attributed to spin flip out of its original precession plane, depending on the orientation of $\boldsymbol{\tau}$. The dependence on the initial spin orientation occurs because when the spins are initialized oppositely, they could preces with a π-phase difference. As a result, at the time that the tipping pulse is applied, the spins could be along opposite directions, resulting in the opposite $\boldsymbol{\tau}$ and thus different rotation direction. Second, when the spins are initialized along the same orientation (along $\boldsymbol{x}$ or $\boldsymbol{-x}$) in different samples, (L-Au)-Ag_2S-CdS or (D-Au)-Ag_2S-CdS samples, the effect of tipping pulses is also different, although they are applied at the same delay time. When the spins are initialized in the same orientation, they could always preces in-phase between two samples, because the only difference between these two samples is their handedness, while other structural

parameters, including size of Au core and thicknesses of CdS and intermediate Ag_2S shells are intentionally designed to be the same. Therefore, observation of different spin rotation caused by the tipping pulses can be attributed to the opposite orientation of the light induced $\boldsymbol{H_{chiral}}$ between these two samples. This comparison is consistent with our results from measurement of differential polarization absorption (Figure 5.14), and the orientation of light induced $\boldsymbol{H_{chiral}}$ is related to the structural handedness. Third, when the spin is rotated our of its original precession plane by the light induced $\boldsymbol{H_{chiral}}$, we have not found any detectable phase change in all spin manipulations, suggesting that the spin manipulation induced by the $\boldsymbol{H_{chiral}}$ is a coherent process.

5.4 Conclusions

In this Chapter, we have studied various chirality-spin interplays in a family of chiral hybrid nanostructures, which can uniquely integrate chirality, plasmons and excitons (spins) in a single nanoscale entity with tunable structural parameters. Importantly, we have shown that nanoscale structural chirality can induce spin polarization in low-dimensional condensed matter systems. Through materials design, we have further demonstrated that the integration of chiral plasmons of metal with semiconductor can lead to novel light-chiral matter interactions. Through such coupling, nanoscale chiral plasmon has been demonstrated to induce effective magnetic field in its nearby semiconductor that is uniquely determined by the structural handedness. Such chirality induced effective magnetic field can offer a viable mechanism for realizing ultrafast spin manipulation at the nanoscale. Different ultrafast spin manipulation processes by using chirality induced effective magnetic field have been achieved. Our

present work should open up a variety of avenues in relevant science and technologies. The concept of using periodic excitation of chiral plasmons to generate effective ultrafast magnetic fields introduces an exciting paradigm for chiral Floquet engineering, unlocking new possibilities in quantum control. Integrating these all-inorganic chiral nanostructures with other quantum materials could lead to hybrid systems with unprecedented functionalities, setting the stage for transformative advancements in quantum information science and next-generation quantum devices.

Chapter 6: Summary and Outlook

In this dissertation, we have proposed and demonstrated several new methods and results in the field of nanoscale chirality including synthesis, modeling, characterization and application of chiral inorganic nanoparticles. There are several future studies and applications that we can immediately envision based on this dissertation.

Firstly, we have presented a general strategy of synthesis of chiral plasmonic nanoparticles by breaking surface symmetry with introduction of chiral molecules. This proposed strategy could be readily applied to broader selections of inorganic materials and different shaped nanoparticles which provides intriguing opportunities in chirality-related applications. For example, palladium (Pd) as a plasmonic metal is known for its application as a catalyst. Following the same synthesis strategy, we can introduce chirality into Pd nanoparticles for the application of enantio-catalysis. We have demonstrated that the robustness of the chiral plasmonic nanoparticles could enable further synthesis of chiral plasmonic-semiconductor heterostructure with the preservation of chirality. We can envision further studies to explore and demonstrate the chirality-related effects in the chiral plasmonic-semiconductor heterostructures such as chirality induced spin selectivity and chiral hot electron generation.

Secondly, we utilized coupled oscillator model to theoretically investigate plasmon-chiral coupling and predicted enhanced CD, inversion of chirality, mode splitting in different coupling regimes. With careful analysis of the physical origin of the CD, we were able to explain the origins of the various chiroptical responses. The FEM simulation confirmed the existence of our predicted chiroptical responses validating

our theoretical analysis. This simple but effective coupled oscillator model provided a valuable tool towards a deep understanding of the plasmon-chiral system. Although our current work focused on the coupling of achiral plasmon and chiral medium, with modification of the oscillator parameters we can easily extend our scope to the coupling of chiral plasmon and chiral medium, which play important roles in chiral sensing. Furthermore, extending our oscillator model with nonlinear coupling terms would enable the theoretical investigation into the nonlinear chiroptical response of the plasmon-chiral system.

Thirdly, we have developed a polarization dependent PiFM measurement of single chiral plasmonic nanoparticles. The PiFM signal was analyzed and attributed to the near field distribution of the chiral plasmonic electric field. The PiFM provides nm scale spatial resolution which is beyond the resolution of far field optical measurements. This technique enables direct characterization of chiral near field which represents a significant step to the understanding and application of the nanoscale chirality. We are developing the integration of s-SNOM technique and our current PiFM technique which would provide a deeper understanding of near field chiroptical response. Meanwhile, another exciting direction is introducing ultrafast laser into the optical AFM apparatus. As we detailed in Chapter 4, the photothermal process of the chiral plasmonic heating is within around a few ns timescale. An optical AFM measurement combined with ultrafast laser and pump-probe optical measurements would enable us to resolve the dynamic of photothermal process in both time domain and spatial domain.

Lastly, we performed ultrafast optical measurements on the chiral hybrid plasmonic-semiconductor nanostructures synthesized following the strategy in Chapter 2. Differently from organic counterparts, our inorganic chiral hybrid structure offers structural flexibility, precise control, and tailorable quantum effects making it ideal testbed for investigation of chirality-spin interplay. We have observed that nanoscale structural chirality can induce strong spin polarization in the semiconductor shell. We further demonstrated dynamic chirality in semiconductors and coherent spin manipulation through chirality-induced effective magnetic field by the active control of near-field chiral plasmon underscoring its potential as a powerful platform for spin-based quantum technologies. The concept of using periodic excitation of chiral plasmons to generate effective ultrafast magnetic fields introduces an exciting paradigm for chiral Floquet engineering, unlocking new possibilities in quantum control.

Bibliography

1. Nadi, N., *Chirality in Biological Nanospaces*. (CRC Press, 2011).
2. L. Nguyen, H. He, and C. Pham-Huy, *Chiral Drugs: An Overview*, International journal of biomedical science: IJBS **2**, 85 (2006).
3. Y. P. Svirko and N. I. Zheludev, *Polarization of light in nonlinear optics*. (Wiley-VCH, 2000), p.240.
4. W. H. Brooks, W. C. Guida, and K. G. Daniel, *The Significance of Chirality in Drug Design and Development*, Current Topics in Medicinal Chemistry **11**, 760 (2011).
5. M. Hentschel, M. Schäferling, X. Duan, H. Giessen, and N. Liu, *Chiral plasmonics*, Sci. Adv. **3**, e1602735 (2017).
6. E. S. A. Goerlitzer, A. S. Puri, J. J. Moses, L. V. Poulikakos, and N. Vogel, *The Beginner's Guide to Chiral Plasmonics: Mostly Harmless Theory and the Design of Large-Area Substrates*, Adv. Opt. Mater. **9**, 2100378 (2021).
7. A. Ben-Moshe, S. G. Wolf, M. B. Sadan, L. Houben, Z. Fan, A. O. Govorov, and G. Markovich, *Enantioselective control of lattice and shape chirality in inorganic nanostructures using chiral biomolecules.*, Nat. Commun. **5**, 4302 (2014).
8. P.-p. Wang, S.-J. Yu, A. O. Govorov, and M. Ouyang, *Cooperative expression of atomic chirality in inorganic nanostructures*, Nat. Commun. **8**, 14312 (2017).
9. X. Gao, B. Han, X. Yang, and Z. Tang, *Perspective of Chiral Colloidal Semiconductor Nanocrystals: Opportunity and Challenge*, Journal of the American Chemical Society **141**, 13700 (2019).
10. J. K. Gansel, M. Thiel, M. S. Rill, M. Decker, K. Bade, V. Saile, G. von Freymann, S. Linden, and M. Wegener, *Gold Helix Photonic Metamaterial as Broadband Circular Polarizer*, Science **325**, 1513 (2009).
11. Y. Svirko, N. Zheludev, and M. Osipov, *Layered chiral metallic microstructures with inductive coupling*, Applied Physics Letters **78**, 498 (2001).
12. R. Zhao, L. Zhang, J. Zhou, T. Koschny, and C. M. Soukoulis, *Conjugated gammadion chiral metamaterial with uniaxial optical activity and negative refractive index*, Physical Review B **83**, 035105 (2011).
13. M. Decker, M. Ruther, C. E. Kriegler, J. Zhou, C. M. Soukoulis, S. Linden, and M. Wegener, *Strong optical activity from twisted-cross photonic metamaterials*, Opt. Lett. **34**, 2501 (2009).
14. H.-E. Lee, H.-Y. Ahn, J. Mun, Y. Y. Lee, M. Kim, N. H. Cho, K. Chang, W. S. Kim, J. Rho, and K. T. Nam, *Amino-acid- and peptide-directed synthesis of chiral plasmonic gold nanoparticles*, Nature **556**, 360 (2018).
15. H.-E. Lee, R. M. Kim, H.-Y. Ahn, Y. Y. Lee, G. H. Byun, S. W. Im, J. Mun, J. Rho, and K. T. Nam, *Cysteine-encoded chirality evolution in plasmonic rhombic dodecahedral gold nanoparticles*, Nat. Commun. **11**, 263 (2020).

16. H. Liu, A. E. Vladár, P.-P. Wang, and M. Ouyang, *Tuning Geometric Chirality in Metallic and Hybrid Nanostructures by Controlled Nanoscale Crystal Symmetry Breaking*, J. Am. Chem. Soc. **145**, 7495 (2023).
17. A. Kuzyk, R. Schreiber, Z. Fan, G. Pardatscher, E.-M. Roller, A. Högele, F. C. Simmel, A. O. Govorov, and T. Liedl, *DNA-based self-assembly of chiral plasmonic nanostructures with tailored optical response*, Nature **483**, 311 (2012).
18. Q. Zhang, T. Hernandez, K. W. Smith, S. A. Hosseini Jebeli, A. X. Dai, L. Warning, R. Baiyasi, L. A. McCarthy, H. Guo, D.-H. Chen, J. A. Dionne, C. F. Landes, and S. Link, *Unraveling the origin of chirality from plasmonic nanoparticle-protein complexes*, Science **365**, 1475 (2019).
19. L. M. Kneer, E.-M. Roller, L. V. Besteiro, R. Schreiber, A. O. Govorov, and T. Liedl, *Circular Dichroism of Chiral Molecules in DNA-Assembled Plasmonic Hotspots*, ACS Nano **12**, 9110 (2018).
20. A. O. Govorov and Z. Fan, *Theory of chiral plasmonic nanostructures comprising metal nanocrystals and chiral molecular media*, ChemPhysChem **13**, 2551 (2012).
21. T. J. Davis and D. E. Gómez, *Interaction of localized surface plasmons with chiral molecules*, Phys. Rev. B **90**, 235424 (2014).
22. Q. Cheng, J. Yang, L. Sun, C. Liu, G. Yang, Y. Tao, X. Sun, B. Zhang, H. Xu, and Q. Zhang, *Tuning the Plexcitonic Optical Chirality Using Discrete Structurally Chiral Plasmonic Nanoparticles*, Nano Lett. **23**, 11376 (2023).
23. C. He, J. Guo, L. Jin, X. Deng, J. Li, X. Liang, K. Liang, and L. Yu, *The Mechanism and Fine-Tuning of Chiral Plexcitons in the Strong Coupling Regime*, Nano Lett. **23**, 9428 (2023).
24. N. J. Greenfield, *Using circular dichroism spectra to estimate protein secondary structure*, Nat. Protoc **1**, 2876 (2006).
25. A. J. Miles, R. W. Janes, and B. A. Wallace, *Tools and methods for circular dichroism spectroscopy of proteins: a tutorial review*, Chem. Soc. Rev. **50**, 8400 (2021).
26. L.-Y. Wang, K. W. Smith, S. Dominguez-Medina, N. Moody, J. M. Olson, H. Zhang, W.-S. Chang, N. Kotov, and S. Link, *Circular Differential Scattering of Single Chiral Self-Assembled Gold Nanorod Dimers*, ACS Photonics **2**, 1602 (2015).
27. H. Zhu, J. Yi, M.-Y. Li, J. Xiao, L. Zhang, C.-W. Yang, R. A. Kaindl, L.-J. Li, Y. Wang, and X. Zhang, *Observation of chiral phonons*, Science **359**, 579 (2018).
28. W. J. Choi, K. Yano, M. Cha, F. M. Colombari, J.-Y. Kim, Y. Wang, S. H. Lee, K. Sun, J. M. Kruger, A. F. de Moura, and N. A. Kotov, *Chiral phonons in microcrystals and nanofibrils of biomolecules*, Nat. Photon. **16**, 366 (2022).
29. H. Ueda, M. García-Fernández, S. Agrestini, C. P. Romao, J. van den Brink, N. A. Spaldin, K.-J. Zhou, and U. Staub, *Chiral phonons in quartz probed*

by X-rays, Nature **618**, 946 (2023).
30. T. Wang, H. Sun, X. Li, and L. Zhang, *Chiral Phonons: Prediction, Verification, and Application*, Nano Lett. **24**, 4311 (2024).
31. J. Yamanishi, H.-Y. Ahn, H. Yamane, S. Hashiyada, H. Ishihara, K. T. Nam, and H. Okamoto, *Optical gradient force on chiral particles*, Sci. Adv. **8**, eabq2604 (2022).
32. S. B. Wang and C. T. Chan, *Lateral optical force on chiral particles near a surface*, Nat. Commun. **5**, 3307 (2014).
33. A. Hayat, J. P. B. Mueller, and F. Capasso, *Lateral chirality-sorting optical forces*, Proc Natl Acad Sci **112**, 13190 (2015).
34. H. Chen, C. Liang, S. Liu, and Z. Lin, *Chirality sorting using two-wave-interference--induced lateral optical force*, Phys. Rev. A **93**, 053833 (2016).
35. G. Long, C. Jiang, R. Sabatini, Z. Yang, M. Wei, L. N. Quan, Q. Liang, A. Rasmita, M. Askerka, G. Walters, X. Gong, J. Xing, X. Wen, R. Quintero-Bermudez, H. Yuan, G. Xing, X. R. Wang, D. Song, O. Voznyy, M. Zhang, S. Hoogland, W. Gao, Q. Xiong, and E. H. Sargent, *Spin control in reduced-dimensional chiral perovskites*, Nat. Photon. **12**, 528 (2018).
36. R. Nakajima, D. Hirobe, G. Kawaguchi, Y. Nabei, T. Sato, T. Narushima, H. Okamoto, and H. M. Yamamoto, *Giant spin polarization and a pair of antiparallel spins in a chiral superconductor*, Nature **613**, 479 (2023).
37. T. Yu, Z. Luo, and G. E. W. Bauer, *Chirality as generalized spin–orbit interaction in spintronics*, Phys. Rep. **1009**, 1 (2023).
38. R. Naaman, Y. Paltiel, and D. H. Waldeck, *Chiral molecules and the electron spin*, Nat. Rev. Chem. **3**, 250 (2019).
39. R. Naaman, Y. Paltiel, and D. H. Waldeck, *Chiral Induced Spin Selectivity Gives a New Twist on Spin-Control in Chemistry*, Acc. Chem. Res. **53**, 2659 (2020).
40. R. Naaman, Y. Paltiel, and D. H. Waldeck, *Chiral Molecules and the Spin Selectivity Effect*, J. Phys. Chem. **11**, 3660 (2020).
41. Y.-H. Kim, Y. Zhai, H. Lu, X. Pan, C. Xiao, E. A. Gaulding, S. P. Harvey, J. J. Berry, Z. V. Vardeny, J. M. Luther, and M. C. Beard, *Chiral-induced spin selectivity enables a room-temperature spin light-emitting diode*, Science **371**, 1129 (2021).
42. B. P. Bloom, Y. Paltiel, R. Naaman, and D. H. Waldeck, *Chiral Induced Spin Selectivity*, Chem. Rev. **124**, 1950 (2024).
43. K. Michaeli, N. Kantor-Uriel, R. Naaman, and D. H. Waldeck, *The electron's spin and molecular chirality – how are they related and how do they affect life processes?*, Chem. Soc. Rev. **45**, 6478 (2016).
44. O. Ávalos-Ovando, E. Y. Santiago, A. Movsesyan, X.-T. Kong, P. Yu, L. V. Besteiro, L. K. Khorashad, H. Okamoto, J. M. Slocik, M. A. Correa-Duarte, M. Comesaña-Hermo, T. Liedl, Z. Wang, G. Markovich, S. Burger, and A. O. Govorov, *Chiral Bioinspired Plasmonics: A Paradigm Shift for Optical Activity and Photochemistry*, ACS Photonics **9**, 2219 (2022).

45. W. Ma, L. Xu, A. F. de Moura, X. Wu, H. Kuang, C. Xu, and N. A. Kotov, *Chiral Inorganic Nanostructures*, Chem. Rev. **117**, 8041 (2017).
46. U. Hananel, A. Ben-Moshe, D. Tal, and G. Markovich, *Enantiomeric Control of Intrinsically Chiral Nanocrystals*, Adv. Mater. **32**, 1905594 (2020).
47. A. Ben-Moshe, A. da Silva, A. Müller, A. Abu-Odeh, P. Harrison, J. Waelder, F. Niroui, C. Ophus, A. M. Minor, M. Asta, W. Theis, P. Ercius, and A. P. Alivisatos, *The chain of chirality transfer in tellurium nanocrystals*, Science **372**, 729 (2021).
48. W. Jiang, Z.-b. Qu, P. Kumar, D. Vecchio, Y. Wang, Y. Ma, J. H. Bahng, K. Bernardino, W. R. Gomes, F. M. Colombari, A. Lozada-Blanco, M. Veksler, E. Marino, A. Simon, C. Murray, S. R. Muniz, A. F. de Moura, and N. A. Kotov, *Emergence of complexity in hierarchically organized chiral particles*, Science **368**, 642 (2020).
49. G. González-Rubio, J. Mosquera, V. Kumar, A. Pedrazo-Tardajos, P. Llombart, D. M. Solís, I. Lobato, E. G. Noya, A. Guerrero-Martínez, J. M. Taboada, F. Obelleiro, L. G. MacDowell, S. Bals, and L. M. Liz-Marzán, *Micelle-directed chiral seeded growth on anisotropic gold nanocrystals*, Science **368**, 1472 (2020).
50. R. M. Hazen and D. S. Sholl, *Chiral selection on inorganic crystalline surfaces*, Nat. Mater. **2**, 367 (2003).
51. T. Greber, Ž. Šljivančanin, R. Schillinger, J. Wider, and B. Hammer, *Chiral Recognition of Organic Molecules by Atomic Kinks on Surfaces*, Physical Review Letters **96**, 056103 (2006).
52. R. Fasel, M. Parschau, and K.-H. Ernst, *Amplification of chirality in two-dimensional enantiomorphous lattices*, Nature **439**, 449 (2006).
53. A. J. Gellman, *An Account of Chiral Metal Surfaces and Their Enantiospecific Chemistry*, Acc. Mater. Res. **2**, 1024 (2021).
54. A. Ahmadi, G. Attard, J. Feliu, and A. Rodes, *Surface Reactivity at "Chiral" Platinum Surfaces*, Langmuir **15**, 2420 (1999).
55. J. Zhang, Y. Tang, K. Lee, and M. Ouyang, *Nonepitaxial Growth of Hybrid Core-Shell Nanostructures with Large Lattice Mismatches*, Science **327**, 1634 (2010).
56. Y. Xia, X. Xia, and H.-C. Peng, *Shape-Controlled Synthesis of Colloidal Metal Nanocrystals: Thermodynamic versus Kinetic Products*, J. Am. Chem. Soc. **137**, 7947 (2015).
57. A. R. Tao, S. Habas, and P. Yang, *Shape Control of Colloidal Metal Nanocrystals*, Small **4**, 310 (2008).
58. M. L. Personick and C. A. Mirkin, *Making Sense of the Mayhem behind Shape Control in the Synthesis of Gold Nanoparticles*, J. Am. Chem. Soc. **135**, 18238 (2013).
59. S. W. Im, H.-Y. Ahn, R. M. Kim, N. H. Cho, H. Kim, Y.-C. Lim, H.-E. Lee, and K. T. Nam, *Chiral Surface and Geometry of Metal Nanocrystals*, Adv.

Mater. **32**, 1905758 (2020).
60. K. A. Willets and R. P. V. Duyne, *Localized Surface Plasmon Resonance Spectroscopy and Sensing*, Annu. Rev. Phys. Chem. **58**, 267 (2007).
61. J. Zhang, Y. Tang, K. Lee, and M. Ouyang, *Tailoring light–matter–spin interactions in colloidal hetero-nanostructures*, Nature **466**, 91 (2010).
62. L. Weng, H. Zhang, A. O. Govorov, and M. Ouyang, *Hierarchical synthesis of non-centrosymmetric hybrid nanostructures and enabled plasmon-driven photocatalysis*, Nat. Commun. **5**, 4792 (2014).
63. J.-E. Park, Y. Lee, and J.-M. Nam, *Precisely Shaped, Uniformly Formed Gold Nanocubes with Ultrahigh Reproducibility in Single-Particle Scattering and Surface-Enhanced Raman Scattering*, Nano Letters **18**, 6475 (2018).
64. X. Wang and Z. Tang, *Circular Dichroism Studies on Plasmonic Nanostructures*, Small **13**, 1601115 (2017).
65. Y. Li, H. Lin, W. Zhou, L. Sun, D. Samanta, and C. A. Mirkin, *Corner-, edge-, and facet-controlled growth of nanocrystals*, Science Advances **7**, eabf1410 (2021).
66. H. Zhang, M. Jin, and Y. Xia, *Noble-Metal Nanocrystals with Concave Surfaces: Synthesis and Applications*, Angew. Chem. Int. Ed. **51**, 7656 (2012).
67. P.-p. Wang, S.-J. Yu, and M. Ouyang, *Assembled Suprastructures of Inorganic Chiral Nanocrystals and Hierarchical Chirality*, J. Am. Chem. Soc. **139**, 6070 (2017).
68. B. Nikoobakht and M. A. El-Sayed, *Preparation and Growth Mechanism of Gold Nanorods (NRs) Using Seed-Mediated Growth Method*, Chem. Mater. **15**, 1957 (2003).
69. Z. L. Wang, M. B. Mohamed, S. Link, and M. A. El-Sayed, *Crystallographic facets and shapes of gold nanorods of different aspect ratios*, Surf. Sci. **440**, L809 (1999).
70. J. H. Song, F. Kim, D. Kim, and P. Yang, *Crystal Overgrowth on Gold Nanorods: Tuning the Shape, Facet, Aspect Ratio, and Composition of the Nanorods*, Chem. Eur. J. **11**, 910 (2005).
71. B. Goris, S. Bals, W. Van den Broek, E. Carbó-Argibay, S. Gómez-Graña, L. M. Liz-Marzán, and G. Van Tendeloo, *Atomic-scale determination of surface facets in gold nanorods*, Nat. Mater. **11**, 930 (2012).
72. C. R. Laramy, H. Lopez-Rios, M. N. O'Brien, M. Girard, R. J. Stawicki, B. Lee, M. O. de la Cruz, and C. A. Mirkin, *Controlled Symmetry Breaking in Colloidal Crystal Engineering with DNA*, ACS Nano **13**, 1412 (2019).
73. E. K. Payne, K. L. Shuford, S. Park, G. C. Schatz, and C. A. Mirkin, *Multipole Plasmon Resonances in Gold Nanorods*, . J. Phys. Chem. B **110**, 2150 (2006).
74. G. Zheng, Z. Bao, J. Pérez-Juste, R. Du, W. Liu, J. Dai, W. Zhang, L. Y. S. Lee, and K.-Y. Wong, *Tuning the Morphology and Chiroptical Properties*

of Discrete Gold Nanorods with Amino Acids, Angew. Chem. Int. Ed. **57**, 16452 (2018).

75. S. Hou, J. Yan, Z. Hu, and X. Wu, *Enhancing the plasmonic circular dichroism by entrapping chiral molecules at the core–shell interface of rod-shaped Au@Ag nanocrystals*, ChemComm **52**, 2059 (2016).
76. X. López-Lozano, H. Barron, C. Mottet, and H.-C. Weissker, *Aspect-ratio- and size-dependent emergence of the surface-plasmon resonance in gold nanorods – an ab initio TDDFT study*, Phys. Chem. Chem. Phys. **16**, 1820 (2014).
77. J. Zhu, F. Wu, Z. Han, Y. Shang, F. Liu, H. Yu, L. Yu, N. Li, and B. Ding, *Strong Light–Matter Interactions in Chiral Plasmonic–Excitonic Systems Assembled on DNA Origami*, Nano Letters **21**, 3573 (2021).
78. L. K. Khorashad, L. V. Besteiro, M. A. Correa-Duarte, S. Burger, Z. M. Wang, and A. O. Govorov, *Hot Electrons Generated in Chiral Plasmonic Nanocrystals as a Mechanism for Surface Photochemistry and Chiral Growth*, J. Am. Chem. Soc. **142**, 4193 (2020).
79. S.-H. Yang, R. Naaman, Y. Paltiel, and S. S. P. Parkin, *Chiral spintronics*, Nature Reviews Physics **3**, 328 (2021).
80. N. H. Cho, A. Guerrero-Martínez, J. Ma, S. Bals, N. A. Kotov, L. M. Liz-Marzán, and K. T. Nam, *Bioinspired chiral inorganic nanomaterials*, Nat. Rev. Bioeng. **1**, 88 (2023).
81. J. T. Collins, C. Kuppe, D. C. Hooper, C. Sibilia, M. Centini, and V. K. Valev, *Chirality and Chiroptical Effects in Metal Nanostructures: Fundamentals and Current Trends*, Adv. Opt. Mater. **5**, 1700182 (2017).
82. T.-T. Zhuang, Y. Li, X. Gao, M. Wei, F. P. García de Arquer, P. Todorović, J. Tian, G. Li, C. Zhang, X. Li, L. Dong, Y. Song, Y. Lu, X. Yang, L. Zhang, F. Fan, S. O. Kelley, S.-H. Yu, Z. Tang, and E. H. Sargent, *Regioselective magnetization in semiconducting nanorods*, Nat. Nanotechnol. **15**, 192 (2020).
83. U. Hananel, A. B. Moshe, G. Markovich, and A. P. Alivisatos, *Nanocrystals as Model Systems for Studying the Interplay Between Crystallization and Chirality*, Isr. J. Chem. **61**, 697 (2021).
84. H. Lu, Z. V. Vardeny, and M. C. Beard, *Control of light, spin and charge with chiral metal halide semiconductors*, Nat. Rev. Chem. **6**, 470 (2022).
85. A. Ben-Moshe, B. M. Maoz, A. O. Govorov, and G. Markovich, *Chirality and chiroptical effects in inorganic nanocrystal systems with plasmon and exciton resonances.*, Chem. Soc. Rev. **42**, 7028 (2013).
86. D. Vestler, I. Shishkin, E. A. Gurvitz, M. E. Nasir, A. Ben-Moshe, A. P. Slobozhanyuk, A. V. Krasavin, T. Levi-Belenkova, A. S. Shalin, P. Ginzburg, G. Markovich, and A. V. Zayats, *Circular dichroism enhancement in plasmonic nanorod metamaterials*, Opt. Express **26**, 17841 (2018).
87. M. L. Nesterov, X. Yin, M. Schäferling, H. Giessen, and T. Weiss, *The Role*

of Plasmon-Generated Near Fields for Enhanced Circular Dichroism Spectroscopy, ACS Photonics **3**, 578 (2016).

88. H. Zhang and A. O. Govorov, *Giant circular dichroism of a molecule in a region of strong plasmon resonances between two neighboring gold nanocrystals*, Phys. Rev. B **87**, 075410 (2013).
89. C. D. Aiello, J. M. Abendroth, M. Abbas, A. Afanasev, S. Agarwal, A. S. Banerjee, D. N. Beratan, J. N. Belling, B. Berche, A. Botana, J. R. Caram, G. L. Celardo, G. Cuniberti, A. Garcia-Etxarri, A. Dianat, I. Diez-Perez, Y. Guo, R. Gutierrez, C. Herrmann, J. Hihath, S. Kale, P. Kurian, Y.-C. Lai, T. Liu, A. Lopez, E. Medina, V. Mujica, R. Naaman, M. Noormandipour, J. L. Palma, Y. Paltiel, W. Petuskey, J. C. Ribeiro-Silva, J. J. Saenz, E. J. G. Santos, M. Solyanik-Gorgone, V. J. Sorger, D. M. Stemer, J. M. Ugalde, A. Valdes-Curiel, S. Varela, D. H. Waldeck, M. R. Wasielewski, P. S. Weiss, H. Zacharias, and Q. H. Wang, *A Chirality-Based Quantum Leap*, ACS Nano **16**, 4989 (2022).
90. C. Ye, Y. Sun, Y. Li, and X. Zhang, *Single-Shot Nondestructive Quantum Sensing for Gaseous Samples with Hundreds of Chiral Molecules*, J. Phys. Chem. Lett. **14**, 6772 (2023).
91. S. Mondal, F. Dumur, D. Gigmes, M. P. Sibi, M. P. Bertrand, and M. Nechab, *Enantioselective Radical Reactions Using Chiral Catalysts*, Chem. Rev. **122**, 5842 (2022).
92. Q. Qian, H. Ren, J. Zhou, Z. Wan, J. Zhou, X. Yan, J. Cai, P. Wang, B. Li, and Z. Sofer, *Chiral molecular intercalation superlattices*, Nature **606**, 902 (2022).
93. X. Yin, M. Schäferling, B. Metzger, and H. Giessen, *Interpreting Chiral Nanophotonic Spectra: The Plasmonic Born–Kuhn Model*, Nano Lett. **13**, 6238 (2013).
94. B. Foerster, J. Rutten, H. Pham, S. Link, and C. Sönnichsen, *Particle Plasmons as Dipole Antennas: State Representation of Relative Observables*, J. Phys. Chem. C **122**, 19116 (2018).
95. T. J. Davis and D. E. Gómez, *Colloquium: An algebraic model of localized surface plasmons and their interactions*, Rev. Mod. Phys. **89**, 011003 (2017).
96. M. S. Davis, W. Zhu, J. K. Lee, H. J. Lezec, and A. Agrawal, *Microscopic origin of the chiroptical response of optical media*, Sci. Adv. **5**, eaav8262 (2019).
97. J. A. Schellman, *Symmetry rules for optical rotation*, Acc. Chem. Res. **1**, 144 (1968).
98. L. V. Besteiro, H. Zhang, J. Plain, G. Markovich, Z. Wang, and A. O. Govorov, *Aluminum Nanoparticles with Hot Spots for Plasmon-Induced Circular Dichroism of Chiral Molecules in the UV Spectral Interval*, Adv. Opt. Mater. **5**, 1700069 (2017).
99. R. Chikkaraddy, B. de Nijs, F. Benz, S. J. Barrow, O. A. Scherman, E. Rosta,

A. Demetriadou, P. Fox, O. Hess, and J. J. Baumberg, *Single-molecule strong coupling at room temperature in plasmonic nanocavities*, Nature **535**, 127 (2016).
100. K. Słowik, R. Filter, J. Straubel, F. Lederer, and C. Rockstuhl, *Strong coupling of optical nanoantennas and atomic systems*, Phys. Rev. B **88**, 195414 (2013).
101. B. Gallinet and O. J. F. Martin, *Ab initio theory of Fano resonances in plasmonic nanostructures and metamaterials*, Phys. Rev. B **83**, 235427 (2011).
102. V. Giannini, Y. Francescato, H. Amrania, C. C. Phillips, and S. A. Maier, *Fano Resonances in Nanoscale Plasmonic Systems: A Parameter-Free Modeling Approach*, Nano Lett. **11**, 2835 (2011).
103. M. F. Limonov, M. V. Rybin, A. N. Poddubny, and Y. S. Kivshar, *Fano resonances in photonics*, Nat. Photon. **11**, 543 (2017).
104. F. Wu, N. Li, B. Ding, and W. Zhang, *Plasmon–Exciton Strong Coupling Effects of the Chiral Hybrid Nanostructures Based on the Plexcitonic Born–Kuhn Model*, ACS Photonics **10**, 1356 (2023).
105. H. U. Yang, J. D'Archangel, M. L. Sundheimer, E. Tucker, G. D. Boreman, and M. B. Raschke, *Optical dielectric function of silver*, Phys. Rev. B **91**, 235137 (2015).
106. 10. D. Rioux, S. Vallières, S. Besner, P. Muñoz, E. Mazur, and M. Meunier, *An Analytic Model for the Dielectric Function of Au, Ag, and their Alloys*, Adv. Opt. Mater. **2**, 176 (2014).
107. A. Ben-Moshe, A. O. Govorov, and G. Markovich, *Enantioselective synthesis of intrinsically chiral mercury sulfide nanocrystals*, Angew. Chem. Int. Ed. **52**, 1275 (2013).
108. Y. Dong, Y. Zhang, X. Li, Y. Feng, H. Zhang, and J. Xu, *Chiral Perovskites: Promising Materials toward Next-Generation Optoelectronics*, Small **15**, 1902237 (2019).
109. G. Long, R. Sabatini, M. I. Saidaminov, G. Lakhwani, A. Rasmita, X. Liu, E. H. Sargent, and W. Gao, *Chiral-perovskite optoelectronics*, Nat. Rev. Mater. **5**, 423 (2020).
110. L. Gui, M. Hentschel, J. Defrance, J. Krauth, T. Weiss, and H. Giessen, *Nonlinear Born-Kuhn Analog for Chiral Plasmonics*, ACS Photonics **6**, 3306 (2019).
111. K. Morisawa, T. Ishida, and T. Tatsuma, *Photoinduced Chirality Switching of Metal-Inorganic Plasmonic Nanostructures*, ACS Nano **14**, 3603 (2020).
112. W. Ma, L. Xu, L. Wang, C. Xu, and H. Kuang, *Chirality-Based Biosensors*, Adv. Funct. Mater. **29**, 1805512 (2019).
113. B. P. Isaacoff and K. A. Brown, *Progress in Top-Down Control of Bottom-Up Assembly*, Nano Lett. **17**, 6508 (2017).
114. M. Schäferling, *Chiral Nanophotonics*. (Springer, Switzerland, 2017)
115. J. Crassous, M. J. Fuchter, D. E. Freedman, N. A. Kotov, J. Moon, M. C.

Beard, and S. Feldmann, *Materials for chiral light control*, Nature Reviews Materials **8**, 365 (2023).
116. D. Ayuso, O. Neufeld, A. F. Ordonez, P. Decleva, G. Lerner, O. Cohen, M. Ivanov, and O. Smirnova, *Synthetic chiral light for efficient control of chiral light–matter interaction*, Nat. Photon. **13**, 866 (2019).
117. J. Karst, N. H. Cho, H. Kim, H.-E. Lee, K. T. Nam, H. Giessen, and M. Hentschel, *Chiral Scatterometry on Chemically Synthesized Single Plasmonic Nanoparticles*, ACS Nano **13**, 8659 (2019).
118. S. Kempter, A. Khmelinskaia, M. T. Strauss, P. Schwille, R. Jungmann, T. Liedl, and W. Bae, *Single Particle Tracking and Super-Resolution Imaging of Membrane-Assisted Stop-and-Go Diffusion and Lattice Assembly of DNA Origami*, ACS Nano **13**, 996 (2019).
119. A. Rafiei Miandashti, L. Khosravi Khorashad, M. E. Kordesch, A. O. Govorov, and H. H. Richardson, *Experimental and Theoretical Observation of Photothermal Chirality in Gold Nanoparticle Helicoids*, ACS Nano **14**, 4188 (2020).
120. X.-T. Kong, L. Khosravi Khorashad, Z. Wang, and A. O. Govorov, *Photothermal Circular Dichroism Induced by Plasmon Resonances in Chiral Metamaterial Absorbers and Bolometers*, Nano Lett. **18**, 2001 (2018).
121. F. J. Giessibl, *Advances in atomic force microscopy*, Rev. Mod. Phys. **75**, 949 (2003).
122. A. A. Sifat, J. Jahng, and E. O. Potma, *Photo-induced force microscopy (PiFM) – principles and implementations*, Chem. Soc. Rev. **51**, 4208 (2022).
123. A. Dazzi, F. Glotin, and R. Carminati, *Theory of infrared nanospectroscopy by photothermal induced resonance*, J. Appl. Phys. **107**, 124519 (2010).
124. . Mathurin, A. Deniset-Besseau, D. Bazin, E. Dartois, M. Wagner, and A. Dazzi, *Photothermal AFM-IR spectroscopy and imaging: Status, challenges, and trends*, J. Appl. Phys. **131**, 010901 (2022).
125. B. Hecht, B. Sick, U. P. Wild, V. Deckert, R. Zenobi, O. J. F. Martin, and D. W. Pohl, *Scanning near-field optical microscopy with aperture probes: Fundamentals and applications*, J. Chem. Phys. **112**, 7761 (2000).
126. X. Chen, D. Hu, R. Mescall, G. You, D. N. Basov, Q. Dai, and M. Liu, *Modern Scattering-Type Scanning Near-Field Optical Microscopy for Advanced Material Research*, Adv. Mater. **31**, 1804774 (2019).
127. A. García-Etxarri, I. Romero, F. J. García de Abajo, R. Hillenbrand, and J. Aizpurua, *Influence of the tip in near-field imaging of nanoparticle plasmonic modes: Weak and strong coupling regimes*, Phys. Rev. B **79**, 125439 (2009).
128. R. Büchner, T. Weber, L. Kühner, S. A. Maier, and A. Tittl, *Tip Coupling and Array Effects of Gold Nanoantennas in Near-Field Microscopy*, ACS Photonics **8**, 3486 (2021).
129. M. Esmann, S. F. Becker, J. Witt, J. Zhan, A. Chimeh, A. Korte, J. Zhong,

R. Vogelgesang, G. Wittstock, and C. Lienau, *Vectorial near-field coupling*, Nat. Nanotechnol **14**, 698 (2019).
130. X. Chen, Y. Chen, M. Yan, and M. Qiu, *Nanosecond Photothermal Effects in Plasmonic Nanostructures*, ACS Nano **6**, 2550 (2012).
131. J. Jahng, J. Brocious, D. A. Fishman, F. Huang, X. Li, V. A. Tamma, H. K. Wickramasinghe, and E. O. Potma, *Gradient and scattering forces in photoinduced force microscopy*, Phys. Rev. B **90**, 155417 (2014).
132. K. Ray, S. P. Ananthavel, D. H. Waldeck, and R. Naaman, *Asymmetric Scattering of Polarized Electrons by Organized Organic Films of Chiral Molecules*, Science **283**, 814 (1999).
133. T. P. Yoon and E. N. Jacobsen, *Privileged Chiral Catalysts*, Science **299**, 1691 (2003).
134. B. Gohler, V. Hamelbeck, T. Z. Markus, M. Kettner, G. F. Hanne, Z. Vager, R. Naaman, and H. Zacharias, *Spin Selectivity in Electron Transmission Through Self-Assembled Monolayers of Double-Stranded DNA*, Science **331**, 894 (2011).
135. A.-M. Guo and Q.-F. Sun, *Spin-Selective Transport of Electrons in DNA Double Helix*, Phys.Rev.Lett. **108**, 218102 (2012).
136. R. Naaman and D. H. Waldeck, *Chiral-induced Spin Selectivity Effect*, J.Phys.Chem.Lett. **3**, 2178 (2012).
137. P. Cintas, *Biochirality*. (Springer, New York, 2013).
138. D. Zager and Z. Vager, *Spin order without magnetism – a new phase of spontaneously broken symmetry in condensed matter*, Phys. Lett. A **376**, 1895 (2013).
139. R. Naaman and D. H. Waldeck, *Spintronics and Chirality: Spin Selectivity in Electron Transport Through Chiral Molecules*, Ann. Rev. Phys. Chem **66**, 263 (2015).
140. P. Chandra Mondal, C. Fontanesi, D. H. Waldeck, and R. Naaman, *Field and Chirality Effects on Electrochemical Charge Transfer Rates: Spin Dependent Electrochemistry*, ACS Nano **9**, 3377 (2015).
141. R. A. Rosenberg, D. Mishra, and R. Naaman, *Chiral Selective Chemistry Induced by Natural Selection of Spin- Polarized Electrons*, Angew. Chem. Int. Ed. **54**, 7295 (2015).
142. C.-H. Ko, Q. Zhu, F. Tassinari, G. Bullard, P. Zhang, D. N. Beratan, R. Naaman, and M. J. Therien, *Twisted molecular wires polarize spin currents at room temperature*, Proc. Nat. Aca. Sci. **119**, e2116180119 (2022).
143. F. Evers, A. Aharony, N. Bar-Gill, O. Entin-Wohlman, P. Hedegård, O. Hod, P. Jelinek, G. Kamieniarz, M. Lemeshko, K. Michaeli, V. Mujica, R. Naaman, Y. Paltiel, S. Refaely-Abramson, O. Tal, J. Thijssen, M. Thoss, J. M. van Ruitenbeek, L. Venkataraman, D. H. Waldeck, B. Yan, and L. Kronik, *Theory of Chirality Induced Spin Selectivity: Progress and Challenges*, Adv. Mater. **34**, 2106629 (2022).
144. A. Ghazaryan, Y. Paltiel, and M. Lemeshko, *Analytic Model of Chiral-*

Induced Spin Selectivity, J. Phys. Chem. C **124**, 11716 (2020).
145. S. Ghosh and e. al, *Effect of Chiral Molecules on the Electron's Spin Wavefunction at Interfaces*, J. Phys. Chem. Lett. **11**, 1550 (2020).
146. J. Fransson, *Vibrational origin of exchange splitting and chiral-induced spin selectivity,* Phys.Rev. B **102**, 235416 (2020).
147. J. Fransson, *Chirality-Induced Spin Selectivity: The Role of Electron Correlations*, J. Phys. Chem. Lett. **10**, 7126 (2019).
148. J. Fransson, *Charge Redistribution and Spin Polarization Driven by Correlation Induced Electron Exchange in Chiral Molecules*, Nano Lett. **21**, 3026−3032 (2021).
149. S. Dalum and P. Hedegard, *Theory of Chiral Induced Spin Selectivity*, Nano Lett. **19**, 5253 (2019).
150. S. Alwan and Y. Dubi, *Spinterface Origin for the Chirality-Induced Spin-Selectivity Effect*, J. Am. Chem. Soc. **143**, 14235 (2021).
151. T. P. Fay and D. T. Limmer, *Origin of Chirality Induced Spin Selectivity in Photoinduced Electron Transfer*, Nano Lett. **21**, 6696−6702 (2021).
152. L. Zhang, Y. Hao, W. Qin, S. Xie, and F. Qu, *Chiral-induced spin selectivity: A polaron transport model*, Phys. Rev. B **102**, 214303 (2020).
153. D. D. Awschalom, D. Loss, and N. Samarth, *Semiconductor Spintronics and Quantum Computation*. (Springer,2002).
154. N. T. Phuc, *Floquet-engineered chiral-induced spin selectivity*, J. Chem. Phys. **159**, 054706 (2023).
155. T. Oka and S. Kitamura, *Floquet Engineering of Quantum Materials*, Annu. Rev. Condens. Matter Phys. **10**, 387 (2019).
156. M. Rasmusson, A. N. Tarnovsky, E. Åkesson, and V. Sundström, *On the use of two-photon absorption for determination of femtosecond pump–probe cross-correlation functions*, Chem. Phys. Lett.**335**, 201 (2001).
157. V. I. Klimov and D. W. MaBranch, *Auger-process-induced charge separation in semiconductor nanocrystals*, Phys. Rev. B **55**, 13173 (1997).
158. V. Klimov, S. Hunsche, and H. Kurz, *Biexciton effects in femtosecond nonlinear transmission of semiconductor quantum dots*, Phys. Rev. B **50**, 8110(R) (1994).
159. J. Zhang, Y. Tang, K. Lee, and M. Ouyang, *Tailoring light–matter–spin interactions in colloidal hetero-nanostructures*, Nature **466**, 91 (2010).
160. Y. Tang, A. F. Goncharov, V. V. Struzhkin, R. J. Hemley, and M. Ouyang, *Spin of Semiconductor Quantum Dots under Hydrostatic Pressure*, Nano Letters **10**, 358 (2010).
161. M. Wolf and J. Berezovsky, *Homogeneous and inhomogeneous sources of optical transition broadening in room temperature CdSe/ZnS nanocrystal quantum dots*, Appl. Phys. Lett. **105**, 143105 (2014).
162. J. Berezovsky, O. Gywat, F. Meier, D. Battaglia, X. Peng, and D. D. Awschalom, *Initialization and read-out of spins in coupled core–shell quantum dots*, Nat. Phys. **2**, 831 (2006).

163. M. Ouyang and D. D. Awschalom, *Coherent spin transfer between molecularly bridged quantum dots*, Science **301**, 1074 (2003).
164. J. A. Gupta, D. D. Awschalom, X. Peng, and A. P. Alivisatos, *Spin coherence in semiconductor quantum dots*, Phys. Rev. B **59**, 10421 (1999).
165. J. A. Gupta, D. D. Awschalom, A. L. Efros, and A. V. Rodina, *Spin dynamics in semiconductor nanocrystals*, Phys. Rev. B **66**, 125307 (2002).
166. F. Meier and D. D. Awschalom, *Faraday rotation spectroscopy of quantum-dot quantum wells*, Phys. Rev. B **71** (2005).
167. F. Meier, V. Cerletti, O. Gywat, D. Loss, and D. D. Awschalom, *Molecular spintronics: coherent spin transfer in coupled quanrtum dots*, Phys. Rev. B **69**, 195315 (2004).
168. J. Berezovsky, M. Ouyang, F. Meier, Awschalom, B. D.D., and X. Peng, *Spin dynamics and level structure of quantum-dot quantum wells*, Phys. Rev. B **71**, 081309 (2005).
169. H. Tong, D. Feng, X. Li, L. Deng, Y. Leng, T. Jia, and Z. Sun, *Room-Temperature Electron Spin Generation by Femtosecond Laser Pulses in Colloidal CdS Quantum Dots*, Materials **6**, 4523 (2013).
170. O. Ben Dor, S. Yochelis, A. Radko, K. Vankayala, E. Capua, A. Capua, S.-H. Yang, L. T. Baczewski, S. S. P. Parkin, R. Naaman, and Y. Paltiel, *Magnetization switching in ferromagnets by adsorbed chiral molecules without current or external magnetic field*, Nat. Commun. **8**, 14567 (2017).
171. M. Ozeri, J. Xu, G. Bauer, L. A. B. Olde Olthof, G. Kimbell, A. Wittmann, S. Yochelis, J. Fransson, J. W. A. Robinson, Y. Paltiel, and O. Millo, *Modification of Weak Localization in Metallic Thin Films Due to the Adsorption of Chiral Molecules*, J. Phys. Chem. Lett. **14**, 4941 (2023).
172. R. Naaman, D. H. Waldeck, and Y. Paltiel, *Chiral molecules-ferromagnetic interfaces, an approach towards spin controlled interactions*, Appl. Phys. Lett. **115**, 133701 (2019).
173. K. Kondou, M. Shiga, S. Sakamoto, H. Inuzuka, A. Nihonyanagi, F. Araoka, M. Kobayashi, S. Miwa, D. Miyajima, and Y. Otani, *Chirality-Induced Magnetoresistance Due to Thermally Driven Spin Polarization*, J. Am. Chem. Soc **144**, 7302 (2022).
174. J. Kwon, W. J. Choi, U. Jeong, W. Jung, I. Hwang, K. H. Park, S. G. Ko, S. M. Park, N. A. Kotov, and J. Yeom, *Recent advances in chiral nanomaterials with unique electric and magnetic properties*, Nano Convergence **9**, 32 (2022).
175. A. Soumyanarayanan, N. Reyren, A. Fert, and C. Panagopoulos, *Emergent phenomena induced by spin–orbit coupling at surfaces and interfaces*, Nature **539**, 509 (2016).
176. S. Tsuda and C. H. Brito Cruz, *Femtosecond Dynamics of the Optical Stark Effect in Semiconductor-Doped Glass*, Appl. Phys. Lett. **68**, 1093 (1995).
177. J. A. Gupta, R. Knobel, N. Samarth, and D. D. Awschalom, *Ultrafast Manipulation of Electron Spin Coherence*, Science **292**, 2458 (2001).